Dynamics of Structures

2nd workshop on dynamic loads and response of structures and soil dynamics

Hansen, Lars Pilegaard

Publication date:
1996

Document Version
Publisher's PDF, also known as Version of record

DYNAMICS OF STRUCTURES

2nd Workshop on Dynamic Loads and Response of Structures and Soil Dynamics

AALBORG UNIVERSITY
DENMARK
November 13 - 14, 1996

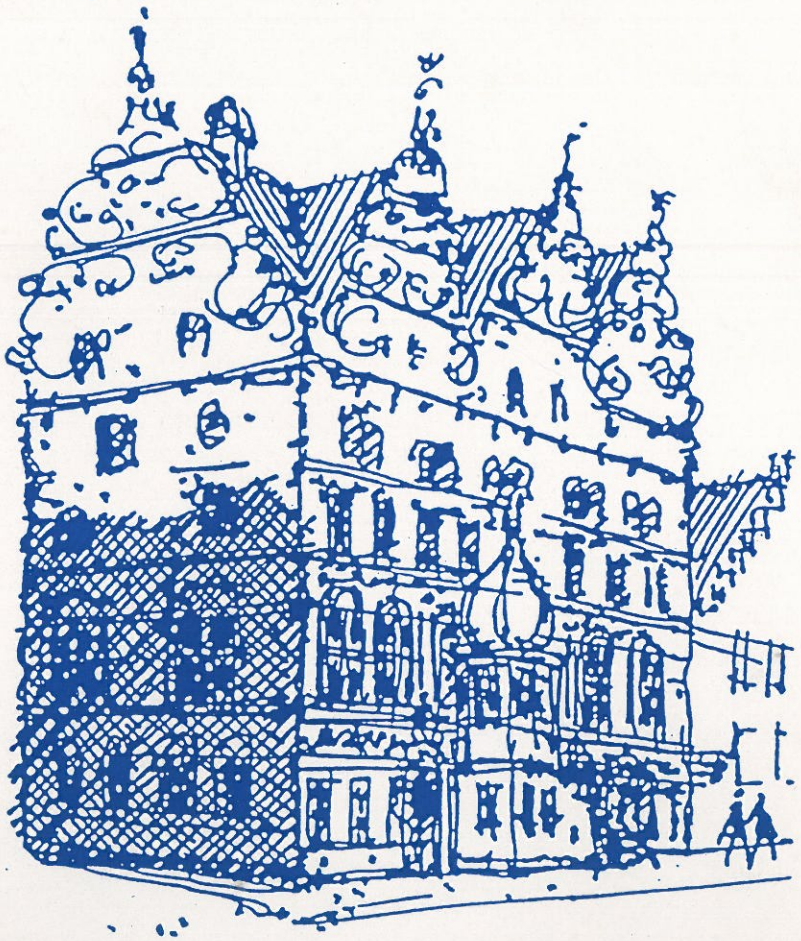

Foreword

"Dynamics of Structures" is a research programme started in 1993 and sponsored by the Danish Technical Research Council. It is a cooperative effort of the Department of Building Technology and Structural Engineering and the Department of Civil Engineering at Aalborg University and the Department of Structural Engineering and Materials at the Technical University of Denmark (until the end of 1995).

The purpose of the programme is to conduct research and to provide research education and results relating to dynamic loads and response of structures and foundations. Characterization and modelling of materials under time varying loads are also parts of the research programme. The research will develop and use both analytical, numerical and experimental methods.

The subject areas dealt with in the research programme are:

- Analysis of structures
- Wind and wave loads
- Soil mechanics
- System identification
- Damage detection
- Fatigue and crack propagation
- Man induced vibrations
- Experimental methods

The purpose of this second workshop held at Aalborg University, November 13 - 14, 1996 was to present some of the results from the projects in the research programme as well as results from projects at other universities and consulting firms. Another purpose was to get researchers working with related areas in closer connection with each other.

36 researchers from Norway, Sweden and Denmark participated in the workshop.

Aalborg, Dec. 1996

Lars Pilegaard Hansen
Department of Building Technology and Structural Engineeering
Aalborg University
Sohngaardsholmsvej 57
DK 9000 Aalborg
tel. +45 9635 8585
fax. +45 9814 2366
email i6lph@civil.auc.dk

PROGRAMME

Wednesday, November 13

17.00	Welcome. Hall, Building A, Sohngårdsholmsvej 57, 9000 Aalborg
17.15 - 19.00	Visit in the laboratories
20.00	Dinner at downtown restaurant "Kniv og Gaffel", Maren Turisgade 10, 9000 Aalborg

Thursday, November 14

Lecture hall F108, Sohngårdsholmsvej 57, 9000 Aalborg

09.00	Welcome / Lars Pilegaard Hansen	
Session 1	**Modelling of Dynamic Loads** Chairman: Søren R.K. Nielsen	
09.05 - 09.25	Steen Krenk:	Modelling of Wind Loads
09.25 - 09.45	Jeppe Jönsson:	Computational Investigation of Repetitive Vertical Human Loading
09.45 - 10.05	Kim Mørk:	Design Criteria for Submarine Pipelines Subjected to Vortex Induced Vibrations
10.05 - 10.25	B. L. Josefson et al:	Mechanical Energy Flow in Vibrating Structures
10.25 - 10.45	Allan Larsen:	Elements in Aerodynamic Flutter Control
10.45 - 11.15	Coffee	
Session 2	**Dynamic Properties of Materials** Chairman: Jørgen S. Steenfelt	
11.15 - 11.35	Lars Bo Ibsen:	Bearing Capacity of Foundations Subjected to Impact Loads
11.35 - 11.55	Mikael Enelund:	Formulation and Integration of Standard Linear Solid with Integer and Fractional Rule Laws
11.55 - 12.15	Thomas C. Hansen:	Fatigue and Crack Propagation in Structural Materials
12.15 - 12.35	B. Skallerud and Z.L.Zhang:	Numerical Analysis of Damage Evolution in Cyclic Elastic-Plastic Crack Growth Problems
12.35 - 12.55	Poul Lade:	Rotational Kinematic Hardening Model for Sand
13.00 - 14.00	Lunch	
Session 3	**Dynamic Analysis of Structures** Chairman: Lars Pilegaard Hansen	
14.00 - 14.20	Søren R. K. Nielsen/ Henriette Hansen:	Active Vibration Control
14.20 - 14.40	Helge Gravesen and Morten Faurskov:	Displacements of Øresund Bridge Piers from Ship Impact
14.40 - 15.00	Poul S. Skjærbæk:	Earthquake Tests of Reinforced Concrete Frames

Dynamics of Structures
2 nd Workshop - Aalborg - November 13 - 14, 1996

Participants

Andersen, Knut H.	NGI, Norway
Andersen, Palle	AAU, Denmark
Andrén, Peter	KTH, Sweden
Asmussen, John	AAU, Denmark
Brincker, Rune	AAU, Denmark
Bødker, Lars	AAU, Denmark
Enelund, Mikael	CTH, Sweden
Faurschou, Morten	Carl Bro a/s, Denmark
Gravesen, Helge	Carl Bro a/s, Denmark
Hansen, Henriette	AAU, Denmark
Hansen, Svend Ole	Svend Ole Hansen, Denmark
Hansen, Lars Pilegaard	AAU, Denmark
Hansen, Thomas Cornelius	H+H Industri, Denmark
Ibsen, Lars Bo	AAU, Denmark
Jacobsson, Lars	CTH, Sweden
Jakobsen, Kim Parsberg	AAU, Denmark
Jensen, Jakob Laigaard	COWI, Denmark
Josefson, Lennart	CTH, Sweden
Jönsson, Jeppe	ES-Consult A/S, Denmark
Kirkegaard, Poul Henning	AAU, Denmark
Krenk, Steen	Lund University, Sweden
Lade, Poul	The John Hopkins University, USA / AAU, Denmark
Larsen, Allan	COWI, Denmark
Mørk, Kim	Det Norske Veritas, Norway
Nielsen, Søren R.K.	AAU, Denmark
Oscarsson, Johan	CTH, Sweden
Petersson, Martin	CTH, Sweden
Rasmussen, Klaus	AAU, Denmark
Rytter, Anders	Rambøll, Denmark
Skallerud, Bjørn	The Norwegian Inst. of Techn, Norway /AAU,Denmark
Skjærbæk, Poul S.	AAU, Denmark
Steenfelt, Jørgen S.	AAU, Denmark
Sørensen, John Dalsgård	AAU, Denmark
Thesbjerg, Leo	Rambøll, Denmark
Thorbek, Lars	Svend Ole Hansen, Denmark
Wilson, Anders	CTH, Sweden

Secretariat: Pernille Sørensen, AAU, Denmark

Table of Contents

DYNAMIC ALONG-WIND RESPONSE OF SIMPLE STRUCTURES

S.O. Hansen[1] and S. Krenk[2]

Abstract

A design procedure for dynamic along-wind response of simple structures is presented. The time dependence of turbulent wind velocity field is described by a frequency spectrum and the spatial coherence by the normalized along-wind cross spectrum. A simple turbulence length-scale is proposed, and a modification of the traditional exponential coherence function is presented, leading to a reduction of the high frequency part of the joint acceptance function used to calculate resonant response. The low-frequency, non-resonant part of the response is estimated from a quasi-static analysis without use of the mode shape. Simple explicit design formulas are developed for the joint acceptance function for line-like structures with simple mode shapes, and a consistent generalisation to plate-like structures is developed. The presentation leads to a self contained design procedure illustrated by three examples.

Introduction

The dynamic along-wind response of structures to turbulent wind can be estimated theoretically by methods originally proposed by Davenport (1962). The basic requirements are that: the wind load is determined from the undisturbed turbulent wind field, the relevant mode of vibration is uncoupled from other modes, and the structure is modelled as elastic with viscous damping. The time dependence of the turbulent wind velocity field is described by a frequency spectrum, and the spatial correlation by a normalized co-spectrum and a correlation function. The low-frequency structural response is calculated as a double integral of the correlation function and the response influence function used for static load. The resonant structural response calculations contain the joint acceptance function in form of a multiple integral of the normalized co-spectrum and the mode shape over the surface of the structure. For line-like structures this is a double integral, and for plate-like structures a quadruple integral. In principle the integration should include both front and back face of the building, but the rather limited data for the back face show considerable scatter, and seems to justify the use of a the front face only, Simiu and Scanlan (1986).

[1] Svend Ole Hansen ApS, Sct. Jørgens Alle 5-7, DK-1615 Copenhagen, Denmark
[2] Division of Mechanics, Lund University, Box 118, S-221 00 Lund, Sweden

The evaluation of the joint acceptance function, containing the spatial integral, depends on the functional form of the co-spectrum. Traditionally a simple exponential form has been assumed, in which separation distance r, frequency n and mean wind velocity U are combined into a single variable nr/U. This format contains two inconsistencies: the co-spectrum must integrate to zero over a plane transverse to the mean wind, and the correlation should be less than unity at any finite separation distance. However, measurements of the co-spectrum contain considerable scatter, and the exponential format leads to substantial simplifications in the evaluation of the joint acceptance function for simple structures and mode shapes. A modification of the exponential format leading to a simple consistent form of the normalized co-spectrum was proposed by Krenk (1996) based on theoretical considerations. The main effects of the modified co-spectrum format are to introduce finite correlation between points at finite distance, and to decrease the value of the high frequency (or large separation) part of the co-spectrum by some 25 percent. In the following design procedure these effects are incorporated into explicit design formulas for the joint acceptance function of line-like structures. Furthermore the explicit format is extended in a consistent way to plate-like structures, combining results from similar line-like structures.

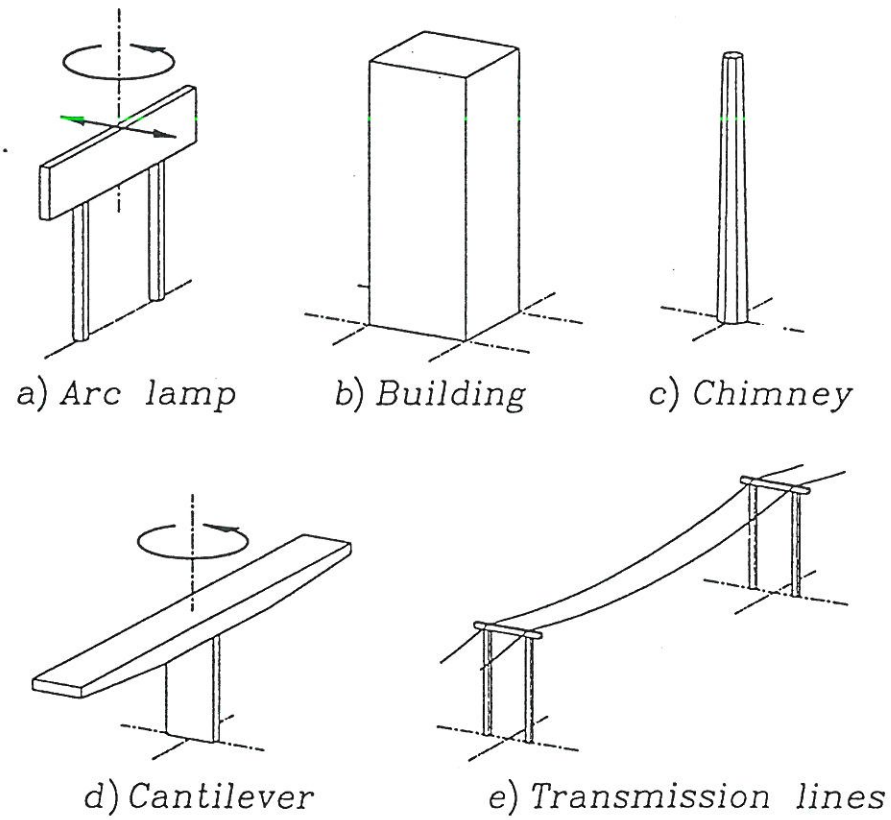

Figure 1. Typical line- and plate-like structures.

The present paper develops a self contained design procedure for dynamic along-wind response of line-like and plate-like structures. Typical examples are shown in Fig. 1. The procedure contains a simple description of the wind in terms of a frequency spectrum containing the integral length-scale L of the turbulence, a co-spectrum containing the horizontal and vertical decay constants C_y and C_z and an exponential correlation function depending on integral length-scales. Finite correlation between the turbulent wind velocity components at different points for all frequencies is obtained by use of a modified wave number containing the length scale of the wind. Explicit design formulas are given for several common line- and plate-like structures and mode shapes. The proposed design procedure is simpler and presumably more accurate, than the recent Eurocode (1994) proposal based on the traditional exponential co-spectrum function with a product format for resonant response of plate-like structures and less accurate approximations of the low-frequency response.

Wind Structure

The present procedure is based on the along-wind turbulence component of the undisturbed natural wind. The turbulent wind field is anisotropic and the mean wind increases with height. This complicates a full statistical description of the wind field, and although an anisotropic turbulence model incorporating wind shear has recently been developed, Mann (1994) and Mann and Krenk (1994), engineering design typically is based on a turbulence intensity distribution, a normalized frequency spectrum of the turbulent wind components at a point, a spatial description of the normalized joint spectrum of the velocity components at two separate points and a correlation function used for low-frequency response.

Turbulence intensity

The turbulence intensity $I_u(z)$ for the along-wind turbulent velocity component u at height z is defined as

$$I_u(z) = \frac{\sigma_u(z)}{U(z)} \tag{1}$$

where $\sigma_u(z)$ is the standard deviation of the turbulent velocity component u, and $U(z)$ is the mean wind speed, both at height z. For flat terrain σ_u is approximately independent of height, and the turbulence intensity can be represented as, Simiu and Scanlan (1986),

$$I_u(z) = \frac{1}{ln(z/z_0)} \tag{2}$$

where z_0 is the roughness length of the terrain.

Power spectral density

It is convenient to describe the one-sided power spectral density of the along-wind turbulent velocity component u at height z in terms of the non-dimensional power spectral density function $R_n(z,n)$, defined as

$$R_n(z,n) = \frac{nS_u(z,n)}{\sigma_u^2(z)} \tag{3}$$

where n is the frequency and $S_u(z,n)$ is the power spectral density of u. The non-dimensional format (3) is convenient for use with a logarithmic frequency scale, where integration with respect to the increment $d(\ln n) = dn / n$ is normalized to unity.

The high frequency part of the spectral density corresponds to rather small vortices, and the form of the spectrum can therefore be estimated from the theory of homogeneous turbulence using Taylor's hypothesis of convected turbulence, Batchelor (1953). Consideration of energy transport and dissipation leads to the asymptotic high frequency behaviour

$$R_n(z,n) \sim A\left(\frac{nL(z)}{U(z)}\right)^{-2/3} = A\, f_L^{-2/3}(z) \quad , \quad f_L >> 1 \tag{4}$$

where A is a non-dimensional parameter, and

$$f_L(z) = \frac{nL(z)}{U(z)} \tag{5}$$

is a non-dimensional frequency defined in terms of the mean wind speed $U(z)$ and a length-scale of the turbulence $L(z)$. Usually $L(z)$ is defined as the longitudinal integral length-scale, i.e. the length obtained by integrating the correlation function, $\rho_u(z,r_x)$, of longitudinal turbulence components with zero time lag at height z and with a longitudinal separation of distance r_x. In practice the integral length scale is calculated using the experimentally determined auto-correlation function, $\rho_u^T(z,\tau)$ for the along-wind turbulence component u at height z, i.e.

$$L(z) = U(z)\int_0^\infty \rho_u^T(z,\tau)d\tau = \frac{U(z)S_u(z,n=0)}{4\sigma_u^2(z)} \tag{6}$$

in which $\rho_u^T(z,\tau) = \rho_u(z,r_x = U(z)\tau)$ according to Taylor's hypothesis of convected turbulence. Thus, the integral length-scale is determined by the actual spectrum S_u at zero frequency. The low frequency behaviour of the non-dimensional power spectral density is

$$R_n(z,n) \sim 4\frac{nL(z)}{U(z)} = 4f_L(z), \qquad f_L << 1 \tag{7}$$

In addition to the low and high frequency asymptotics a good spectral representation should also represent the central part with the maximum value of $R_n(z,n)$ well.

The spectral density representations used in practice have a fixed format with the correct powers of f_L for low and high frequency. The format (3) of the non-dimensional power spectral density implies that any scaled frequency af_L leads to the same normalization, independent of the parameter a. Calibration of any fixed spectral density format therefore essentially consists in selecting the optimal value of the scaling parameter a. Experience indicates that a simple, yet fairly robust, calibration can be obtained from the high frequency relation (4) using measured values of the parameter A. According to ESDU (1985) full-scale measurements of the high frequency behaviour of the fluctuating wind field at different heights indicate that A is a slowly decreasing function of height, but for structures with heights up to 200-300m the ESDU data indicate that the use of $A \approx 0.14$, independent of height, leads to errors less than 5%, when L is the integral length-scale of the measured correlation function.

A simple spectral density function that satisfies the normalization condition and $A = 0.14$ is

$$R_n(z,n) = \frac{\frac{2}{3}10.2f_L(z)}{(1+10.2f_L(z))^{5/3}} = \frac{6.8f_L(z)}{(1+10.2f_L(z))^{5/3}} \tag{8}$$

This is a modification of a spectral density originally proposed by Kaimal et al. (1972) and also used by Simiu and Scanlan (1986). In the original form of the spectral density a term $50nz/U$ was used instead of $10.2f_L$, corresponding to an integral length-scale proportional with the height z. The spectral density function (8) is also used in Eurocode (1994). This spectral density function represents measured data well for moderately high frequencies, but some measurements indicate less accuracy in the low to medium frequency range. This is due to the fact that the spectral function (8) does not satisfy the

low frequency condition (7), but gives a theoretical length-scale of $1.7L$ corresponding to a too high value of the spectral density in the low frequency domain.

A different spectrum, due to von Karman (1948), gives better consistency between observed high and low frequency behaviour. The von Karman frequency spectrum is

$$R_n(z,n) = 4\frac{\Gamma(\frac{5}{6})\sqrt{\pi}}{\Gamma(\frac{1}{3})}\frac{f_L(z)}{(1+(2\pi f_L(z))^2)^{5/6}} = \frac{2.987 f_L(z)}{(1+(2\pi f_L(z))^2)^{5/6}} \qquad (9)$$

where the numerical constant corresponds to the high frequency parameter $A = 0.14$. The factor 2π converts the cyclic frequency to angular frequency, and thus the natural length-scale of the von Karman spectrum corresponds to the high frequency fit of the integral length-scale. The low frequency part of the von Karman spectrum leads to a theoretical length-scale of $0.75L$ corresponding to a too low value of the spectral density in the low frequency domain. Harris (1990) has proposed a modification of the von Karman spectrum that permits simultaneous fit of the high and low frequency parts, but it leads to a non-algebraic expression that is probably too complicated for typical structural design.

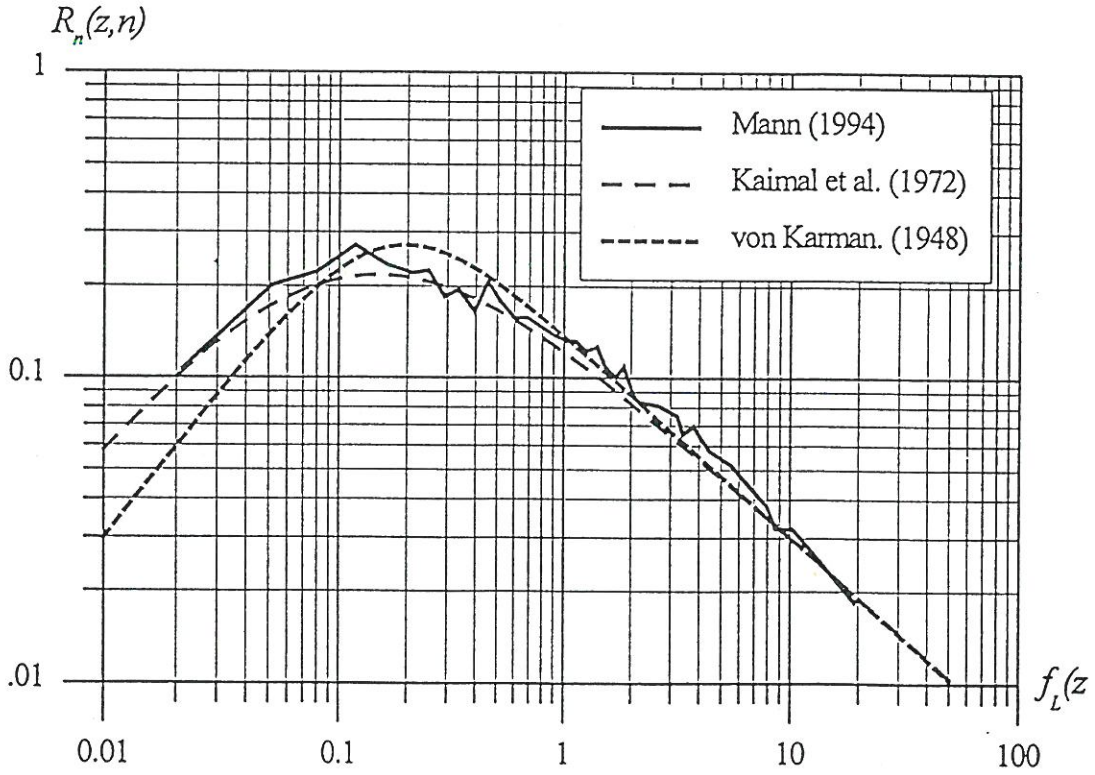

Figure 2. Non-dimensional spectral density functions. The integral length-scale for the measured data has been chosen in order to match the high-frequency range.

In Figure 2 the two non-dimensional spectral density functions (8) and (9) are compared with measured data from the Great Belt experiment, Mann (1994). The agreement between the Great Belt data and the Kaimal spectral density function is remarkably good in the entire frequency range.

Turbulence length-scale

The integral length-scale of the turbulence must be determined from full-scale measurements. The various results from such measurements show very large scatter, partly due to differences in the length and the degree of stationarity of the records used for the analysis. The integral length-scale may depend on the height z above terrain as well as the terrain roughness. Counihan (1975) suggested that the integral length-scale decreases with increasing surface roughness, while the opposite variation was described by ESDU (1985).

The integral length-scale depends on surface characteristics on a very long upstream fetch, say of the order of 50km. Except for offshore structures and structures within a few kilometres from the sea, the integral length-scale will be influenced in a complicated way by the variation of the terrain roughness. At present there does not seem to be any simple and accurate procedure available for the determination of the integral length-scale for terrain with surface roughness changes normally encountered in most practical design situations.

In most design situations the response only exhibits a moderate dependence on the integral length-scale. Thus the resonant part of the response of normal structures depends on the integral length-scale to the power -1/3, i.e. a slow decrease with increasing length-scale. This justifies the use of the following, conservatively estimated, integral length-scale

$$L(z) = L_{ref}\left(\frac{z}{z_{ref}}\right)^{0.3} \qquad 10\text{m} \le z \le 200\text{m} \tag{10}$$

with reference values $z_{ref} = 10\,\text{m}$ and $L_{ref} = 100\,\text{m}$, independent of surface roughness. This estimate is an approximate and simplified representation of ESDU (1985) data for smooth terrain with roughness lengths of the order of 1mm. The integral length-scale will probably be larger for terrains with larger roughness length, making (10) slightly conservative e.g. in cities.

The recent Eurocode 1 has adopted a considerable more elaborate specification of the integral length-scale based on older data from ESDU (1974). The full-scale measurements available do not seem to justify the complexity of Eurocode 1. Furthermore, later ESDU-updates indicate increasing integral length-scale with increasing surface roughness, i.e. just the opposite of the specifications given in Eurocode (1994) based on the work of Solari (1993).

Normalized co-spectrum

In the frequency domain, the spatial characteristics of the along-wind turbulence component is described by the normalized joint spectrum of the turbulent velocity components $u(x_1)$ and $u(x_2)$ at the two points x_1 and x_2,

$$\psi(x_1,x_2,n) = \frac{S_{uu}(x_1,x_2,n)}{\sqrt{S_u(x_1,n)S_u(x_2,n)}} \tag{11}$$

In general the normalized joint spectrum $\psi(x_1,x_2,n)$ may be complex and depend on all three arguments. The recent study by Mann (1994) indicates that the effect of blocking of the turbulent field by the terrain has only a moderate effect on the charactersitics of the turbulence. This supports the assumption that the normalized joint spectrum ψ depends on the points x_1 and x_2 only through their difference $x_2 - x_1 = (r_x, r_y, r_z)$. A complex value of ψ implies the existence of a phase angle corresponding to a systematic delay between the points x_1 and x_2. In the present context we are interested in points x_1 and x_2 lying in the same transverse plane. If the two points are at the same height, $z_1 = z_2$, symmetry implies that ψ is real. The anisotropy induced by the mean velocity gradient leads to a phase delay for points at different height, Mann (1994). However, no sufficiently simple representation seems to exist at the present time, and we shall therefore base the following considerations solely on the real part of ψ, the so-called normalized co-spectrum.

At the present time explicit theoretical results for the co-spectrum are restricted to homogeneous isotropic turbulence. In spite of the anisotropy of the turbulence of the natural wind the results from homogeneous isotropic turbulence suggest some basic properties of the normalized co-spectrum relating to its consistency. In isotropic homogeneous turbulence all cross-spectra can be expressed in terms of a single potential function and its first two derivatives, Krenk (1996). The results are formulated in terms of the wave number vector $k = (k_x, k_y, k_z)$, where the along-wind component is $k_x = 2\pi n / U$ due to the convection hypothesis, and the two transverse components k_y and k_z only appear in the form $\kappa^2 = k_y^2 + k_z^2$ due to symmetry. In particular the joint frequency spectrum of the along-wind velocity component for two points lying in the same transverse plane with distance r can be expressed in the form

$$S_{uu}(r,n) = \left(1 + \frac{r}{2}\frac{d}{dr}\right)\frac{2\pi}{U}\int_0^\infty 2E(k)\frac{J_1(\kappa r)}{\kappa r}\frac{\kappa^3 d\kappa}{k^4} \tag{12}$$

where k is the length of the wave number vector, $k^2 = k_x^2 + \kappa^2$, $J_1(\,)$ is the Bessel function of order one, and $E(k)$ is the energy density associated with wave numbers in the

interval $[k, k+dk]$. The differential operator in front of the integral has the effect that a polar area integral over the infinite transverse plane is identically zero, independent of the paticular form of the energy density function $E(k)$. Indeed, this is a necessary requirement for the turbulent velocity components $u(x)$ to have zero mean.

Additional information can be obtained by considering particular forms of the energy density function $E(k)$. In particular a generalized form of the von Karman spectrum is useful. The frequency spectrum has the form

$$S_u(n) = \frac{S_0}{(1+(k_x L)^2)^\gamma} = \frac{S_0}{(1+(2\pi nL/U)^2)^\gamma} \tag{13}$$

where the parameter γ determines the high frequency behaviour, and L is a length scale, and S_0 is a normalizing factor,

$$S_0 = 4\frac{\Gamma(\gamma)\sqrt{\pi}}{\Gamma(\gamma-\frac{1}{2})}\frac{L}{U}\sigma_u^2 \tag{14}$$

The high frequency behaviour (4) is obtained for $\gamma = 5/6$, and L as the integral length-scale. The energy density corresponding to the general spectrum (13) is

$$E(k) = \frac{Un^3}{4\pi}\frac{d}{dn}\left(\frac{1}{n}\frac{dS_u}{dn}\right) = \frac{U}{\pi}\frac{\gamma(\gamma+1)S_0(kL)^4}{(1+(kL)^2)^\gamma} \tag{15}$$

Substitution of this expression into (12) leads to the following explicit expression for the normalized co-spectrum, Krenk (1996)

$$\psi(r,n) = \left(1+\frac{r}{2}\frac{d}{dr}\right)\left[\frac{2}{\Gamma(\gamma)}\left(\frac{\kappa_x r}{2}\right)^\gamma K_\gamma(\kappa_x r)\right] \tag{16}$$

$K_\gamma(\,)$ is the modified Bessel function of the second kind, and κ_x is a wave number combining the frequency and the length scale L of the spectrum (13),

$$\kappa_x = \sqrt{k_x^2 + L^{-2}} = \sqrt{(2\pi n/U)^2 + L^{-2}} \tag{17}$$

A similar Bessel function expression for the normalized co-spectrum corresponding to $\gamma = 5/6$ has been investigated by Kristensen and Jensen (1979), and in asymptotic form by Harris (1970).

Direct use of the modified Bessel functions would require numerical methods. In view of the fact that the turbulence of the natural wind is anisotropic, it is desirable to extract the basic features of the result (16) in a simplified form, suitable for design calculations. The two basic features appear to be the integration requirement appearing via the differential operator, and the appearence of the wave number κ_x in the argument of the co-spectrum. Both of these features are retained if we consider the limit corresponding to $\gamma = 1/2$. In this limit the modified Bessel function is replaced by an exponential, $K_{1/2}(z) = \sqrt{\pi/2z}\, e^{-z}$, leading to the following normalized co-spectrum

$$\psi(r,n) = \left(1 + \frac{r}{2}\frac{d}{dr}\right)\exp(-\kappa_x r) = (1 - \tfrac{1}{2}\kappa_x r)\exp(-\kappa_x r) \qquad (18)$$

This simple function satisfies the integration requirement and leads to correlation less than one for all finite separation distances, due to the use of the wave number κ_x that retains a finite value for all frequencies. In the case of convected isotropic homogeneous turbulence the normalized co-spectrum is determined completely by the one-dimensional frequency spectral density $S_u(n)$. Thus, in the isotropic theory there is no room for additional parameters to determine the spatial characteristics, like the co-spectrum. In the natural wind the potential representation (12) is only an approximation, and the modified exponential format (18) may have introduced further approximations. While the principal features are retained, such as the change of sign and the role of the non-dimensional distance $\kappa_x r$, there is room for a scaling parameter and for differences between vertical and horizontal separation. In fact, calibration of the modified exponential format (18) to give the same integral length-scale as the general expression (16) with $\gamma = 5/6$ leads to the argument $0.7\kappa_x r$.

Available data for the co-spectrum show considerable scatter, and do not identify clearly the distance at which the sign changes. Traditionally an expónential format of the form

$$\psi_{exp}(r,n) = \exp(-Crn/U) \qquad (19)$$

has been used, and the parameter C has been calibrated from data in the near range, i.e. $rn/U < 0.2$. The exponential format (19) and the modified exponential format (18) would

have common tangent at zero distance for 'large' length scale and $C = \frac{1}{2}2\pi \approx 9.4$. This value is close to commonly used values, see e.g. Simiu and Scanlan (1986).

Eurocode 1 is based on the exponential normalised co-spectrum with a decay constant C=11.5 used for both vertical and horizontal separations. This value is considerable larger than decay constants normally used in building codes and leads to underestimated coherences in some situations, see e.g. Figure 3 for horizontal separations of 15m and 32.5m. Furthermore, some degree of conservatism is asked for due to the fact that pressures on the structure are better correlated than the longitudinal turbulence in the undisturbed, oncoming air flow.

Figure 3 shows measured values of the normalized co-spectrum at a mean wind velocity of approx. 22 m/s for horizontal separations r = 15.0, 32.5, 47.5m at height z = 70m from the Great Belt experiment, Mann (1994), and the co-spectrum according to the modified exponential format (18) with argument $\kappa_x r$ and the exponential format (19) with $C = 3\pi$. The measurements clearly indicate a downward shift associated with the length scale L=240m for increasing separation, and also suggest a change of sign around $\kappa_x r \approx$1.5-2.

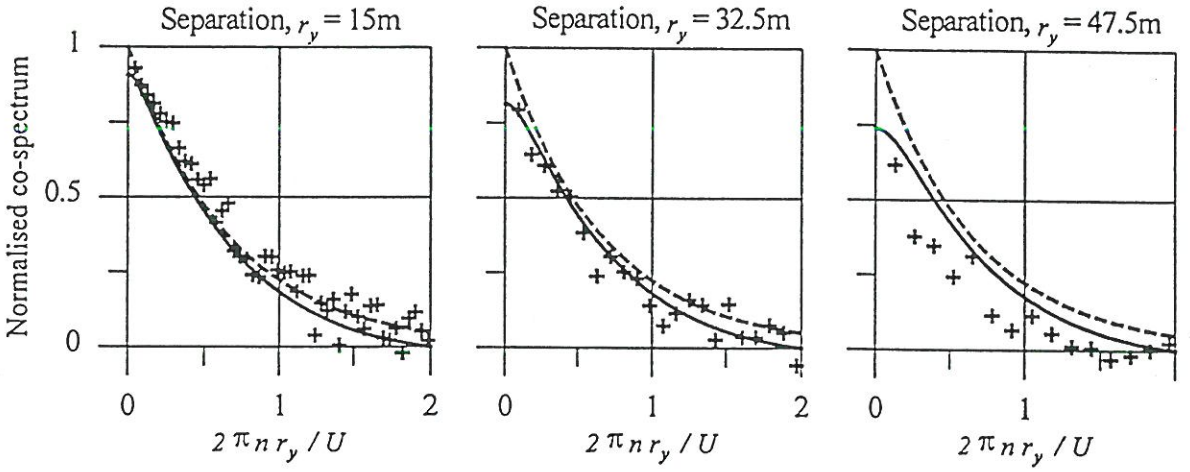

Figure 3. Normalised co-spectrum as a function of wave number $2\pi n/U$ multiplied by the separation r_y. The full-scale data are shown on the figure by +, the solid lines show the modified exponential format with $C_y = 2\pi$ and L=240m, and the exponential format with $C_y = 3\pi$ is given by the dotted lines.

A simple modification of the format to include different horizontal and vertical length scales is obtained by scaling the coordinates y and z with different decay constants C_y and C_z. The exponential format then is:

$$\psi_{exp}(r_y, r_z, n) = \exp\left(-\frac{n}{U}\sqrt{(C_y r_y)^2 + (C_z r_z)^2}\right) \tag{20}$$

The coherence function according to the modified exponential format can now be obtained by differentation according to (18) as:

$$\psi(y,z,n) = \left(1 + \frac{n_x}{2}\frac{d}{dn_x}\right)\psi_{exp} = \left(1 + \frac{n_x}{2}\frac{d}{dn_x}\right)\exp\left(-\frac{n_x}{U}\sqrt{(C_y r_y)^2 + (C_z r_z)^2}\right) \tag{21}$$

where the modified frequency n_x

$$n_x = \sqrt{n^2 + \left(\frac{U}{2\pi L}\right)^2} \tag{22}$$

has been used. Direct calculation gives the modified exponential coherence function as

$$\psi(r_y, r_z, n) = \left(1 - \tfrac{1}{2}\frac{n_x}{U}\sqrt{(C_y r_y)^2 + (C_z r_z)^2}\right)\exp\left(-\frac{n_x}{U}\sqrt{(C_y r_y)^2 + (C_z r_z)^2}\right) \tag{23}$$

At zero frequency the modified frequency takes the value $U/(2\pi L)$, where L is the integral length-scale. Consider as an example U=25 m/s at z=10m. This gives the minimum value $n_x \approx 0.04$Hz ($L \approx 100$m). Thus the difference between the actual frequency n and the modified frequency n_x given by (22) is mainly of interest for low frequency vibrations, e.g. of bridges.

Full-scale measurements carried out at many different sites show that the normalised co-spectrum decay constants depend on height above terrain, mean wind velocity and surface roughness. Fitting the modified exponential function to the normalised co-spectrum measured in the Great Belt experiment for a horizontal separation of 15m, see Figure 3, gives a decay constant of $C_y \approx 5$. Other normalized co-spectrum measurements carried out for points separated approx. 10m vertically also fits well to the modified exponential function using a decay constant of $C_z \approx 5$. The decay constants found for separations exceeding approx. 20m tend to be larger than 5, see Figure 3.

In practice it is often most convenient to derive the results corresponding to the modified exponential coherence function directly from those of the exponential format by differentiation with respect to the frequency according to (21). If results, e.g. for the joint

acceptance function, are available for the exponential format of the co-spectrum, the similar results for the modified exponential format can be obtained from these by differentiation. In this connection it is important to remember that the decay constants C_y and C_z of 5 determined for the modified exponential format using full-scale measurements with separations of the order of 10-20m, correspond to decay constants of $\frac{3}{2} \cdot 5 = 7.5$ in the exponential format, i.e. close to the deacy constant of 8 used by some building codes.

Correlation function

The spatial characteristics used calculating the low-frequency structural response based on a quasi-static approach is described by the correlation function, $\rho_u(r_y, r_z)$, of longitudinal turbulence components with zero time lag in a plane perpendicular to the mean wind direction. The correlation function is assumed to be of exponential form, i.e.

$$\rho_u(r_y, r_z) = \exp(-\sqrt{(r_y / L_u^y)^2 + (r_z / L_u^z)^2}) \tag{24}$$

r_y and r_z are the horizontal and vertical distance, respectively, between the two points considered, and L_u^y and L_u^z are integral length-scales estimated be means of full-scale measurements.

Evaluation of turbulent response

The fluctuating part of the structural response due to turbulent wind may be separated into a quasi-static contribution from low frequency background turbulence and one or more dynamic contributions from turbulence in resonance with the natural frequencies of the structure. The variance of the structural response is evaluated by integration over the structure, and the principal difference in the evaluation of the quasi-static and the dynamic contribution is that in the former the spatial integration is carried out only once, while in the dynamic contribution the spatial integration must in principle be carried out at each frequency. If an exponential form is assumed for both the correlation function and the normalised co-spectrum the response integrals of the quasi-static and the dynamic contributions take similar forms. Furthermore, the corresponding results for a modified exponential format can be obtained directly by differentiation.

In the following the formulation of background and resonance response of two-dimensional structures is briefly summarised. The characteristics of slender structures with full correlation across the width are identified and used to develop accurate explicit approximations for rectangular structures of arbitrary width. Finally, conversion of these formulas to the modified exponential format is discussed.

Response integrals for two-dimensional structures

The integrals presented in this section for background and resonance response can be used with different correlation functions, e.g. the exponential correlation form and the modified correlation form.

Background response

Typically, the bulk of variance in the longitudinal component of turbulence is at frequencies well below the natural frequencies of the structure. This indicates that the background turbulent response can be calculated , assuming that the wind load is quasi-static. This approach is simple and provides accurate response estimates in most situations.

The background turbulent response, $R_b(t)$, is calculated by:

$$R_b(t) = \int_A F_l(z,t)\eta(z)dA \tag{25}$$

in which $\eta(z)$ is the response-influence function equal to the response obtained for a unit static pressure applied at point $z=(y,z)$, and the fluctuating wind pressure caused by turbulence, $F_l(z,t)$, is given by:

$$F_l(z,t) = C(z)\rho U(z)u(z,t) \tag{26}$$

A is the structure area perpendicular to the wind direction, C is the shape factor, ρ is the air density, U is the mean wind velocity, and u is the along-wind turbulence component.

The variance σ_b^2 of the background response R_b is the expected value of R_b^2 obtained via a double integral over the structure. In normalised form:

$$\sigma_b^2 = (C_{ref}\rho U_{ref}\sigma_{u,ref}A)^2 \eta_{ref}^2 J_b^2 \tag{27}$$

in which the non-dimensional background response variance integral describing the interaction between air flow correlation and the response-influence function $\eta(z)$

$$J_b^2 = \frac{1}{A^2}\int_A\int_A \rho_u(r)g(z_1)g(z_2)dA_1dA_2 \tag{28}$$

is expressed in terms of the normalised background wind-load distribution function

$$g(z) = \frac{C(z)}{C_{ref}}\frac{U(z)}{U_{ref}}\frac{\sigma_u(z)}{\sigma_{u,ref}}\frac{\eta(z)}{\eta_{ref}} \tag{29}$$

The function g describes the distribution of the background wind turbulence and response-influence function over the structure, and $\rho_u(r)$ is the correlation coefficient for longitudinal turbulence components separated $r = (r_y, r_z)$, i.e. r_y horizontally and r_z vertically. The subscript *ref* refers to the function value at the reference point chosen.

Resonant response

The resonant part of the structural response due to the along-wind loading may be calculated by modal analysis. The response to gusty wind is usually dominated by the fundamental mode, and the corresponding generalised fluctuating load $Q(t)$ is:

$$Q(t) = \int_A F_l(z,t)\xi(z)dA \tag{30}$$

where $\xi(z)$ is the mode shape. The dynamic part of the structural deflection may be written as $a(t)\cdot\xi(z)$, where $a(t)$ is a stochastic amplitude function. The spectral density, $S_a(n)$, of $a(t)$ is proportional to the structural frequency response function squared, $|H(n)|^2$, and to the generalised load spectrum:

$$S_a(n) = (C_{ref}\rho U_{ref}\xi_{ref}A)^2|H(n)|^2\,|J(n)|^2 S_{u,ref}(n) \tag{31}$$

where the joint acceptance function $|J(n)|^2$, describing the interaction between air flow correlation at frequency n and structural mode shape, is calculated by the expression:

$$|J(n)|^2 = \frac{1}{A^2}\int_A\int_A \psi_u(r,n)g(z_1)g(z_2)dA_1dA_2 \tag{32}$$

using the non-dimensional resonant wind-load distribution function $g(z)$ defined as:

$$g(z) = \frac{C(z)}{C_{ref}}\frac{U(z)}{U_{ref}}\sqrt{\frac{S_u(z,n)}{S_{u,ref}(n)}}\frac{\xi(z)}{\xi_{ref}} \tag{33}$$

It is worth noting the resemblance between the joint acceptance function defined in equation (32) by means of the normalised co-spectrum $\psi_u(r,n)$ and the non-dimensional background response variance given by equation (28) based on the correlation function $\rho_u(r)$.

Variation in one dimension

For line-like structures the non-dimensional response variance J_h^2 in equation (28) is determined by a double integral over the structural length h. It can be converted to a single integral as shown by Dyrbye and Hansen (1988):

$$J_h^2 = \frac{1}{h}\int_0^h k(r)\rho_u(r)dr \tag{34}$$

where the co-influence function $k(r)$ is given as:

$$k(r) = \frac{2}{h}\int_0^{h-r} g(z)g(z+r)dz \tag{35}$$

All load pairs having a distance of r give a contribution to the non-dimensional response variance J_h^2 equal to $k(r)\rho_u(r)dr$. Equation (34) is simply an integral adding J_h^2 contributions originating from load pairs all having the distance of r.

Equation (34) can also be used to calculate the joint acceptance function by replacing the correlation function ρ_u with the normalised co-spectrum ψ_u, and using a co-influence function $k()$ determined by equation (35) with the distribution function $g()$ given in equation (33). Using the power spectral density functions of the longitudinal turbulence given by equations (8) or (9) indicates that the non-dimensional resonant wind-load distribution function $g()$, and thereby the co-influence function $k()$, is independent of the frequency n except for very low frequencies not important for the resonant response considered here.

Assuming an exponential form of $\rho_u(r)$, i.e. $\rho_u(r) = \exp(-r / L_u^r)$, the response variance integral $J_h^2(\phi)$ becomes a function of $\phi = h / L_u^r$. The exponential correlation form leads to the asymptotic behaviour $J_h^2(\phi) = k(0)/\phi$ for large values of ϕ. Similarly, the exponential form of the normalised co-spectrum gives a joint acceptance function $|J(\phi)|^2$ with an upper frequency limit of $|J(\phi)|^2 = k(0)/\phi$, see Davenport (1977). Here the joint acceptance function is a function of the parameter $\phi = Cnh / U_{ref}$, in which C is the normalised co-spectrum decay constant defined by (19).

Some examples of the functions $g()$, $k()$ are given in table 1 below. All co-influence functions $k(r)$ are equal to 0 for $r = h$. It should be noted, that $k(r)$ has a single root at $r = h$ for the height independent distribution function $g(z) = 1$ (first example), a double root of $r = h$ for the linear distribution function $g(z) = z$ (second example) and a triple root of $r = h$ for the distribution function $g(z) = z^2$ (third example).

Table 1. Non-dimensional distribution functions $g()$, co-influence functions $k()$ and coefficients G used in equations (40) and (46).

$g(z)$	$k(r)$, $s = r/h$	G
1	$2(1-s)$	1/2
z/h	$\frac{1}{3}(1-s)^2(2+s)$	3/8
$(z/h)^2$	$\frac{1}{15}(1-s)^3(s^2+3s+6)$	5/18
$\sin(\pi z/h)$	$(1-s)\cos(\pi s)+\sin(\pi s)/\pi$	$4/\pi^2$
$2z/h-1$	$\frac{2}{3}(1-s)(1-2s-2s^2)$	-

Two-dimensional response approximations for rectangular structures

When the lack of correlation along the structural width perpendicular to the mean wind direction is important, two-dimensional response calculations should be carried out. This aspect becomes significant when the structural width is of the same order of magnitude or larger than the wave length taken at the natural frequency, U/n_e.

Background response

The non-dimensional background response variance J_b^2 in equation (28) is determined by a four-fold integral over the structure width b and height h. It can be calculated as a double integral derived by a procedure similar to the one applied for line-like structures where double integrals are converted to single integrals:

$$J_b^2 = \frac{1}{bh}\int_0^h\int_0^b k(r_y,r_z)\rho_u(r_y,r_z)dr_y dr_z \tag{36}$$

The co-influence function $k(r_y,r_z)$ is given as:

$$k(r_y,r_z) = \frac{2}{bh}\int_0^{h-r_z}\int_0^{b-r_y}\Big(g(y,z)g(y+r_y,z+r_z)+g(y,z+r_z)g(y+r_y,z)\Big)dydz \tag{37}$$

All load pairs having a distance of r_y horizontally and r_z vertically give a contribution to the non-dimensional response variance equal to $k(r_y,r_z)\rho_u(r_y,r_z)dr_y dr_z$. Equation (36) is simply a double integral adding response variance contributions originating from load pairs all having the distances of r_y, r_z.

If the distribution function g can be written as $g(y,z) = g_y(y)g_z(z)$ the co-influence function k is given by $k(r_y,r_z) = k_y(r_y)k_z(r_z)$, where k_y and k_z are given in terms of one-dimensional characteristics based on line-like structures.

When the distribution function g in equation (29) has constant sign and the correlation function is of exponential form, see equation (24), a background response factor k_h with a value of 1 for full correlation can be defined as:

$$k_h = J_h^2 / \gamma_h^2 \tag{38}$$

The normalisation constant γ_h given by:

$$\gamma_h = \frac{1}{bh}\int_0^h\int_0^h g(y,z)dydz \tag{39}$$

is equal to J_h for full correlation with ρ_u=1 for all distances of interest. γ_h gives the integral effect of the distribution function g.

Assuming that $g(y,z) = g_y(y)g_z(z)$, the background response factor k_h can be approximated by the expression:

$$k_h(\phi_y,\phi_z) = \frac{1}{1+\sqrt{(G_y\phi_y)^2 + (G_z\phi_z)^2 + \left(\frac{2}{\pi}G_y\phi_y G_z\phi_z\right)^2}} \tag{40}$$

in which the non-dimensional parameters ϕ are given by the one-dimensional variations:

$$\phi_y = b / L_u^y \quad , \quad \phi_z = h / L_u^z \tag{41}$$

G values are obtained for line-like structures, see table 1 for typical g functions. G_y is obtained for $g = g_y$, and G_z is obtained for $g = g_z$. The asymptotic behaviour that gives the value of $2/\pi$ in the denominator of equation (40) is derived in (44) below.

Resonant response

Similar to the non-dimensional response variance, the joint acceptance function can be calculated by a double integral:

$$|J(n)|^2 = \frac{1}{bh}\int_0^h\int_0^b k(r_y,r_z)\psi_u(r_y,r_z,n)dr_y dr_z \tag{42}$$

in which the co-influence function k is given by equation (37) using the non-dimensional resonant wind load distribution function g defined in equation (33).

Assuming an exponential co-spectrum form, the joint acceptance function $|J(\phi_y,\phi_z)|^2$ becomes a function of the non-dimensional parameters $\phi_y = C_y nb/U_{ref}$ and $\phi_z = C_z nh/U_{ref}$ where C_y and C_z are the co-spectrum decay constants with horizontal and vertical separations, respectively.

For $n \to 0$ corresponding to large wavelengths in the air flow, the normalised exponential co-spectrum approaches 1 giving a joint acceptance function asymptote of:

$$|J(\phi_y,\phi_z)|^2 \to \frac{1}{hb}\int_0^h\int_0^b k(r_y,r_z)dr_y dr_z \tag{43}$$

For $n \to \infty$ corresponding to small wavelengths in the air flow, the correlation ψ_u is local, i.e. $r_y \approx r_z \approx 0$, and the joint acceptance function asymptote is given by:

$$|J(\phi_y,\phi_z)|^2 \to \frac{k(0,0)}{hb}\int_0^h\int_0^b \psi_u(r_y,r_z,n\to\infty)dr_y dr_z = \frac{\pi}{2}\frac{k(0,0)}{\phi_y\phi_z} \tag{44}$$

In the special case, where the function g is given as a product of the two one-dimensional functions, g_y and g_z, the factor of $\pi/2$ is the ratio between the plate-like joint acceptance function and the product of the two line-like joint acceptance functions for high frequencies of n. Using products of line-like joint acceptance functions, which is common

practice in most building codes, e.g. in Eurocode 1, may therefore lead to underestimated response estimates. Normally, this is taken into account using safe estimates of flow parameters, for instance of the normalised co-spectrum decay constants C_y and C_z. Here, the factor of $\pi/2$ is taken into account using the format given in (40) and (46).

Size reduction function for modes with constant sign

The size reduction function $K_S(\phi_y,\phi_z)$ accounts for the interaction between the wind turbulence and the structural mode of vibration. For modes having constant sign the size reduction factor approaches its maximum value for low frequencies, where the wind turbulence is best correlated over the structure. The correlation, and thereby the size reduction function, decreases for increasing frequency. The size reduction function is given by:

$$K_S(\phi_y,\phi_z) = \int_0^h\int_0^h k(r_y,r_z)\psi_u(r_y,r_z,\phi_y,\phi_z)\,dr_y\,dr_z \;/\; \int_0^h\int_0^h k(r_y,r_z)\,dr_y dr_z \qquad (45)$$

where the co-influence function k is given by equation (37) using the distribution function specified in equation (33).

The size reduction factor may be approximated by:

$$K_S(\phi_y,\phi_z) = \frac{1}{1+\sqrt{\left(G_y\phi_y\right)^2+\left(G_z\phi_z\right)^2+\left(\frac{2}{\pi}G_y\phi_yG_z\phi_z\right)^2}} \qquad (46)$$

in which the parameters of ϕ are equal to:

$$\phi_y = C_y bn/U_{ref} \quad , \quad \phi_z = C_z hn/U_{ref} \qquad (47)$$

where G_y and G_z are determined from the response of equivalent one-dimensional structures with horizontal length b and vertical height h, respectively. The approximation of the size reduction function has the correct asymptotes for frequencies approaching zero and infinity, respectively, see Figure 4.

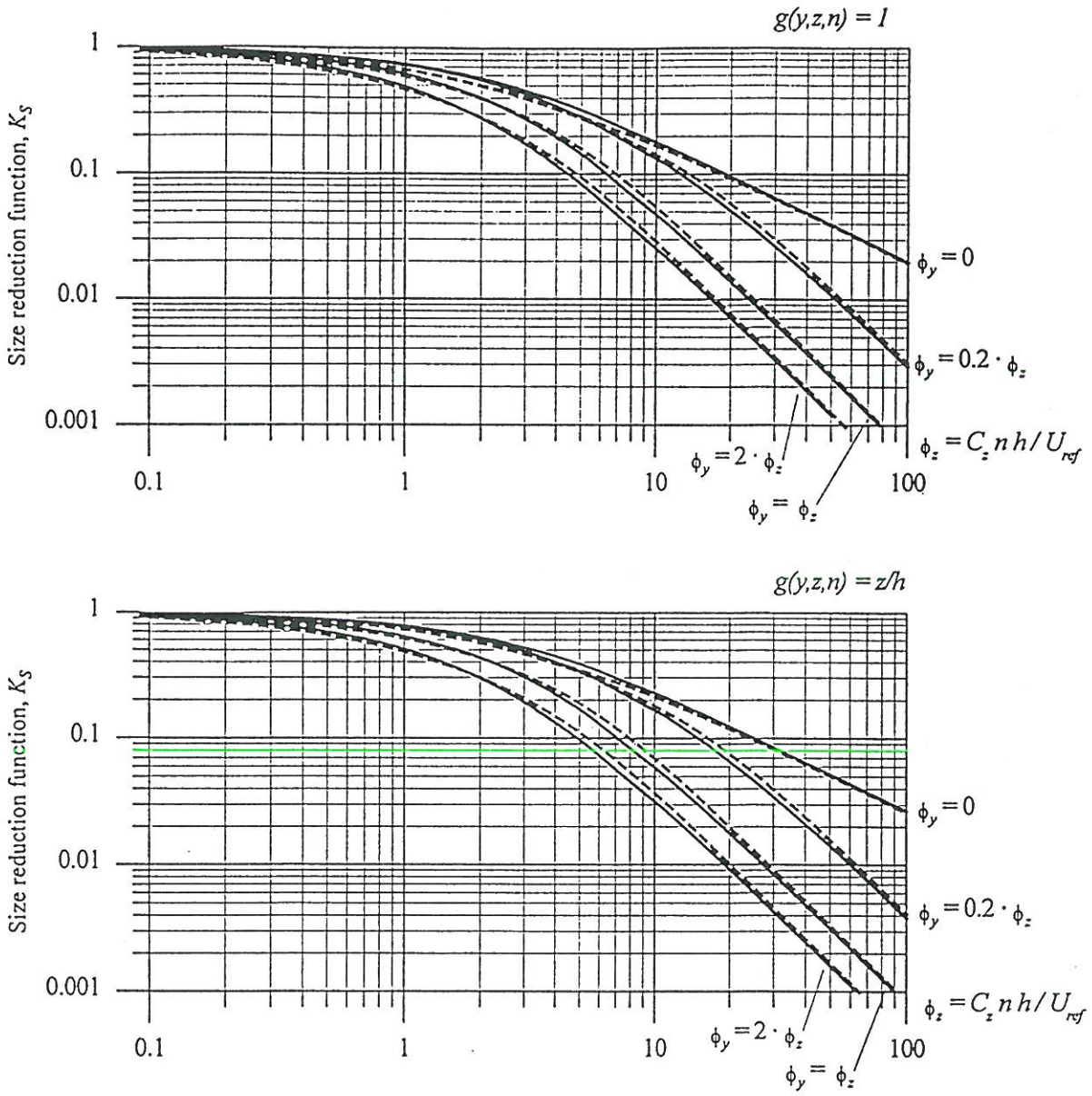

Figure 4. The solid and dotted lines show the size reduction function given in equation (45) and (46), respectively. The curves shown can also be interpreted as the background response factor k_b using $\phi_z = h / L_u^z$ and $\phi_y = b / L_u^y$.

Joint acceptance function for modes not having constant sign

For high frequencies corresponding to gusts much smaller than the structure, the interaction between the wind turbulence and structural modes not having constant sign follows the general features described for modes with constant sign. For low frequencies corresponding to large gusts of the same size or larger than the structure, the interaction between wind turbulence and structural modes not having constant sign is different from the features described for modes with constant sign.

Figure 5 shows the rather simplified variation given by the function $g_y(y) = 2y/b - 1$, i.e. a simple linear variation symmetrical with respect to the midpoint $y = b/2$. The height variation is described by $g_z(z) = 1$ and $g_z(z) = z/h$, respectively.

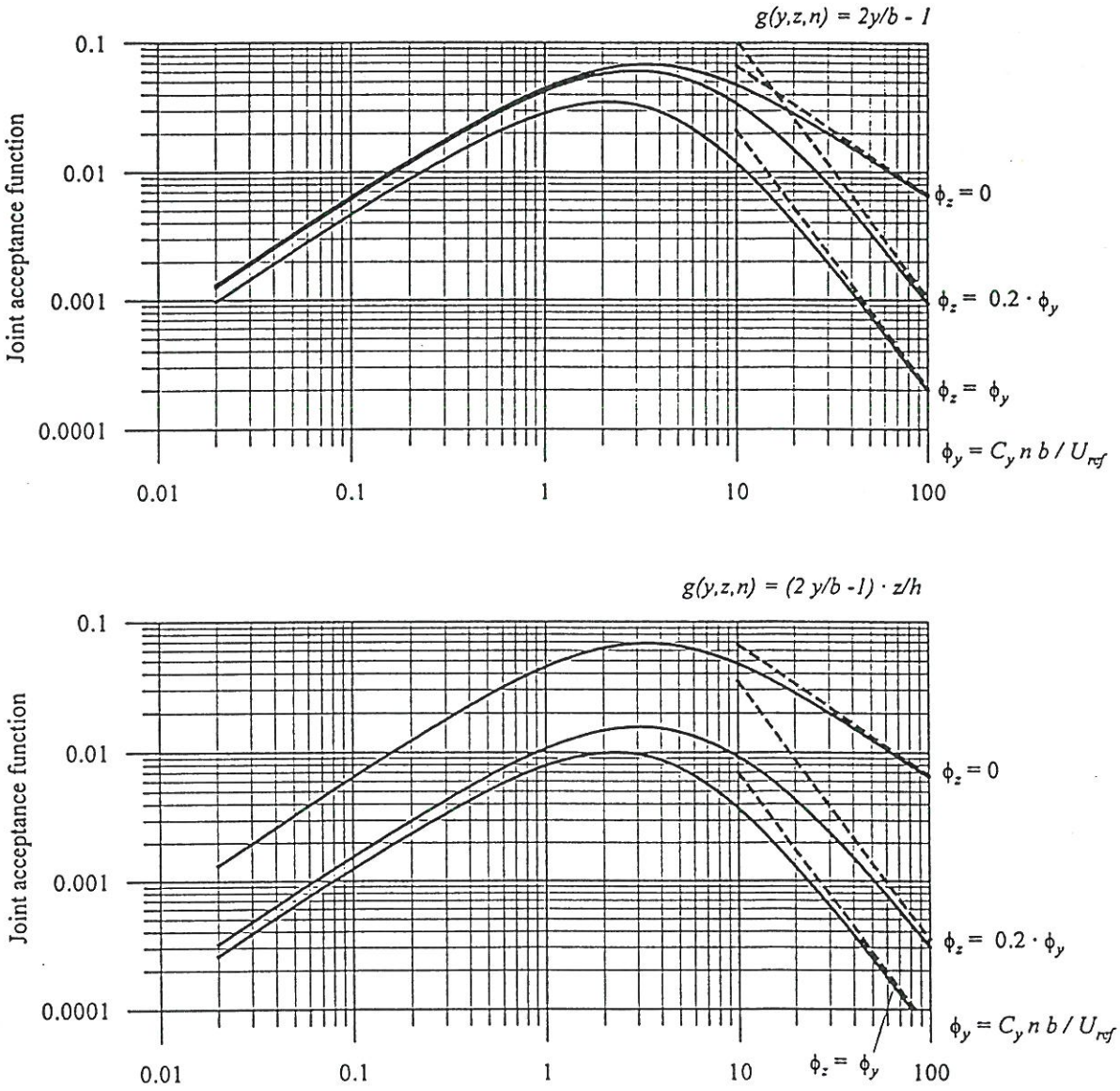

Figure 5. Joint acceptance function given in equation (42). The dotted lines give the asymptotic behaviour according to equation (44). The curves shown can also be interpreted as the non-dimensional response variance J_h^2 using $\phi_y = b / L_u^y$ and $\phi_z = h / L_u^z$.

High frequency reduction for modified exponential format

The spatial characterisics of the turbulence enters the response evaluation via the joint acceptance function $|J()|^2$ given by (32). So far the analysis has been based on the exponential representation (19) of the normalized co-spectrum. As already explained the normalized co-spectrum must integrate to zero over an infinite vertical plane. The asymptotic behaviour of the joint aceptance function for high frequencies is determined by the area integral of the co-spectrum over the structure, and it is therefore to be expected that a consistent representation of the normalized co-spectrum satisfying the integral requirement will reduce the joint acceptance function for high frequencies, Krenk (1996). We now demonstrate this reduction, and indicate how it can be incorporated directly into the approximate formula (46) for the size reduction factor.

The joint acceptance function is defined by the integral (32) of the normalized co-spectrum and the mode shape. Only the normalized co-spectrum depends on the frequency, and thus the joint acceptance function corresponding to the modified exponential format can be obtained from that of the exponential format by application of the differentiation (21) directly to the joint acceptance functions in the form

$$|J(n_x)|^2 = \left(1+\frac{n_x}{2}\frac{d}{dn_x}\right)\left|J_{\exp}(n_x)\right|^2 \tag{48}$$

where the frequency n_x given by (22) can be replaced by n except for large structures sensitive to very low frequencies. As already mentioned the decay parameters C_y and C_z used in the exponential format should be replaced with $\frac{2}{3}C_y$ and $\frac{2}{3}C_z$ in the modified exponential format.

Let us consider a one-dimensional structure of width b. The asymptotic behaviour for high frequencies of the joint acceptance function for the exponential format is

$$\left|J_{\exp}(n)\right|^2 \propto (G_y C_y bn/U_{ref})^{-1} \tag{49}$$

The asymptotic behaviour of the joint acceptance function corresponding to the modfied exponential format now follows by use of the differentiation formula (48) and replacement of the parameter C_y with $\frac{2}{3}C_y$. The result is that for high frequencies

$$|J(n)|^2 \cong \tfrac{1}{2}\tfrac{3}{2}\left|J_{\exp}(n)\right|^2 = \tfrac{3}{4}\left|J_{\exp}(n)\right|^2 \tag{50}$$

The first factor comes from differentiation and the second from using the parameter $\frac{2}{3}C_y$. The combined effect is a reduction of the joint acceptance function with a factor of 0.75 in the high frequency region. In the low frequency region there are two cases to consider. For mode shapes with constant sign the joint acceptance function approaches a constant value, independent of the parameter C_y, and thus the modification of the exponential format does not change the value of the joint acceptance function for low frequencies. For mode shapes that change sign the joint acceptance function is proportional to $G_y C_y bn / U_{ref}$ in the low frequency range. In this case the effects of differentiation and change of parameter cancel, leaving the low frequency behaviour of the joint acceptance function unchanged. Thus, it is concluded that the effect on the high and low frequency behaviour of the joint acceptance function for a one-dimensional structure of replacing the exponential co-spectrum (20) with the modified form (21) is a reduction with the factor 0.75 in the high frequency range, Krenk (1996).

The high frequency reduction factor of 0.75 was derived for one-dimensional structures from the integral consistency condition. In principle, the consistency condition implies that the asymptotic decay of the joint acceptance function for two-dimensional structures is of higher order. However, for large two-dimensional structures the assumption of wind loads based on the undisturbed wind may be questionable, and therefore it is proposed to incorporate the co-spectrum consistency requirement represented by the modified exponential format directly into the representation (46) of the size reduction factor by retaining the exponential decay constants C_y and C_z and replacing the parameters G_y and G_z with $\frac{4}{3}G_y$ and $\frac{4}{3}G_z$. For two-dimensional structures this represents a conservative estimate of the integral.

Design procedure

The largest structural response occurring during a storm period of 10 minutes is a sample in a statistical distribution with a mean value called the characteristic structural response. The characteristic structural response is determined by adding the 10-minute mean response and the estimated extreme response fluctuation occurring, the latter estimated as a peak factor multiplied by the standard deviation of the response fluctuations, see Madsen et al. (1986).

A design procedure following the principles described in this paper is outlined. The purpose of the design procedure is to calculate the so-called gust factor equal to the ratio between the characteristic structural response and the 10-minute mean structural response.

The reference heights of typical structures covered by the design procedure are shown in figure 6. The design procedure proposed covers structures with heights of up to 200m that have mode shapes with constant signs. The height limit of 200m is due to the simple logarithmic profile used in the design procedure. The design procedure given is not appropriate for dynamic analysis of guyed masts, continuous bridges, cable-stayed bridges and arch bridges.

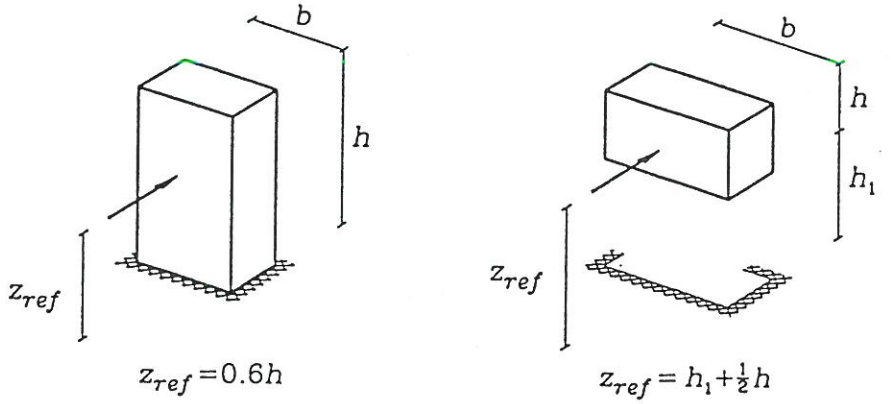

Figure 6. Reference heights of the structures covered by the design procedure proposed.

The structure considered has a vertical dimension h and a horizontal dimension b. If the width varies with height for a vertical line-like structure, the width of b at reference height z_{ref} shown in figure 6 should be chosen. If the structure is horizontal and line-like, the width of h at the centre point should be chosen.

Wind structure

The mean wind velocity at height z above ground, $U(z)$, is assumed to vary according to the logarithmic profile:

$$U(z) = U_{bas} \cdot k_T \cdot \ln(z / z_0) \tag{51}$$

where U_{bas} is the basic wind velocity that specifies the climate of the site, k_T is the terrain factor and z_0 is the roughness length.

The design procedure proposed uses the turbulence intensity given in equation (2), the correlation function given in equation (24) and the non-dimensional power spectral density function, $R_n(z,n)$, given in equation (8) being in good agreement with measured data at Great Belt, see Figure 2. The traditional exponential co-spectrum given in equation (20) is used with decay constants of C_y and C_z equal to 7.5 based on full-scale measurements at points with separations of the order of 10-20m. The value underestimate the decay constants for separations exceeding approx. 20m leading to slightly conservative design results for large structures. The reduction factor 0.75 in the high frequency range is incorporated by replacing the parameters G_y and G_z with $\frac{4}{3}G_y$ and $\frac{4}{3}G_z$.

Gust factor

The gust factor φ is defined as the ratio between a static wind load giving the maximum response of the structure occurring during a reference time interval, normally taken as 10 minutes, and the mean wind load giving the mean response of the structure. The gust factor is calculated from:

$$\varphi = 1 + k_p \, 2 I_u(z_{ref}) \sqrt{k_b + k_r} \tag{52}$$

where z_{ref} is a representative reference height. The peak-factor is the ratio between the peak and standard deviation of the fluctuating load, see equation (53). The first term represents the mean response and the second term the estimated peak of the fluctuating response. The background response factor accounts for the excitation from background turbulence and the resonant response factor gives the excitation from the turbulent fluctuations close to the natural frequency of the structure in the alongwind direction, see equation (57).

Peak factor

The peak factor is defined as the ratio between the peak and standard deviation of the fluctuating load within the reference time interval T. The peak factor is calculated as:

$$k_p = \sqrt{2\ln(\nu T)} + \frac{0.5772}{\sqrt{2\ln(\nu T)}} \tag{53}$$

where ν is the zero-upcrossing frequency and T=600 seconds is the averaging time for the reference wind velocity. The zero-upcrossing frequency ν is calculated from background and resonance contributions as:

$$\nu = \sqrt{\frac{n_0^2 k_b + n_1^2 k_r}{k_b + k_r}} \tag{54}$$

where n_1 is the natural frequency (Hz) for the alongwind vibrations of the structure and n_0 is the representative frequency (Hz) of the gust loading on rigid structures. The frequency n_0 is defined as:

$$n_0 = \sqrt{\frac{\int_0^\infty n^2 K_S(n) S_u(n, z_{ref}) dn}{\int_0^\infty K_S(n) S_u(n, z_{ref}) dn}} \tag{55}$$

where size reduction function $K_S(n)$ is given in equation (46). n_0 is approximated by:

$$n_0 = 0.3 \frac{U(z_{ref})}{\sqrt{hb}} \sqrt{\frac{\sqrt{hb}}{L_u^x}} \quad , \quad n_0 \le n_1 \tag{56}$$

in which the integral length scale $L_u^x = L(z_{ref})$ is given in equation (10). The approximation is not accurate for small areas of hb and estimates of n_0 should never exceed the natural frequency n_1. $\sqrt{hb}$ has been chosen as a characteristic dimension, according to the asymptotic behaviour of the size reduction function for frequencies approaching infinity. The approximation overestimates frequency n_0, and thereby the response, slightly.

Background response

The background response factor k_b taking the excitation from background turbulence into account is calculated by equation (40) assuming G_y=1/2 and G_z=3/8, see table 1, and $L_u^y = \frac{1}{3} L_u^x$ and $L_u^z = \frac{1}{4} L_u^x$.

Resonant response

The resonant response factor R giving the excitation from turbulent fluctuations close to the natural frequency of the structure is defined by:

$$k_r = \frac{\pi^2}{2\delta} R_n(z_{ref}, n_e) R_S(n_e) \tag{57}$$

where the non-dimensional spectral density $R_n(z_{ref}, n_e)$ is given in equation (8) and the size reduction factor $K_S(n_e)$ is given in equation (46). δ is the logarithmic damping decrement of the alongwind vibrations equal to:

$$\delta = \delta_s + \delta_a \tag{58}$$

where δ_s is the structural damping and the aerodynamic damping δ_a is:

$$\delta_a = \frac{C\rho U(z_{ref})}{2n_e\mu} \tag{59}$$

C is the shape factor, ρ is air density, $U(z_{ref})$ is mean wind velocity at the reference height and μ is the structural mass per unit of area taken at reference height, and for a horizontal line-like structure at the centre point. For line-like structures, the mass per unit of length is equal to μ multiplied by the structure width.

Examples

The design procedure calculations are illustrated for 3 structures: 1) a 150m tall concrete chimney, 2) a 100m long bridge and 3) a 50m tall, 20m wide building, see tables 2 and 3 below. Wind load and structural vibrations along the mean wind direction are considered. The natural frequencies and structural damping chosen for the three structures are based on experience. They should be estimated accurately for the particular structure in question.

The g-functions assumed are as follows:

Structure 1: $g_y = 1$, $g_z = (z/h)^2$.

Structure 2: $g_y = \sin(\pi y/b)$, $g_z = 1$.

Structure 3: $g_y = 1$, $g_z = z/h$.

The chimney site is characterised as farmland, the bridge is assumed to be 50m above sea level and the building is located in suburban terrain.

The gust factor calculated in the design procedure is used to determine the characteristic bending moment at the chimney and building foundations and at midspan of the bridge.

The gust factors of approximately 2 calculated by the design procedure indicate that the 10-minute mean response is of the same order of magnitude as the extreme fluctuations of the response.

The calculations show that the resonant response k_r is largest for the 150m tall concrete chimney having the lowest natural frequency of the three structures considered. The resonant response k_r is approximately twice the background response k_b indicating that the high frequency response reduction introduced by the modified exponential function is significant for the concrete chimney response estimate.

The relatively large natural frequencies assumed for the bridge and building give relatively low resonant response. The background response is dominating making the accurate low-frequency response obtained by the present design procedure useful.

Table 2. Input parameters specifying the wind climate, terrain and structural characteristics.

Wind climate		Struc. 1	Struc. 2	Struc. 3
Reference wind velocity U_{bas} (m/s)	(51)	25	25	25
Air density ρ (kg/m³)		1.25	1.25	1.25
Site specifications				
Roughness length z_0 (m)	(51)	0.05	0.01	0.3
Terrain factor k_T	(51)	0.19	0.17	0.22
Structure specifications				
Horizontal dimension b (m)	Fig. 6	6	100	20
Vertical dimension h (m)	Fig. 6	150	5	50
Natural frequency n_1 (Hz)		0.3	1.0	0.9
Logarithmic decrement δ_s		0.06	0.04	0.08
Mass per unit of area μ (kg/m²)		700	1000	500
Shape factor C		0.6	1.0	1.2

Table 3. The results calculated were obtained using the design procedure specifications indicated in the table. The mode shape coefficients given in Table 1 have been multiplied with 4/3 taking into account the high frequency reduction for modified exponential format.

Design parameters		Struc. 1	Struc. 2	Struc. 3
Reference height z_{ref} (m)	Fig. 6	90	50	30
Mean wind velocity $U(z_{ref})$ (m/s)	(48)	35.6	36.2	25.3
Turbulence intensity $I_u(z_{ref}) = I_{u,ref}$	(2)	0.133	0.117	0.217
Integral length scale $L_u = L_u^x(z_{ref})$ (m)	(10)	193	162	139
Aerodynamic damping δ_a	(59)	0.064	0.023	0.042
Total damping δ	(58)	0.124	0.063	0.122
Background response frequency n_0 (Hz)	(56)	0.140	0.180	0.115
Background response k_b	(40)	0.462	0.519	0.631
Spectral density function $R_n(z_{ref}, n_1)$	(8)	0.093	0.050	0.047
Mode-shape coefficient G_y	Table 1	0.667	0.540	0.667
Non-dimensional parameter ϕ_y	(47)	0.380	20.7	5.33
Mode-shape coefficient G_z	Table 1	0.371	0.667	0.500
Non-dimensional parameter ϕ_z	(47)	9.45	1.04	13.4
Size reduction factor $K_S(n_1)$	(46)	0.219	0.075	0.056
Resonant response k_r	(57)	0.813	0.299	0.107
Zero-upcrossing frequency ν (Hz)	(54)	0.254	0.622	0.359
Peak factor k_p	(53)	3.35	3.61	3.45
Gust factor φ	(52)	2.01	1.77	2.29

CONCLUSION

The dynamic alongwind response to gusty wind has been considered for simple line-like and plate-like structures. The formulation presented includes simple exponential coherence functions as well as more accurate expressions, where the coherence does not approach unity for small frequencies, when the separations are of the same size or larger than the turbulent length scale.

The integration format given in the paper is based on co-influence functions. The format leads to considerable computational reductions compared to common practice.

A simple expression of the size reduction function for plate like structures has been presented. The formula combines the one-dimensional size parameters into an asymptotically correct format giving better accuracy than the traditional product format. It may conveniently be used in new codes improving their accuracy without introducing any extra complexity.

ACKNOWLEDGEMENT

This work has received partial support from the Danish Technical Research Council.

REFERENCES

Abramowitz, M. and Stegun, I. (eds.) (1964), *Handbook of Mathematical Functions*. National Bureau of Standards, Applied Mathematics Series.

Batchelor, G.K. (1953), *The Theory of Homogeneous Turbulence*, Cambridge University Press, Cambridge.

Counihan (1975), Adiabatic Atmospheric Boundary Layers: A Review and Analysis of Data from the Period 1880-1972, *Atmospheric Environment*, 9, pp. 871-905.

Davenport, A.G. (1962), The response of slander line-like structures to a gusty wind, *Proceedings of the Institution of Civil Engineers*, London, 23, pp. 389-408.

Davenport, A.G. (1977), The prediction of the response of structures to gusty wind, in *Safety of Structures under Dynamic Loading*, Holand, Kavlie, Moe and Sigbjörnsson (eds.), pp. 257-284. Tapir, Trondheim.

Dyrbye, C. and Hansen, S.O. (1988), Calculation of Joint Acceptance Function for line-like structures, *Journal of Wind Engineering and Industrial Aerodynamics*, **31**, pp. 351-353.

ESDU (1974), *Characteristics of atmospheric turbulence near the ground. Part II : single point data for strong winds (neutral atmosphere)*, Engineering Science Data Unit 74031, London, England.

ESDU (1985), *Characteristics of atmospheric turbulence near the ground. Part II : single point data for strong winds (neutral atmosphere),* Engineering Science Data Unit 85020, London, England.

Eurocode (1994) *Eurocode 1: Basis of Design and Actions on Structures, Part 2-4: Wind Actions*, CEN, European Committee for Standardization, Brussels.

Harris, R.I. (1970) The nature of the wind, in *Seminar on Modern Design of Wind-Sensitive Structures, 1970*, pp. 29-55. Construction Industry Research and Information Association, CIRIA, London.

Harris, R.I. (1990), Some further thoughts on the spectrum of gustiness in strong winds, *Journal of Wind Engineering and Industrial Aerodynamics*, 33, pp.~461--477.

Kaimal, J.C., Wyngaard, J.C., Izumi, Y. and Coté, O.R. (1972), Spectral characteristics of surface-layer turbulence, *Journal of the Royal Meteorological Society*, 98, pp. 565-589.

Krenk, S. (1996), Wind field coherence and dynamic wind forces, in *Advances in Nonlinear Stochastic Mechanics*, Naess and Krenk (eds.), Kluwer, Doordrecht.

Kristensen, L. and Jensen, N.O. (1979), Lateral coherence in isotropic turbulence and in the natural wind, *Boundary-Layer Meteorology*, 17, pp. 353-373.

Madsen, H.O., Krenk, S. and Lind, N.C. (1986), *Methods of Structural Safety*, Prentice-Hall, Englewood Cliffs, NJ.

Mann, J. (1994), The spatial structure of neutral atmospheric surface-layer turbulence, *Journal of Fluid Mechanics*, 273, pp. 141-168.

Mann, J. and Krenk, S. (1994), Fourier simulation of a non-isotropic wind field model, in *Structural Safety and Reliability*, Schueller, Shinozuka and Yao (eds.), pp. 1669-1674. Balkema, Rotterdam.

Mann, J., Kristensen, L. and Courtney, M.S. (1991), *A study of atmospheric turbulence over water*, Risø National Laboratory, Report R-596, pp. 51, Roskilde, Denmark.

Simiu, E and Scanlan, R.H. (1986) *Wind Effects on Structures, Second Edition.* Wiley, New York.

Solari, G. (1993a) Gust buffeting I: Peak wind velocity and equivalent pressure, *Journal of Structural Engineering*, 119, pp. 365-382.

Solari, G. (1993b) Gust buffeting II: Dynamic alongwind response, *Journal of Structural Engineering*, 119, pp. 383-398.

Von Kármán, T. (1948), Progress in the statistical theory of turbulence, *Journal of Maritime Research*, 7.

Computational Investigation of Repetitive Vertical Human Loading

Jeppe Jönsson, ES-Consult A/S, Staktoften 20, 2950 Vedbæk

Analytical expressions for the spectral distribution of repetitive vertical human loading, mainly jumping, are validated through the use of simulated discrete time series of the load. The simulation is performed on the basis of halfsine impulse shapes and experimentally determined mean values and standard deviations of the pulse period, the pulse starting time and the contact duration. The simulations shows that the developed analytical expressions for the spectral load distribution are adequate. However the use of halfsine impulses has to be modified in order to include the influence of heel impact in the high frequency domain of the load spectrum.

Introduction

The loads produced by humans vary a great deal and new motion patterns on for example sports stadiums or in keep fit gymnastics may develop. Knowledge of the loads are needed in order to perform structural analysis in the ultimate limit state and in order to fulfil the requirements in the serviceability state. A literature survey is given by Per-Erik Eriksson in his work on *Vibration of Low-Frequency Floors* from 1994, [1]. The Swiss researchers Bachmann and Ammann give many valuable references and a thorough treatment of man induced vibrations in [2]. Stochastic load models giving the spectral density distribution of loads have been proposed, see for example Rebelo and Schere [3] and specially the work by Per-Erik Eriksson [1]. An investigation of the mechanics of repetitive human motion has recently been performed by Jönsson and Pilegaard Hansen in [4], this work resulted in different analytical expressions for approximate spectral load distributions. These analytical spectra are validate by simulations, some of which are presented in this paper. An experimental investigation has also been performed by Jönsson and Pilegaard Hansen in [5]. It involves one person performing 5 different repetitive vertical motions on a very stiff loading platform with eigenfrequencies above 60 Hz.

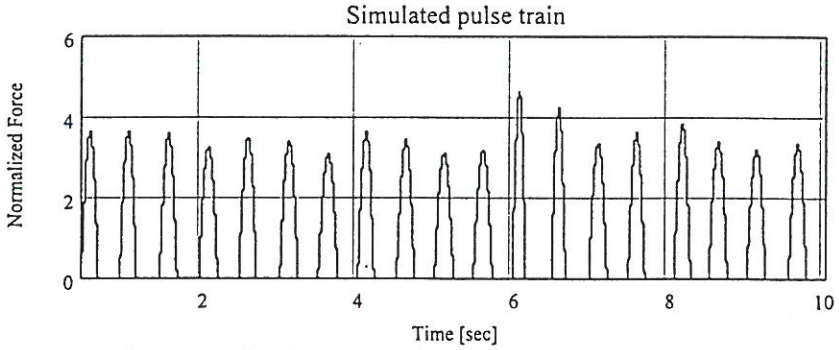

Figure 1. Simulated repetitive vertical human load.

Simulated repetitive vertical human load

A halfsine impulse shape function is introduced and the load amplitude is determined by the periodic load impulse of the contact force $I=MgT_p$. Using the unit function $u(t)$ a single load pulse is given by

$$f(t, t_p, T_p) = \frac{\pi}{2} \frac{MgT_p}{t_p} \sin(\frac{\pi t}{t_p})\ u(t)\ u(t_p - t) \qquad (1)$$

A pulse train is defined as a series of n impulses using the load impulse function defined above however we will include an additional impulse starting time t_s within each period as follows

$$h(t, t_s, t_p, T_p, n) = \sum_{j=0}^{n-1} f\left(t - t_{sj} - \Sigma_{k=1}^{j} T_{pk}, t_{pk}, T_{pk}\right) \qquad (2)$$

The pulse periods T_{pk}, the contact durations t_{pk} and the pulse starting times t_{sk} are random data which follow a normal probability distribution. Note that the mean impulse starting time is zero, $\bar{t}_s$=0. The simulated load shown in figure 1 and in the following figures corresponds to jumping at a frequency of 2Hz with a contact duration ratio of 0.45 and standard deviations of 0.02sec for the impulse starting time or the pulse period and the contact duration.

Discrete force amplitude spectra

The pulse train is used to simulate about 10 seconds of experimentally measured data by discrete evaluation at a sampling frequency of f_s=600Hz. The m simulated measured loads h_r are Fourier transformed using a discrete complex fast Fourier transform. The transformed load data are then used to find the single sided force amplitude spectrum A_r shown in figure 2 as follows

$$h_r = \sum_{j=0}^{n-1} f\left(t_r - t_{sj} - \Sigma_{k=1}^{j} T_{pk}, t_{pk}, T_{pk}\right), \quad H_r = \frac{1}{m}\sum_{k=0}^{m-1} h_k e^{-i\frac{2\pi r}{m}k}, \quad A_r = 2\sqrt{H_r H_r^*} \qquad (3)$$

Before Fourier transforming the data it is treated as if it were real measured data as in [5].

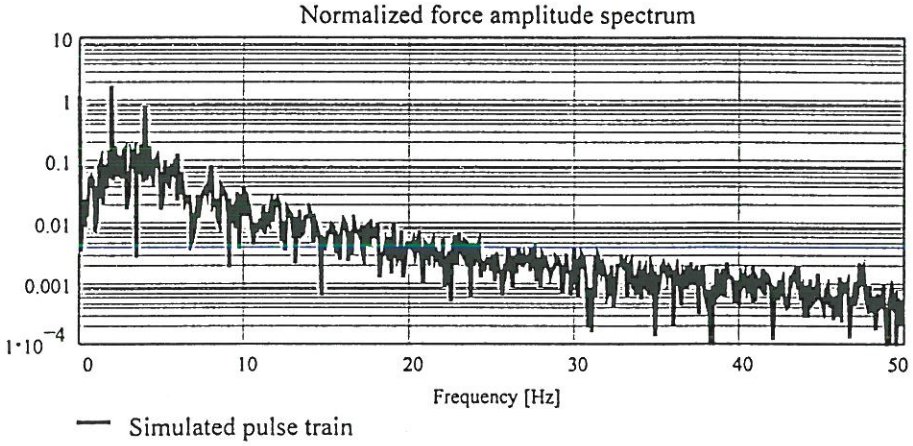

Figure 2. Normalized force amplitude spectrum of simulated human loading.

Analytical force amplitude spectra

The following four load models are analyzed and the corresponding normalized load spectra are shown in figures 3 and 4.

I. A deterministic model using mean values $T_{pk}=\bar{T}_p$, $t_{pk}=\bar{t}_p$ and $t_{sk}=\bar{t}_s=0$.

II. A model where the impulse starting time t_{sk} is stochastic and the remaining variables are deterministic, ie $T_{pk}=\bar{T}_p$ and $t_{pk}=\bar{t}_p$.

III. A model with a deterministic impulse $I=Mg\bar{T}_p$, but where the pulse period T_{pk} is stochastic, the contact duration as well as the impulse starting time are deterministic, ie $t_{pk}=\bar{t}_p$ and $t_{sk}=0$.

IV. A model where the impulse starting time t_{sk} and the contact duration t_{pk} are stochastic and the the pulse period is deterministic, $T_{pk}=\bar{T}_p$.

In the following we will state the analytical results found in Jönsson and Pilegaard Hansen [4] for each of the above given models, however before doing so we need to introduce a few functions. The Fourier transform of a pulse train normalized by the time period $n\bar{T}_p$ is approximated by assuming that the impulses are determined by the mean pulse period as $I=Mg\bar{T}_p$. The approximate Fourier transform is

$$H(\omega, t_s, t_p, T_p, n) \approx \frac{1}{n\bar{T}_p}\int_{-\infty}^{\infty} \sum_{j=0}^{n-1} f\left(t - t_{sj} - \Sigma_{k=1}^{j} T_{pk}, t_{pk}, \bar{T}_p\right) e^{-i\omega t} dt \qquad (4)$$

The Fourier transform of the impulse function normalized by the pulse period T_p is introduced as

$$F(\omega,t_p) = \frac{1}{T_p}\int_{-\infty}^{\infty} f(t,t_p,T_p)e^{-i\omega t}dt = -\frac{1}{2}Mg\,\frac{\pi^2}{\omega^2 t_p^2-\pi^2}\,(1+e^{-i\omega t_p}) \tag{5}$$

The "length" of the fourier transform of the impulse function is

$$|F(\omega,t_p)| = \sqrt{FF^*} = \frac{1}{2}Mg\,\frac{\sqrt{2}\pi^2}{|\omega^2 t_p^2-\pi^2|}\sqrt{1+\cos(\omega t_p)} \tag{6}$$

Further more we need the normal probability distribution $p(x)$, its Fourier transform $P_x(\omega)$ and its length $|P_x(\omega)|$ for the variable x with a mean value μ_x and a standard deviation of σ_x as follows

$$p(x)=\frac{1}{\sigma_x\sqrt{2\pi}}e^{-\frac{(x-\mu_x)^2}{2\sigma_x^2}}, \quad P_x(\omega)=e^{-\frac{1}{2}\omega^2\sigma_x^2}e^{-i\omega\mu_x}, \quad |P_x(\omega)|=\sqrt{P_xP_x^*}=e^{-\frac{1}{2}\omega^2\sigma_x^2} \tag{7}$$

In the following we also use a spectral factor $N(\omega,n)$ and its length defined as

$$N(\omega,n)=\frac{1}{n}\sum_{j=0}^{n-1}e^{-i\omega jT_p}=\frac{1}{n}\frac{1-e^{-i\omega nT_p}}{1-e^{-i\omega T_p}}, \quad |N(\omega,n)|=\frac{1}{n}\sqrt{\frac{1-\cos(\omega nT_p)}{1-\cos(\omega T_p)}} \tag{8}$$

The force amplitude spectra of a pulse train of n pulses is found by use of the mean power spectrum as

$$\tilde{A}(f,n) = 2\sqrt{\overline{HH^*}} \tag{9}$$

The force amplitude spectra of the four load models can be written as follows, see [4],

$$A_I(f,n) = 2\;|N(2\pi f,n)|\;|F(2\pi f)|$$

$$A_{II}(f,n) = 2\sqrt{|P_{t_s}(2\pi f)|^2\,|N(2\pi f,n)|^2+\frac{1}{n}-\frac{1}{n}|P_{t_s}(2\pi f)|^2}\;\;|F(2\pi f)|$$

$$A_{III}(f,n) = 2\sqrt{\frac{1}{n}+2Re\left(P_{T_p}(2\pi f)\frac{n(1-P_{T_p}(2\pi f))-(1-P_{T_p}^n(2\pi f))}{n^2(1-P_{T_p}(2\pi f))^2}\right)}\;|F(2\pi f)| \tag{10}$$

$$A_{IV}(f,n) = 2\sqrt{|P_{t_s}(2\pi f)|^2\,|N(2\pi f,n)|^2+\frac{1}{n}-\frac{1}{n}|P_{t_s}(2\pi f)|^2}\;\sqrt{\overline{FF^*}}$$

For model IV it is necessary to evaluate the mean power spectrum for a single pulse numerically since an analytical result has not been found.

$$\overline{FF^*} = \int_{-\infty}^{\infty} F(\omega,t_{pj})\,F^*(\omega,t_{pj})\,p(t_{pj})\;dt_{pj} \tag{11}$$

Thus the evaluation is eased by using the Fourier transform of the halfsine load pulse.

Concluding remarks

The quality of the stochastic load models reflect their simplicity, model II is the simplest, then comes model III and finally model IV. A remaining topic is how to include the influence of a heel impact. It is proposed that the individual impulse is decomposed into a 95% halfsine impulse with the measured contact duration t_p and a 5% heel halfsine impact with a short contact duration of $0.2t_p$. The impulse of the heel impact can be estimated using the level of the force amplitude at high frequencies.

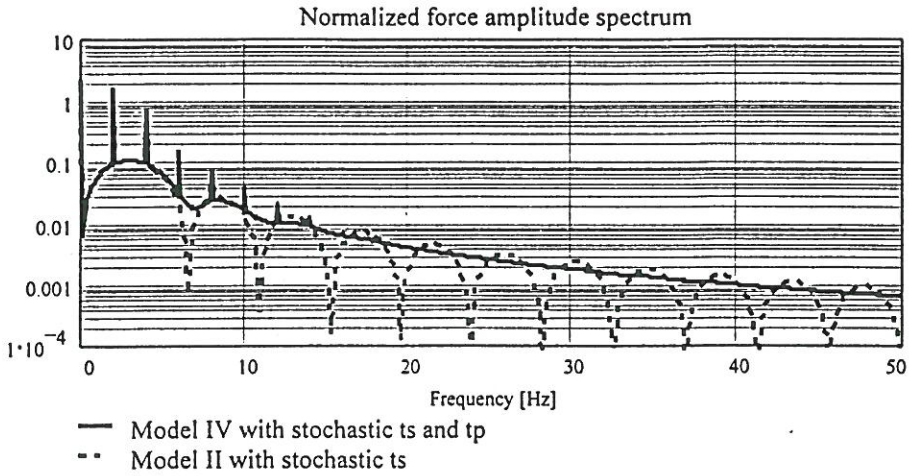

Figure 3. Analytical normalized force amplitude spectra for model II and IV.

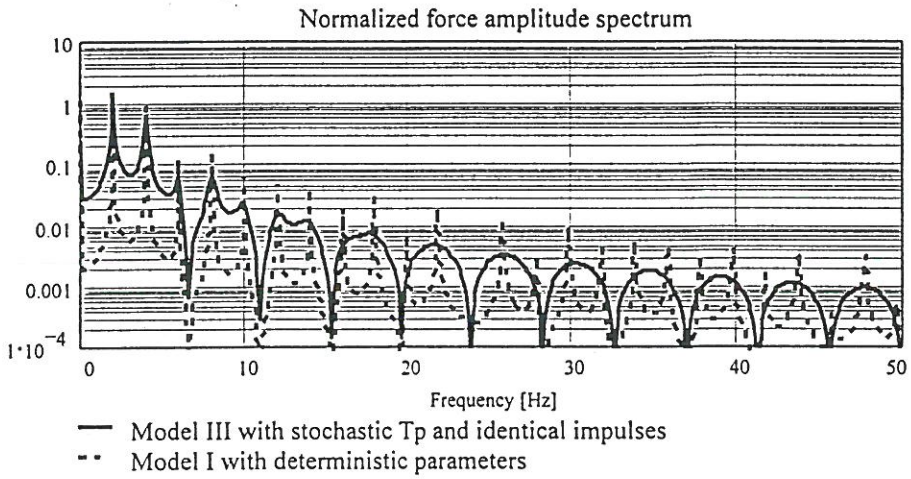

Figure 4. Analytical normalized force amplitude spectra for model IV and I.

Acknowledgement

The present work has been performed within the framework of a research program on dynamics of structures, covering dynamic loads and response of structures and foundations, sponsored by the Danish Technical Research Council. The present project has the title *C.3 Man Induced Vibrations*.

References

[1] P.-E. Eriksson. Vibration of Low-Frequency Floors - Dynamic Forces and Response Prediction. Ph.D. dissertation, Chalmers University of Technology, Unit for Dynamics in Design, Göteborg, Sweden, Publication D94:3, 1994.

[2] H. Bachmann and W. Ammann. *Vibrations in Structures- Induced by Man and machines. Structural engineering Documents*. IABSE, ETH-Hönggerberg, CH-8093 Zurich, Switzerland, 1987.

[3] C. Rebelo and R. J. Scherer. A stochastic model for human induced rhythmic loads. *Structural Safety & Reliability*, Schuëller, Shinozuka & Yao (eds), Balkema, Rotterdam, 1994.

[4] J. Jönsson & L. Pilegaard Hansen, *Repetitive vertical human loading, Part I - Theoretical investigation*, to be published at Dept. of Building Technology and Structural Engineering, Aalborg University, Denmark, 1996.

[5] J. Jönsson & L. Pilegaard Hansen, *Repetitive vertical human loading, Part II - Experimental investigation*, to be published at Dept. of Building Technology and Structural Engineering, Aalborg University, Denmark, 1996.

AN APPROACH TO DESIGN AGAINST CROSS-FLOW VIV FOR SUBMARINE PIPELINES

Kim J. Mørk
Det Norske Veritas
Norway

Luigino Vitali
Snamprogetti SpA
Italy

ABSTRACT

The present paper provides an overview of the DNV Design Guideline for design of free spanning pipelines against Vortex Induced Vibrations (VIV) developed within the MULTISPAN project.

The MULTISPAN research project was established with the objective to provide rational criteria and guidance on design methods for unevenness-induced free spans subjected to current induced VIV.

The proposed design format apply a limit state and partial safety factor methodology (often denoted LRFD) with a reliability based calibration of partial safety factors. The safety philosophy adopted is in compliance with the new DNV'96 Pipeline Rules.

The present paper focuses on the premises for the technical development of the limit state for onset of cross flow vibrations, hydrodynamic model, probabilistic modelling and reliability study performed within the MULTISPAN project.

INTRODUCTION

The MULTISPAN project is a Joint Industry R&D Project sponsored by Statoil and Norsk Agip and performed by Danish Hydraulic Institute, Det Norske Veritas, SINTEF and Snamprogetti. The Design Guideline issued by DNV is based on the research performed in the MULTISPAN Project. A thorough presentation of the motivation and scope for the entire MULTISPAN project is given in Moshagen *et al*, 1997.

The objective of the Design Guideline task is to provide rational criteria and guidance on design methods for unevenness-induced free spans subjected to vortex induced vibrations from steady on-bottom current loading. A comprehensive overview of the DNV Design Guideline covering the following design criteria:

- Onset of cross-flow VIV, and
- Fatigue due to in-line VIV,

as well as structural modelling requirements is presented in Mørk *et al.*, 1997.

The premises, modelling and analysis discussed herein are restricted to the developed criterion for onset of cross-flow.

Cross-flow VIV are affected by several parameters, such as the reduced velocity V_R, the stability parameter K_S, the seabed gap ratio (e/D), the pipe specific mass (ρ_s /ρ), the Strouhal number S_t, the Reynolds number R_e, and the pipe roughness (k/D) among others. The effect of these parameters is thoroughly discussed in Vandiver, 1993.

Onset of cross-flow VIV of significant amplitude occurs typically at a value of V_R between 3.0 and 5.0, whereas maximum amplitude vibrations occurs at a value between 5.0 and 7.0. The reduced velocity V_R is defined as:

$$V_R = \frac{U_n}{f_0 D} \qquad (1)$$

where D is outer pipe diameter, f_0 is a natural frequency for a given vibration mode and U_n is a flow velocity normal to the pipe.

The maximum amplitude of VIV is for given V_R mainly affected by the stability parameter K_S and, as a rule of thumb, cross-flow VIV are 10 times larger than the in-line VIV. For a low damped free span (K_S<0.1) the maximum amplitude of cross-flow VIV is larger than the pipe diameter. For a short free span, say L/D<100, this may give rise to large dynamic stress variations causing over-stresses at the pipe or lead to a critical decrease of the fatigue life.

Although it is not specified in most codes, standard industry practice has generally been not to permit cross flow vibrations while in-line vibration is accepted, provided that cumulative fatigue damage is acceptable during the design life time. The onset of cross-flow VIV criteria is often expressed as:

$$f_0 > \frac{U_{n,c}}{V_{R,onset} D} \gamma \qquad (2)$$

where the constraint is on the natural frequency f_0. $U_{n,c}$ is usually defined as a 100 year return period current velocity value and $V_{R,onset}$ is a typical onset value referred to a vibration amplitude of 0.1D. The safety factor γ is in industry practice often not explicit (i.e equal to 1.0) in eq. (2) but rather implicitly included by using conservative estimates of the current, frequency and natural frequency.

The current flow velocity is location specific and must be representative for the particular geographical area of the free span. Field measurements of acceptable quality and duration and a subsequent evaluation of current statistics using recognised statistical methods is usually required. A discussion may be found in Mathisen *et al*, 1997.

For pipelines on a very uneven seabed, the situation is rather complex with varying boundary conditions (proximity of neighbouring spans, support conditions etc.) combined with varying bending, tension and sagging effects. The variation of the natural frequency, f_0 of spans of nominally equal length can be substantial, Vitali *et al.*, 1993..

Standard industry practice may lead to design with very varying safety levels and it is evident that a rational design approach is tractable. This problem was initially considered in the Troll-Oil project, Mørk *et al*, 1995a where a 16" oil pipeline was designed to carry oil from the Troll West province (through a rocky uneven seabed with high density driven currents) to the Mongstad oil terminal within the Fensfiorden North of Bergen, Norway. The MULTISPAN project provides a generalisation and extension of the design recommendations developed in the Troll-Oil project.

The present paper focuses on the premises for a reliability based calibration of safety factors in a design criterion for onset of cross flow vibrations. A hydrodynamic on-set model and a probabilistic modelling for $V_{R,onset}$ and f_0 is presented.

MODEL FOR ONSET OF CROSS-FLOW VIV:

A semi-empirical relationship is proposed to predict the reduced velocity for onset of cross-flow VIV taking into account the effect of specific mass, stability parameter and gap ratio. The relationship is determined considering an equivalent dynamic system with concentrated mass (structural and added mass), spring stiffness and damping subjected to a sinusoidal lift force.

Assuming that the lift force is sinusoidal during a cycle, the amplitude of cross-flow VIV is given by the following relationship, see (Blevins, 1994):

$$\frac{A}{D} = \frac{0.5\rho U_n^2 C_L \sin(2\pi f_s t + \phi)}{(2\pi f_s)^2 m_e \sqrt{\left(1-(f_s/f_0)^2\right)^2 + (2\xi f_s/f_0)}} \qquad (3)$$

where (A/D) is the normalised cross-flow response, ρ is the fluid density, m_e is the effective mass per unit length of the pipe incl. structural mass, added mass and mass of internal fluid and ξ is the damping ratio. f_s is the vortex shedding frequency given by the Strouhal relationship

$$f_s = S_t \frac{U_n}{D} \qquad (4)$$

where S_t is the Strouhal number. The stability parameter K_s is defined as

$$K_s = \frac{4\pi m_e \xi}{\rho \cdot D^2} = \pi^2 \xi (\rho_s/\rho - C_m) \qquad (5)$$

where (ρ_s/ρ) is the specific mass (without added mass), ξ is the damping ratio and C_m is the added mass coefficient as a function of the gap ratio (e/D), see e.g. (DNVC, 1991).

Assuming $C_L \approx 0.3$ corresponding to the defined onset amplitude $(A/D) \approx 0.1$ seems reasonable according to Blevins, 1994. Further, introducing eq. (1), (4) and (5) into eq. (3) the reduced velocity at onset of cross-flow VIV can be expressed approximately as:

$$V_{R,onset} = \sqrt{\frac{\pi^3(\frac{\rho_s}{\rho}+C_m)}{1.5+S_t^2\left\{\pi^3(\frac{\rho_s}{\rho}+C_m)-1.5K_S^2\right\}}} \qquad (6)$$

Eq. (6) is illustrated in figure 1. It is an approximate solution but fits very well the exact solution of the reduced velocity from eq. (3).

The Strouhal number depends on Reynolds number, pipe surface roughness, free stream turbulence and gap ratio among others. In the present analysis it was assumed that the Strouhal number varies linearly with the gap ratio. An "optimal" Strouhal relationship providing the minimum variability in the model uncertainty is derived by considering a large set of both experimental data and full scale measurement with on-set values in the range from 2.0-5.5, see Vitali *et al, 1997* for details.

The following relationship for the Strouhal number

$$S_t = 0.27 - 0.03(\frac{e}{D}) \qquad (7)$$

was found to be optimal in full compliance with the findings in HSE, 1993. Note that the specific value C_L=0.3 is not critical since the model is calibrated to measured data.

For the Strouhal relationship in eq. (7) the model uncertainty related to the model for $V_{R,onset}$ is easily assessed, i.e., a model uncertainty with a mean value (bias) equal to 0.95, and a CoV in the range 10-15%. However, the uncertainty is likely to be on the high side due to a natural variability in the participating parameters, uncertainty in the laboratory or full-scale set-up, measurement uncertainty and uncertainty in the interpretation of the data which is implicitly included in the above uncertainty measures. The "true" variability is assessed using (subjective) engineering judgement in order to avoid unduly conservative estimates. A normal distribution with a bias equal to 0.95 and a CoV=10% appears to be reasonable.

The set of onset values are indicated in figure 2 along with a recommendation from the GUDESP project, Tura *et al*, 1994. Note that full-scale test exhibit lower onset values compared to laboratory conditions.

The onset model in figure 1 complies with the majority of reported physical dependencies reported in the literature. As a curiosity, the present study indicated that Reynolds number do not have a significant effect on the reduced velocity both for onset and for occurrence of maximum amplitude of VIV.

However, it should be noted that it is difficult in general to transfer the results from a test model to a prototype model. Further, most of the experimental results are obtained in the laboratory where the Reynolds number is always subcritical

($R_e < 2 \cdot 10^5$), while for submarine pipeline the Reynolds number is usually in the transitional or supercritical ($R_e > 3.5 \cdot 10^6$).

In spite of these short-comings the derived onset model is considered adequate for design purposes.

NATURAL FREQUENCY - UNCERTAINTY MODELLING

In design it is required that a refined non-linear static FE-analyses is conducted over an appropriate stretch of the pipeline, say, 2000 m. The as-laid, water-filled, hydrotest and operation condition is analysed in sequence, in each case obtaining an acceptable configuration in terms of stresses. The lowest natural frequency to be applied in eq. (2) is thus obtained from an eigenvalue analyses. The object here is to assess the uncertainty in the natural frequencies (obtained from a FE-model) to describe a real life scenario.

The probabilistic modelling of the cross-flow natural frequency applies a stochastic FE approach, i.e. a FE-model linked to a Monte-Carlo simulation facilitating an implicit handling of the probabilistic characteristics. FE-analyses for pipelines are very time-consuming and it often tractable to replace the direct link to the FE-model with an a-priori established response surface. The methodology comprises the following steps:

- A definition of condition and free span scenarios.
- An identification and probabilistic modelling of the most important basic variables from functional loads, pipeline and soil characteristics, seabed profile including subjective uncertainties.
- Definition of base case values and corresponding validity range/domain defined as lower and upper bounds.
- Establish a combination of input parameters adequately covering the required domain.
- For each combination calculate the natural frequencies using a state-of-practice FE-approach.
- Fit a response surface, e.g. a 2nd order polynomial in the space spanned by the variables, to the data base points.
- Link the response surface to PROBAN (DNVSesam, 1993a) and perform Monte-Carlo simulations to establish the statistics of the natural frequencies.

The data base is established using more than 200 non-linear FE-analyses conducted over an appropriate stretch of a typical pipeline ($\approx$ 1 km) for each sea bed category.

The obtained uncertainty measures in terms of CoV for the cross-flow natural frequency is compatible with the recommendations given in (Mørk *et al*, 1995a) for the TROLL-Oil project. The TROLL Oil project used a single span configuration in the probabilistic modelling of the natural frequency f_0. The results are presented in figure 3. The CoV varies from 9% to 24% dependent on the span length, seabed profile and soil conditions etc. but not significantly on the normalised effective axial force S_{eff}/P_E where P_E is the Euler buckling load. In a reliability based calibration study an average uncertainty is appropriate and LN(1.0;18%) seems reasonable.

Although not observable on the figure the three approaches do not provide conflicting results. Thus, the present analysis indicates that a multi-span scenarios with a sequence of free spans does not on average imply a larger uncertainty on the natural frequency estimation compared to a single span scenario.

RELIABILITY BASED CALIBRATION PROCEDURE

The safety philosophy adopted is based on *safety classes*, in compliance with DNV'96, see (DNV, 1996, or Collberg *et al*, 1997)

Structural reliability theory is applied as a formal link between the codes of practice and reliability requirements. A structural reliability analysis typically involves the following steps, see e.g. Madsen *et al*, 1986:

- Identify all significant failure modes
- Identify the relevant physical variables
- Define the limit state function for each failure mode
- Establish the appropriate joint distribution of the physical variables for load and capacity
- Estimate statistical uncertainties
- Introduce measures of the model uncertainties
- Calculate the failure probability
- Quantify acceptance criteria
- Evaluate results

A Load and Resistance Factored Design (LRFD) type format in compliance with industry practice is adopted. Following DNV CN30.6, 1992 the calibration procedure comprises the following items:

- Definition of the scope for the calibration.
- Establishment of an "easy to use and understand" design equation with a specification of characteristic values.
- Establish a set of representative design cases utilising the design equation with characteristic values and partial safety factors in compliance with the scope.
- Establish target reliability levels relevant for the various safety classes.
- Estimate the probability of failure for the design cases from a recognised reliability analysis and evaluate against target failure probabilities.
- Select appropriate partial safety factors guided by engineering judgement and industry practice.

Acceptable (target) failure probabilities depend in general on the consequence and the nature of failure, the hazard for human injury, the economic losses, the social inconvenience and the amount of expense and effort required to reduce the failure probability. The following annual (or the time period in the temporary phase) failure probabilities per pipeline versus safety classes are applied:

Safety Class	Low	Normal	High
P_f	10^{-2}-10^{-3}	10^{-3}-10^{-4}	10^{-4} -10^{-5}

Pipelines on uneven sea beds are generally confined to a geographic area and the number of independent *critical* failure scenarios expected to be encountered within such areas are usually limited. Only a few (order of 10^0 to 10^1) failure scenarios can be expected to be associated with a probability of failure of the same order as $P_{f,target}$ while the majority of scenarios are associated with a target probability of failure orders of magnitude lower than $P_{f,target}$. Further, a large subjective uncertainty is expected both for the load effects and the capacities. This among other aspects leads to moderate (even strong) correlation among the failure elements (free spans) and indicates that target reliability levels should refer

to each *single* failure scenario in compliance with traditionally performed *local* design checks.

CALIBRATION STUDY

Onset of cross-flow VIV is considered an ULS. The limit state function for may be given as

$$g(x) = f_0 - \frac{U_{n,e}}{V_R D} \tag{8}$$

where the random variables are contained in the vector x and $g(x)<0$ signifies failure. $U_{n,e}$ is the extreme current velocity normal to the pipe and V_R denote the random onset value for the reduced velocity.

Introducing the following normalised stochastic variables

$$X_f = \frac{f_0}{f_{0,c}} \qquad X_{V_R} = \frac{V_R}{V_{R,onset}} \qquad X_e = \frac{U_{n,e}}{U_{n,c}} \tag{9}$$

the limit state function may be rewritten

$$g(x) = X_f X_{V_R} \gamma - X_e \tag{10}$$

PROBABILISTIC MODELLING

The probabilistic modelling for $X_{VR} \in N(0.95;10\%)$ and $X_f \in N(0.95;10\%)$ are discussed above. The modelling for the normalised extreme current velocity X_e is given below.

$U_{n,c}$ is a characteristic current velocity value with a 10^{-2} exceedance probability in the extreme current distribution $F_E(u_{n,e})$ relevant to the considered period (the length of the temporary phase or 1 year for operation condition), i.e.,

$$F_E(U_{n,c}) = 1 - \frac{1}{100} \tag{11}$$

Current measurement (and industry practice) indicate that the local current maxima are Weibull distributed. For large time periods (i.e. large compared to the correlation length between individual local maxima) the extreme value distribution then asymptotically approaches a Gumbel distribution. A reasonable assumption is thus to assume that $F_E(.)$ is Gumbel distributed. This means that X_e may be written:

$$X_e \in G\left(E[X_e]; CoV[X_e]\right) \tag{12}$$

where $CoV[X_e]$ can be given approximately as

$$E[X_e] \approx \frac{1}{\left(1 + \pi CoV[X_e]\right)} \tag{13}$$

The modelling of the extreme current is then reduced to a definition of the variability in the extreme current distribution. $CoV[X_e]=CoV[U_{n,e}]= 0.05 - 0.25$ applied as design cases are clearly representative.

In design, the statistical uncertainty due to a limited number of measurements should be accounted for e.g. using a Bootstraping simulation technique, see e.g. Mørk *et al*, 1995b.

In the present calibration study the physical variability is represented by the Gumbel model whereas the statistical uncertainty is ignored. This is because it is considered tractable to work with an invariant safety factor and the effect of statistical uncertainty is approximately corrected for in the Design Guideline by imposing an adequate increase on the characteristic return period current value.

CALIBRATION RESULT

The result of the calibration study for the base case is presented in figure 4. The 5 lines correspond to the 5 design test cases for the annual extreme current distribution and the stars indicate proposed (base case) safety factors for annual probability of failure for safety class Low, Normal and High (i.e., $P_f \approx 10^{-3}$, 10^{-4} and 10^{-5}, respectively)

It is noted that a change in $CoV[X_e]$ only has a minor effect on the safety level. This is true even though the importance of the individual factors also changes and may be attributed to a very solid design format. (i.e. using a high characteristic current value defined with a 10^{-2} exceedence probability).

In figure 5 the design point values for the base case are presented as a function of safety class Low, Normal and High. The following may be noted:

- The design point for X_f is typically in between 0.6-0.7, i.e. close to two standard deviations below the mean.
- The design point for X_{VR} is close to 0.75. This means that a typical onset value between 3.3 and 4.5 applied in design will have corresponding most likely failure point values between 2.5 and 3.4. Cross flow VIV for reduced velocity values of that order have been observed in full scale test and are not considered unrealistic, see figure 2.
- The design point for X_e ranges from 0.9 to 1.25 depending on safety class and the variability in the extreme current velocity. A value larger than 1.0 indicates a value larger than the characteristic return current velocity.

All design points seem to be reasonable.

DESIGN GUIDELINE

The developed Design Guideline formally supports and complies with the DNV'96 Pipeline Rules for Submarine Pipeline Systems and is considered to be a supplement to relevant National Rules and Regulations.

Significant cross-flow vortex induced vibrations (VIV) defined as maximum oscillation amplitudes larger than 0.1D are not accepted. For the steady current case the cross-flow no-vibration criterion is given as:

$$f_{0,c} \geq \frac{U_{n,c}}{V_{R,onset} D} \gamma_T \Psi_D \Psi_R \Psi_u \tag{14}$$

$V_{R,onset}$ is a characteristic onset value given by eq. (6) using (7) for the Strouhal number and eq. (5) for the stability parameter. In eq. (5) the total damping ratio ζ, comprises:

- structural damping, ζ_{str} due to internal friction forces of the pipe material
- hydrodynamic damping, ζ_h accounting for the effects of the non-uniformity of the on-bottom current and the variation of the pipe-seabottom clearance along the pipe axis
- soil damping, ζ_{soil} due to pipe-soil interaction between suspended spans.

$U_{n,c}$ is a characteristic return period current component normal to the pipe defined as the value with a 10^{-2} exceedance probability in the extreme current distribution relevant for the

considered period. At operating conditions this corresponds to the 100 year return period current.

$f_{0,e}$ is a characteristic "best estimate" frequency obtained from a recognised and detailed FE-analysis of the considered pipeline stretch.

ψ_D is a transformation factor. Current induced VIV attain full amplitude after only a few vibrations and a time average period for the current in the order of 1 min is considered adequate. Thus, ψ_D is a transformation factor accounting for other time average periods, see Mathisen *et al*, 1997.

ψ_R is a reduction factor for the natural frequency, normally to be set to 1.0 and ψ_U is a factor accounting for the extreme current variability.

γ_T is a partial coefficient to be taken from the table below

Safety Class	Low *temporary*	Normal *in-service*	High *in-service*
γ_T	1.7	2.0	2.3

The onset of cross-flow vibrations may in general be defined as being in-between a SLS or ULS depending on the free span scenario and consequences of failure. Compared to a comprehensive fatigue analysis the onset criterion is considered to be conservative and may always be replaced by a recognised fatigue analysis

CONCLUSION

A reliability based calibration of safety factors for onset of cross-flow criteria is presented. The design criteria is presently implemented in a DNV Design Guideline. The work is presently being extended to cover full fatigue analyses and onset-criteria for combined wave and current induced loads related to unevenness induced and scour induced free spans. The final result will be implemented in a formal DNV Class Note 30.X on free spans in compliance with the new DNV'96 pipeline rules.

The MULTISPAN project will be presented in a dedicated session at the coming OMAE conference in April 13-17, 1997 in Yokohama, Japan.

ACKNOWLEDGEMENTS

The authors would like to thank Norsk Agip and Statoil for the permission to publish this paper and acknowledge the fruitful technical contribution from all project participants.

REFERENCES

Blevins R.D. "Flow-Induced Vibration", Krieger Publishing Company, Malabar, Florida, 1994.

Collberg L., Mørk K.J. & Bjørnsen "DNV'96, Limit State based Design Formats, A real Life Application." To be presented at OMAE'97, Yokahama, Japan, April 13-18, 1997

DNV'96 "Submarine Pipeline Rules - Draft for external hearing", Det Norske Veritas, Høvik. Norway, September 1996

DNVC CN30.5 "Environmental Conditions and Environmental Loads", Høvik, Norway, March 1991.

DNVC CN30.6 "Structural Reliability Analysis of Marine Structures", Høvik, Norway, July 1992.

DNVSesam "PROBAN Version 4: Theory Manual", Det Norske Veritas Research Report no. 93-2056, Høvik, Norway, 1993a.

HSE Report (1993): "Evaluation of Vortex Shedding Frequency and Dynamic Span Response", OTI 93614.

Madsen, H.O., Krenk, S. & Lind, N. "Methods of Structural Safety" Prentice Hall Inc., Englewood Cliffs, N.J., 1986.

Mathisen M., Hansen E.A., Andersen O.J. & Bruschi R. "The MULTISPAN Project: Near Seabed Flow in Macro-Roughness Areas." To be presented at OMAE'97, Yokahama, Japan, April 13-18, 1997

Moshagen H., Solemsli O., Verley R. & Bruschi R. "The Multispan Project: Project Background", To be presented at OMAE'97, Yokahama, Japan, April 13-18, 1997

Mørk K.J. Verley R. & Bruschi R. "Troll Oil Pipeline: Calibration of Safety Factors for Cross-flow Vibrations on Very Uneven Seabeds." OMAE'95 Conf. Volume V, pp. 439-447, Copenhagen, 1995a

Mørk K.J. & Bitner-Gregersen E. "Short Term Statistics of Extreme Load effects", Proc. of OMAE'95 Conf. Copenhagen, Denmark, Vol. II, ASME 1995, pp. 117-125, 1995b

Mørk K.J., Vitali L. & Verley R. "The MULTISPAN project: Design Guideline for Free Spanning Pipelines", To be presented at OMAE'97, Yokahama, Japan, April 13-18, 1997

Tura F., Dumitrescu A., Bryndum M.B. & Smeed P.F. "Guidelines for Free Spanning Pipelines: The GUDESP Project." 1994 OMAE, Volume 5, pp 247-256, Houston, 1994.

Vandiver J.K. "Dimensionless Parameters Important ot the prediction of Vortex-Induced Vibration of Long Flexible Cylinders in Ocean Currents". Journal of Fluid and Structures, Vol.7, pp.423-455, 1993.

Vitali L., Marchesani F., Curti G. & Bruschi R. "Dynamic Excitation of Offshore Pipelines resting on very Uneven Seabeds, EURODYN 93, Trondheim, Norway, June 1993.

Vitali L., Verley R., Mørk K.J., & Malacari L.E. "The MULTISPAN Project: Response Models for Vortex-Induced Vibrations of Submarine Pipelines" To be presented at OMAE'97, Yokahama, Japan, April 13-18, 1997

Figure 1: Onset value for Cross-Flow VIV

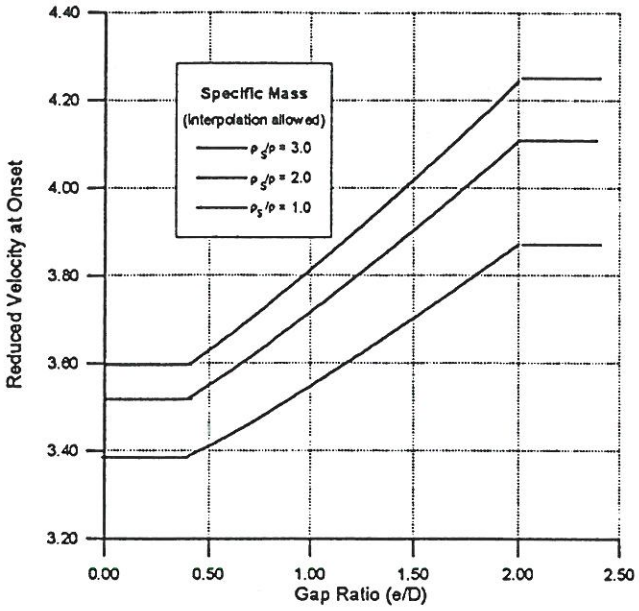

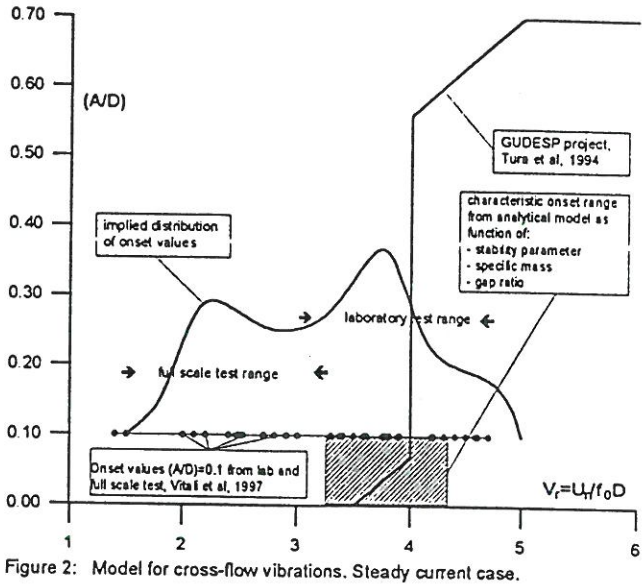

Figure 2: Model for cross-flow vibrations. Steady current case.

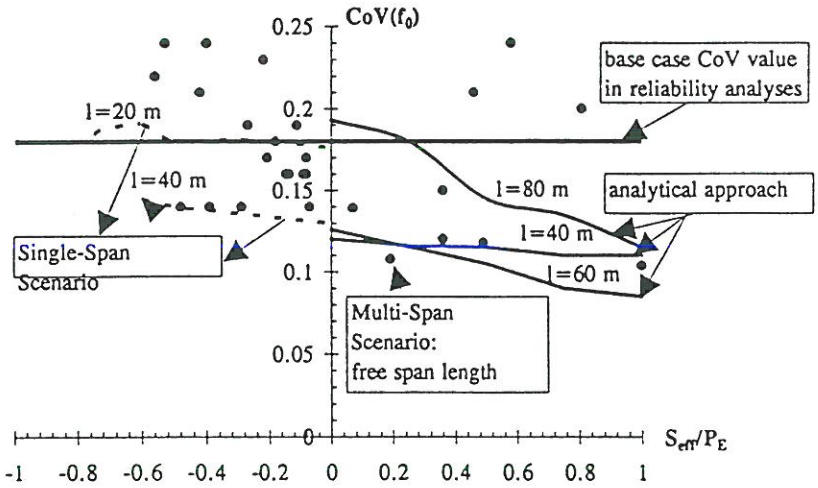

Figure 3: Assessment of model uncertainty (CoV) for natural frequency.

Figure 4 Onset Criteria for Cross-Flow VIV. Calibration Study for Base Case

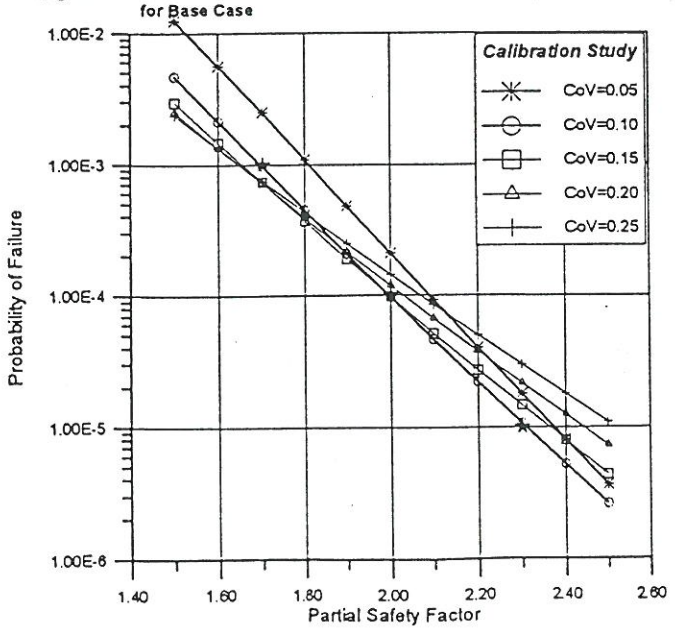

Figure 5: Onset Criteria for Cross-Flow VIV. Design Point Values for Base Case

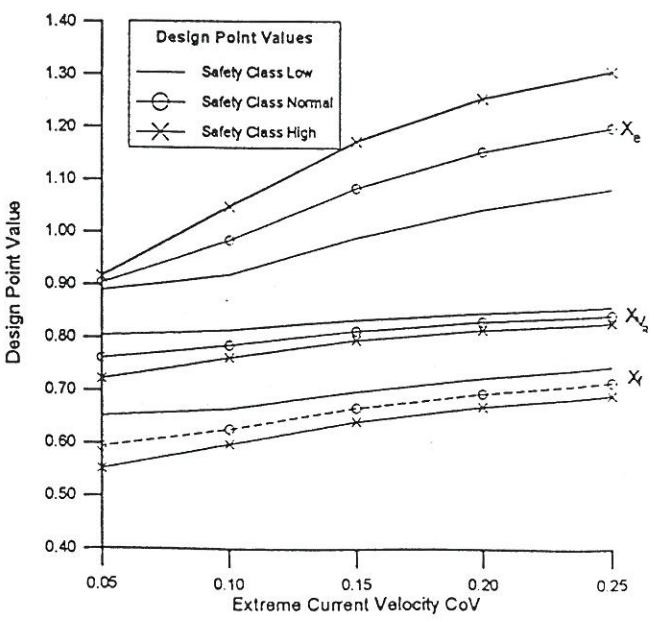

Mechanical energy flow in vibrating structures

B L Josefson, M A Wilson and M Kilian
Division of Solid Mechanics
Chalmers University of Technology
S-412 96 Göteborg, Sweden

Noise and vibration control is a matter of increasing interest. The demand for noise reduction in vehicles like cars, trucks, street cars and aeroplanes will most likely increase in the near future. Structure borne sound constitutes a special problem. Since it is difficult to reduce in an existing structure it is desirable to obtain a qualitative knowledge of dominant paths of energy transfer in the structure already in the design process. The mechanical energy flow is mathematically described with the (instaneous) mechanical intensity vector $q_i = -\sigma_{ij} v_j$. The mechanical intensity vector field contains information about the direction and magnitude of the rate of energy flow (power flow) per unit cross-sectional area and may be displayed as an image of the energy flow field. The use of the mechanical intensity may then enhance the understanding of structure borne sound.

At the Divison of Solid Mechanics at Chalmers we have been working with the mechanical intensity concept for four years in a research project sponsored by the Swedish Research Council for Engineering Sciences (TFR). In the present paper we will present some results from this ongoing project. Our approach is based on the use of the FE-method, which for low frequencies is a powerful tool which provides calculated displacement- and velocity fields and eigenmodes with sufficient accuracy. The approximation normally made in a dynamic FE-analysis to discretize the inertia forces and to use polynomial shape functions for the assumed displacement field will be reasonably good. In these FE-analyses we employ the commercial FE-code SOLVIA, where pertinent expressions for the mechanical intensity has been implemented, see Alfredsson (1993) and Alfredsson, Josefson and Wilson (1996).

For higher frequencies use of the displacement based FE-method will demand an excessively fine mesh in order to resolve, spatially, high local eigenmodes of the structure. Structure borne sound problems in thin-walled steel or aluminim structures may be important at frequencies of about 200-1000 Hz. In this range the modal density is still too low to apply energy based methods like statistical energy analysis (SEA). One alternative approach would then be to extend the applicability of an ordinary FE-analysis by employing dynamic substructuring. We have studied two different reduction methods, the approximate Guyan reduction scheme and the exact dynamic substructuring approach, see Wilson and Josefson (1996), with regard to both accuracy in the computed results and the demand for CPU capacity and memory requirement.

Finally, we present some results for a technical application, the transmission of energy in a truck frame, from the engine (where the truck is excited) to the truck cabin. In particular, the influence of the properties and shape of the cabin to truck frame connection on the total energy transmitted to the truck cabin is studied.

Basic equations

Consider an elastic solid subjected to time-varying external loads. A linear viscoelastic material model of Kelvin type is used to describe internal hysteretic material damping quantified with a loss factor η. The energy continuity equation will read

$$\frac{dW}{dt} + \Pi_0 = L_0 - q_{i,i} \tag{1}$$

Equation (1) expresses a mechanical power balance for an infinitesimal volume. The left hand side contains the power dW/dt being stored, that is the the change in total reversible energy (sum of strain and kinetic energies) and the power Π_0 being dissipated inside the volume. The right hand side contains the power L_0 supplied per unit volume by external body forces and the power $-q_{i,i}$ flowing into the infinitesimal volume through its boundaries.

For the case of stationary harmonic vibration at a given frequency ω, the complex mechanical intensity $\underline{c}_i$ is introduced,

$$\underline{c}_i = -\frac{1}{2}\underline{\sigma}^*_{ij}\underline{v}_j = a_i + ir_i \tag{2}$$

The real part, a_i, of the complex mechanical intensity is termed the active mechanical intensity and corresponds to the net (average) energy flow rate per unit cross-sectional area. The imaginary part, r_i, is called the reactive mechanical intensity. Introducing the complex power supplied per unit volume by body forces, $\underline{S}_0 = P_0 + iQ_0$, the continuity equations for the active and reactive and reactive intensities may be written,

$$a_{i,i} = P_0 - \Pi_0 \qquad r_{i,i} = Q_0 - 2\omega(\overline{U}_0 - \overline{T}_0) \tag{3a,b}$$

Here $\overline{\Pi}_0$, $\overline{U}_0$ and $\overline{T}_0$ are the time-averaged power dissipated per unit volume, the elastic strain energy density and the kinetic energy density, respectively.

For the complete structure one finds that balances prevail between total supplied active power P and the dissipated power Π on one hand, and the total supplied reactive power Q and the total strain and kinetic energies U and T on the other hand. Hence the total supplied active power equals the time-average of the total power dissipated in the structure. The reactive power is related to the difference between the time-averages of the strain and kinetic energies.

Local energy flow in built-up cylindrical shell structure

Below we show some calculated results for a built-up shell structure, see Figure 1. A point mass is placed on a horizontal flexible (upper) plate, which in turn, is connected to a larger horizontal (lower) plate through four vertical springs. This lower plate is connected to the inner side of a flexible circular cylinder (also) through four vertical springs. The cylinder has free ends. The structure consists of four-node shell elements employing consistent mass matrices, and some spring elements resulting in totally 9200 complex valued dofs. The simplified structure in this example should represent a typical submarine application and it has been studied previously in the literature. The wall thicknesses are taken as 5 - 10 mm. The length of the cylinder is 1.4 m and the radius of the cylinder is 0.35 m. Note that the upper plate is placed eccentrically on the lower plate in both horizontal directions. The shell structure is proportionally damped with the loss factor taken as η = 0.01. Figure 2 shows the

calculated vector field, a_i, in the upper and lower horizontal plates at one resonance frequency, $f = 45$ Hz. It is seen that the energy flow through the four springs to the lower plate and to the cylinder is not uniform, on the contrary most of the energy is transmitted through one particular spring.

Figure 3 shows the corresponding result for the calculated vector field, a_i, in the upper and lower horizontal plates when dynamic substructuring has been employed, that is the cylinder is condensed using Guyan reduction. Hence, the structure stiffness and mass matrices for the cylinder are reduced using static condensation, that is neglecting inertia forces on slave degrees of freedom when establishing a relation between master dof:s and slave dof:s. The four connection points for the vertical springs are chosen as points with master degrees of freedom. Note though, that in Fig. 3 the cylinder has shear diaphragm boundary conditions at the cylinder ends. It is seen that the active mechanical intensity field can be modelled by use of dynamic substructuring.

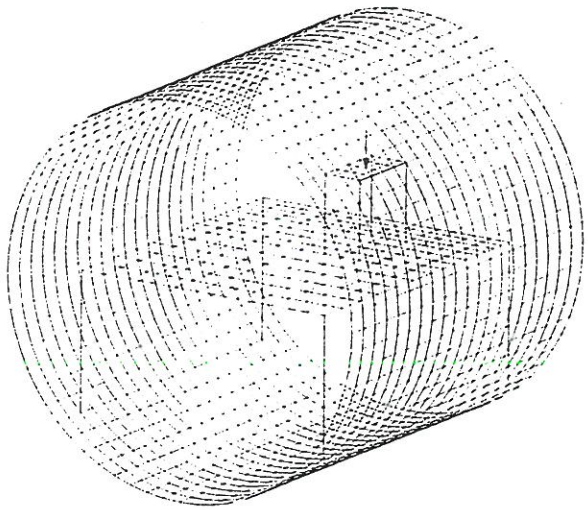

Fig. 1. Geometry for built-up shell structure.

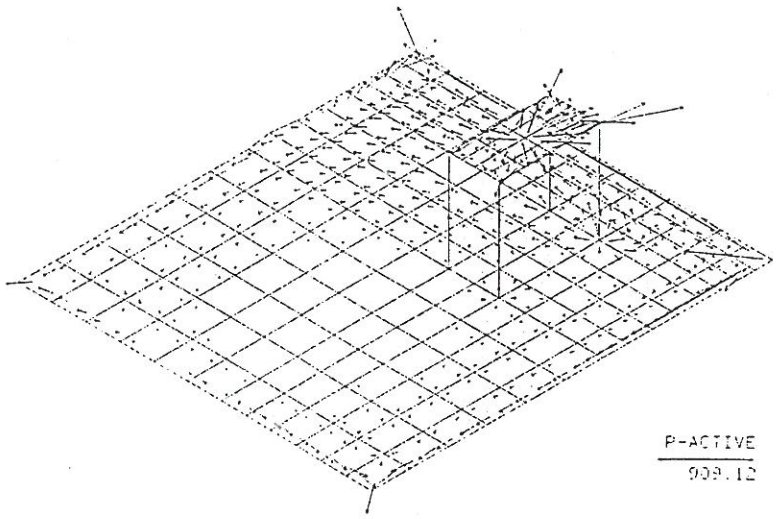

Fig. 2. Calculated active part of mechanical intensity vector field a_i in upper and lower plates at frequency $f = 45$ Hz.

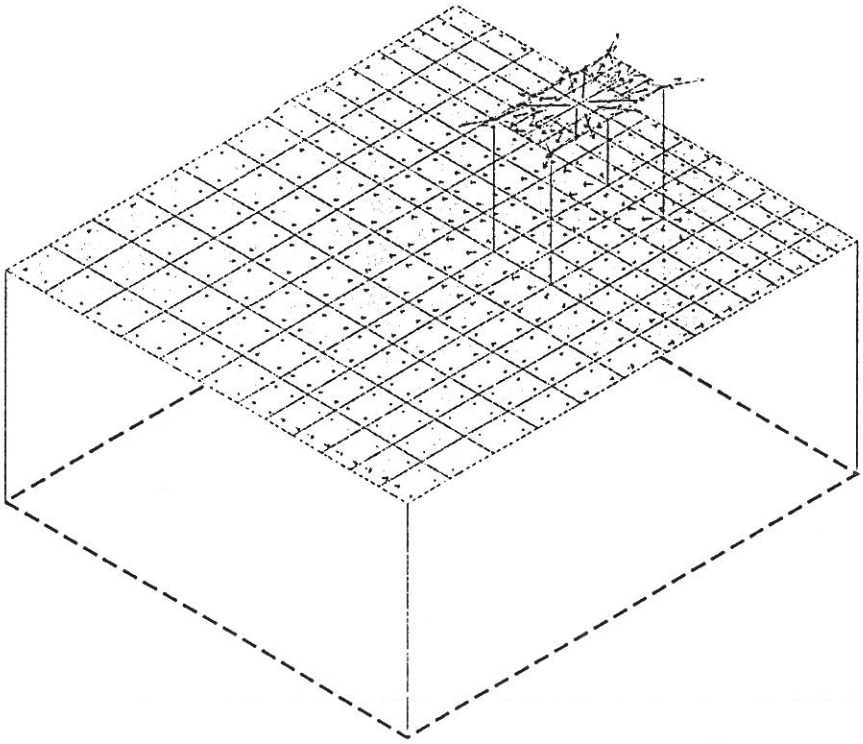

Fig. 3. Calculated active part of mechanical intensity vector field a_i in upper and lower plates at frequency $f = 45$ Hz for the case when cylinder is modelled by use of Guyan reduction.

References

Wilson, M.A., and Josefson, B.L., 1996, Mechanical intensity fields in reduced structures, *Proceedings of the 37th AIAA / ASME / ASCE / AHS / ASC Structures, Structural Dynamics and Materials Conference* in Salt Lake City, UT, USA, pp. 1585-1593.

Alfredsson, K.S., Josefson, B.L., and Wilson, M.A., 1996, Use of the energy flow concept in vibration design, *AIAA Journal,* Vol. 34, pp. 1250-1255.

Alfredsson, K.S., 1993, Active and reactive structural energy flow, to appear in *ASME Journal of Vibration and Acoustics,* in press.

ELEMENTS OF AERODYNAMIC FLUTTER CONTROL

Allan Larsen, COWI Consulting Engineers and Planners
15 Parallelvej, DK-2800 Lyngby, Denmark

1 Introduction

The design of very long span cable supported bridges requires special attention to the problem of aeroelastic stability or flutter. For long span suspension bridges with "semi-streamlined" decks binary (or two degree-of-freedom) flutter is of paramount importance and becomes a governing factor in the design of girder, towers and main cables. Past efforts to cope with the flutter problem have involved increased torsional stiffness of the girder and redistribution of the inertia but this method often leads to uneconomical designs for spans longer than, say, 2000 m.

The twin-deck concept [1] as proposed in a study of super long span bridges studied for the Straits of Gibraltar presents an attractive solution to the flutter problem associated with very long span bridges. The twin-deck concept involves considerable lateral separation of the two carriage ways, leaving a huge air gap or "slot" between them. In an inclined wind the lift and moment distribution on the twin-deck becomes almost identical to the lift and moment distribution on a conventional box cross section, but the pitch velocity becomes considerably larger leading to strong aerodynamic damping in torsion. By varying the width of the deck slot between the carriage ways during design the bridge engineer is in a position to exert *passive flutter control* on the bridge structure in question. The twin-deck layout may thus be tailored to meet certain requirements to the critical wind speed for onset of flutter.

An alternative approach to passive increase of aerodynamic damping is to actively introduce external forces which will counteract the destabilising aerodynamic loads developing on the deck section. This method referred to as *active flutter control* have been used for control of model response in transonic wind tunnel flutter testing of aircraft lifting surfaces and for expansion of the flight envelope of fighter aircraft. Active flutter control of aircraft structures often rely on prescribed movement of existing ailerons or flaps for generation of the necessary control forces.

The present paper examines the basic concepts of active flutter control and discusses use of trailing edge flaps for generation of aerodynamic control forces. Finally aerodynamic flutter control of a practical bridge girder section is discussed in view of aerodynamic simulations based on the discrete vortex method.

2 Mechanism of Binary Flutter and Active Flutter Control

Binary flutter is driven by aerodynamic forces induced by oscillatory torsion and bending motion of a given cross section. The motion in torsion (deck twist) is found to lag the vertical (bending) motion by a certain phase angle governed mainly by structural mass and mass moment of inertia. The phase lag between torsion and vertical bending will cause aerodynamic lift forces L to act in the direction of vertical motion h ($L \cdot h > 0$) for longer periods of time than it will act opposite to the direction of vertical motion ($L \cdot h < 0$). Thus energy is extracted from the wind and stored in the mechanical motion during each circle. Energy can only be dissipated by structural damping and if the energy extracted from the wind exceeds the dissipation in the structure flutter movements will grow during each cycle. This process is illustrated in figure 1. The phase angle in figure 1 is taken to be 45 deg. for illustrative purposes but is normally found to vary between 15 deg. and 30 deg. for typical box girder bridge sections.

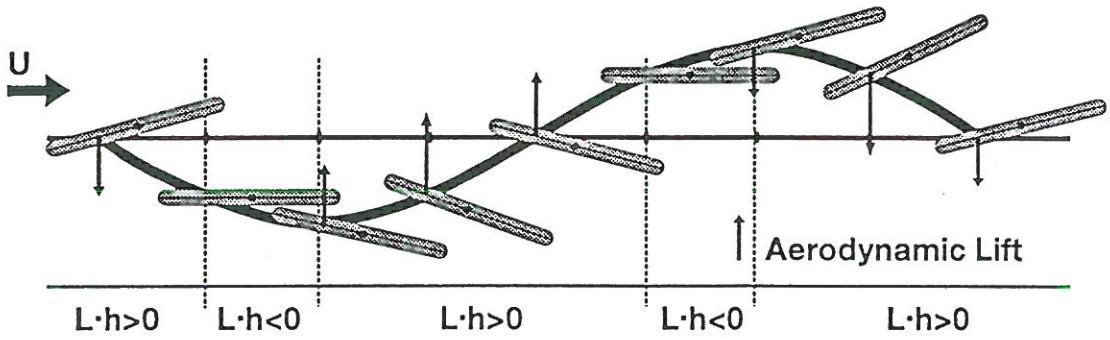

Figure .1 Motion and vertical aerodynamic lift during one circle of binary flutter.

The observation that aerodynamic lift forces are acting in the direction of vertical motion for the majority of a flutter cycle may be exploited in a strategy for flutter control. If a method is devised that allows additional vertical section forces to be introduced in phase or out of phase with the vertical motion as demonstrated in figure 2, flutter may be controlled.

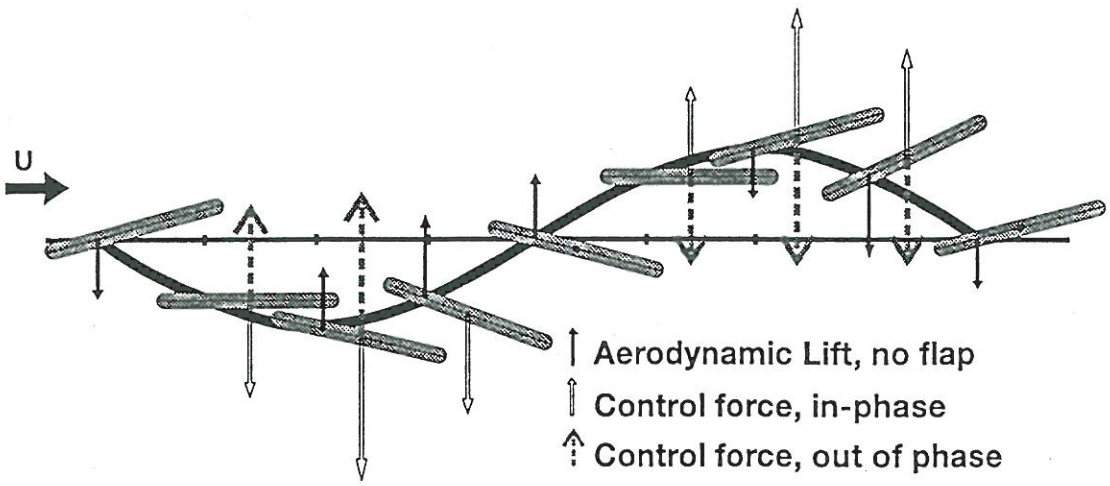

Figure 2. Introduction of vertical control forces in phase (outline) and out of phase (dashed) with the vertical section motion.

Control forces introduced in phase with the vertical motion tends to cancel the aerodynamic lift and should thus increase the critical wind speed for onset of flutter. Control forces introduced in opposite phase of the vertical motion tends to enforce the aerodynamic lift resulting in a decrease of the critical wind speed for onset of flutter.

As an example a 37.5 m wide generic box section for a 2500 m span suspension bridge is considered. Using conventional flat plate flutter theory [2] yields a critical wind speed U_c = 37 m/s which is obviously to low considering standard requirements of 60 m/s. Introducing a vertical control force equal to 0.25‰ of the dynamic vertical section force (= $(2\pi \cdot h)^2$m, m = section mass / unit length) in phase with the vertical motion yields a critical wind speed U_c = 43 m/s. If the phase of the control force is shifted 180 deg. the critical wind speed is lowered to U_c = 28.5 m/s. This control strategy is sometimes adopted for aircraft wind tunnel flutter tests under transsonic or supersonic conditions during which the wind tunnel operator is unable to interfere manually for prevention of model destruction by violent motions. In such cases the control forces will usually be provided by electrodynamic shakers controlled by a servo-loop involving optical displacement transducers or accelerometers for detection of structural motions.

3 Aerodynamic Flutter Control

Active flutter control by means of externally supplied control forces is clearly possible for wind tunnel testing but becomes impractical for large bridge structures and virtually impossible for flying aircraft. For aircraft it becomes interesting to generate the control forces aerodynamically by means of moveable ailerons. Aerodynamic flutter control is investigated in wind tunnel studies for fighter aircraft [3] and is found to be practical. Application of the similar principles for control of bridge deck flutter have been patented by COWI [4] and practical implementation is currently under evaluation. The basic elements of aerodynamic flutter control is understood from the lift force diagram, figure 3

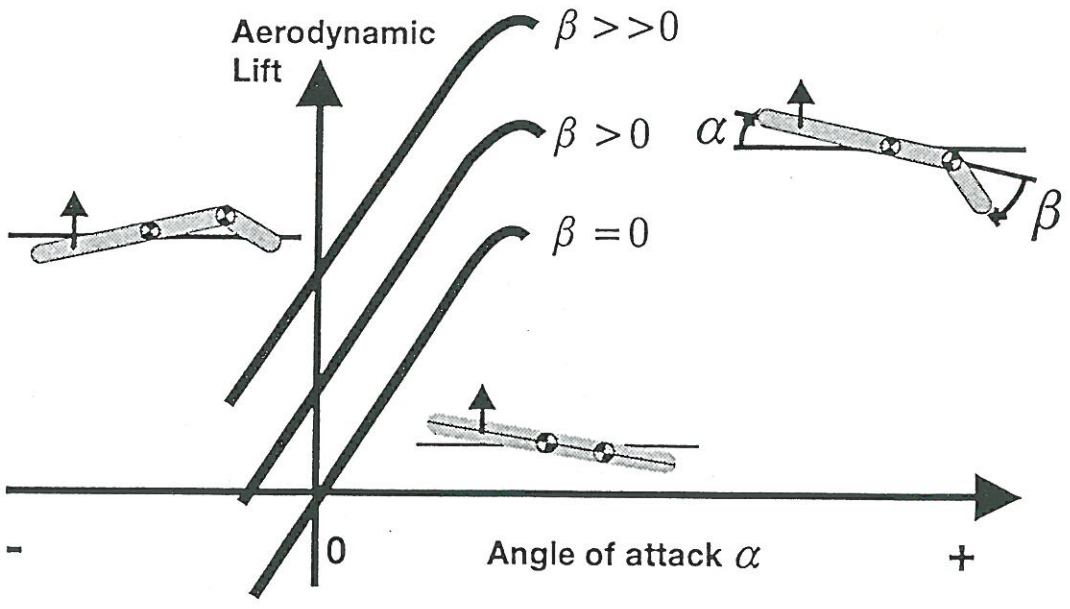

Figure 3. Aerodynamic lift as function of angle of attack for a section fitted with trailing edge flap.

For the case of zero flap angle, $\beta = 0$, the aerodynamic lift is proportional to the angle of attack at angles below stall. The proportionality factor, the lift slope, is equal to 2π for a thin airfoil section and somewhat less, typically ranging between 5.0 and 6.0, for practical "semi-streamlined" bridge girder cross sections. For flap angles $\beta>0$ the lift curve is shifted along the lift axis leading to negative angles of zero lift. At high flap angles $\beta>>0$ it becomes possible to maintain positive lift even for pronounced negative angles of attack. A similar effect to the in-phase control force depicted in fig. 2 may be obtained if the trailing edge flap is operated out of phase relative to the torsion motion. In theory it is even possible to reverse the overall aerodynamic lift force as shown in figure 4.

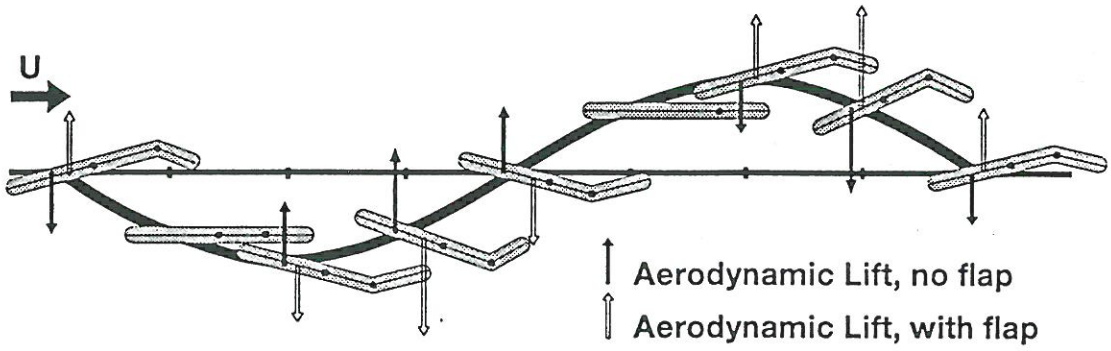

Figure 4. Effect of moveable trailing edge flap on the aerodynamic lift force generated on a cross section. Note that the aerodynamic lift may be reversed due to the presence of the flap.

4 Aerodynamic Flutter Control of Practical Bridge Girder Cross Sections

The development of aerodynamic lift force for cross sections with trailing edge flaps shown in figure 3 is only strictly valid for thin airfoil type cross sections with attached flow. Practical bridge girder cross sections are relatively thick and bluff thus the wind flow around a typical "semi-streamlined" cross section is characterised by large regions of separated flow and a wide vortical wake. The effect of trailing and leading edge flaps on practical cross sections are currently under investigation by COWI using a computerised discrete vortex method implemented in the code DVMFLOW. Flutter predictions based on flutter coefficients (aerodynamic derivatives) calculated by means of DVMFLOW for the East Bridge and the Gibraltar twin-deck cross sections have demonstrated good to excellent agreement with wind tunnel test results [5].

The generic cross section chosen for investigation of the aerodynamic efficiency of a trailing edge flap for aerodynamic flutter control is shown in figure 5. Mass and dynamic properties of the cross section are characteristic of a 2500 m suspension bridge. The central part of the section is 25 m wide and 3.75 m deep rectangular box carrying the roadway hanger sockets and mechanical equipment for moving the triangular edge flaps. The edge flaps are designed to rotate about horizontal hinges at amplitudes of ±30 deg. For the part of the investigation reported herein only the trailing edge flap will be active.

The present cross section layout is very similar to the design planned to be investigated in wind tunnel tests by Aalborg University

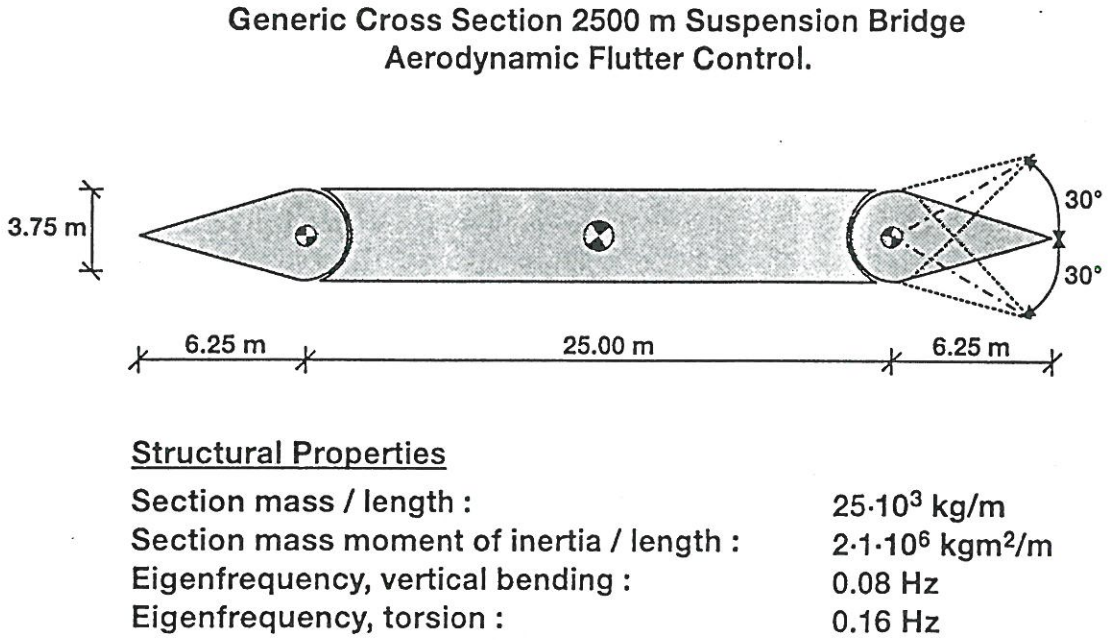

Figure 5. Cross section used in numerical investigation of the efficiency of a trailing edge flap for aerodynamic flutter control.

Three trailing edge flap configurations were investigated:

- Stationary flap. No movement of the trailing edge flap structure
- Phase $\varphi = 1/2\pi$. The trailing edge flap rotated about the hinge at the same frequency as the main box but with a phase shift of 90 deg. Flap amplitude: $\beta = 30$ deg.
- Phase $\varphi = 5/6\pi$. The trailing edge flap rotated about the hinge at the same frequency as the main box but with a phase shift of 150 deg. Flap amplitude: $\beta = 30$ deg.

The numerical flutter investigation proceeded as described in [6]. Aerodynamic derivatives were calculated for non-dimensional wind speeds U/fB = 6, 8, 10 and 12 by means of the forced motion technique. The critical wind speed for onset of flutter was obtained coupling of structural properties and the aerodynamic derivatives using the AMC method. Critical wind speeds U_c for the three flap configurations are obtained from the U-g diagram, figure 6 as the abscissa to intersection point between the calculated virtual aerodynamic damping (U-g) curves and a horizontal line (g = 0.01) corresponding to the anticipated mechanical damping level of the bridge structure. Please note that the Theodorsen damping used in figure 6 by definition is equal to twice the damping relative to critical ($g = 2\cdot\zeta$) or the decrement damping divided by π.

Critical wind speeds are obtained from figure 6 and presented in table 1 below:

Flap configuration	Critical wind speed U_c (m/s)
Stationary flap	37
Flap phase $\varphi = 1/2\pi$ (90 deg.)	41
Flap phase $\varphi = 5/6\pi$ (150 deg.)	31

Table 1 Critical wind speeds for onset of binary flutter for flap configurations investigated in the present study.

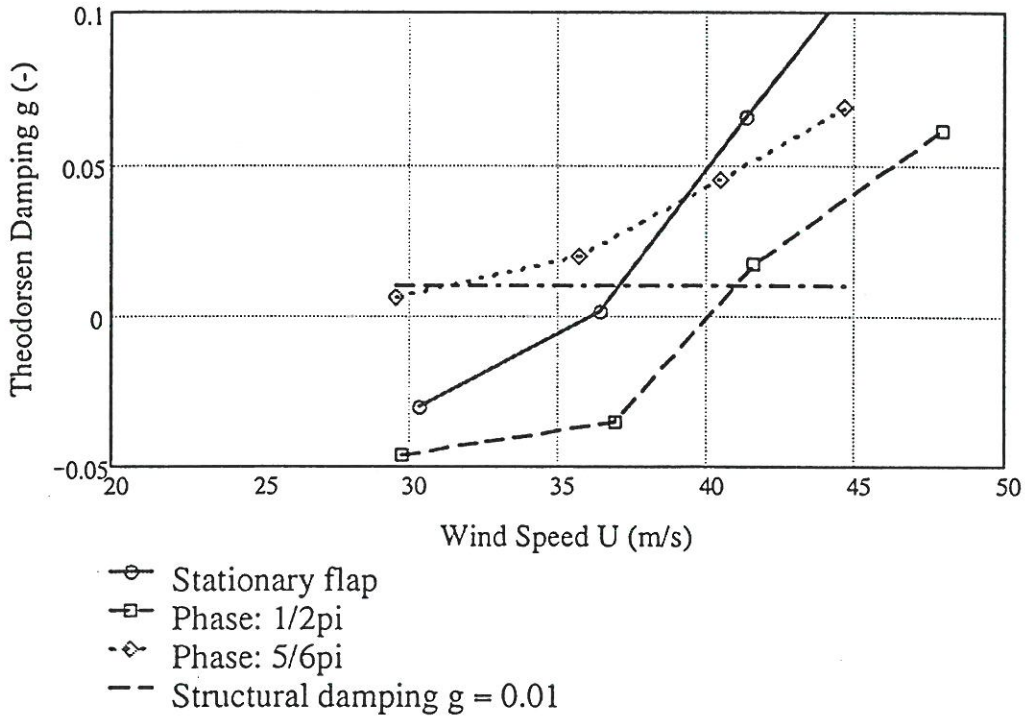

Figure 6. U-g diagram based on aerodynamic derivatives obtained from DVMFLOW simulations of forced twist and bending oscillations.

Two observations may be made from figure 6 and the summary table above:

- DVMFLOW analysis of the onset of flutter for the section with stationary trailing edge flap yields U_c = 37 m/s which is identical to the critical wind speed obtained from standard "flat plate" analysis
- A controllable trailing edge flap can be used for control of the critical wind speed for onset of flutter, but the choice of phase angle between the twisting motion of the main box structure and the is crucial to the effectiveness of the flap.

Plots of the flow field around the section with stationary flap and with the flap operating at amplitude β = 30 deg. and a phase angle φ = 90 deg. relative to torsion of the main box are shown in figure 7 and 8 below.

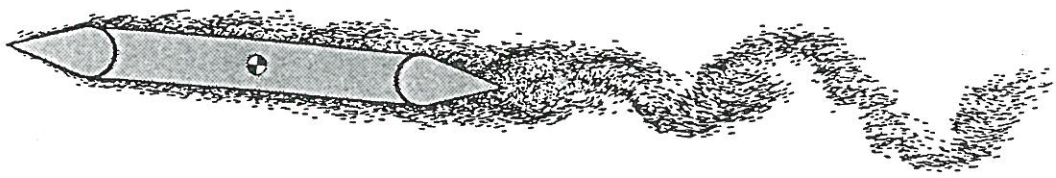

Figure 7. Flow around section with stationary flap at non-dimensional wind speed U/fB = 8. Maximum rotation of main box.

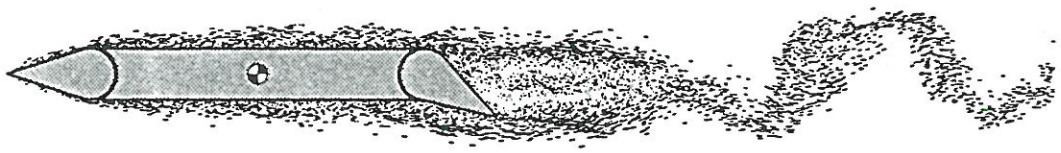

Figure 8. Flow around section with moveable flap at non-dimensional wind speed U/fB = and flap phase shift = 90 deg. Maximum flap deflection, main box horizontal.

The flow depicted in figure 8 displays a large separation zone at the suction side and in the wake of the deflected flap. This separation is likely to be responsible for the rather poor efficiency of the trailing edge flap operating at a phase angle of 90 deg.

5 Conclusion

The results of the present numerical study indicates that is indeed possible to influence the critical wind speed for onset of binary flutter by means of controllable edge flaps. The desired effect, i.e. an increase of the critical wind speed from 37 m/s to 41 m/s is however less than desired.

The numerical studies are continued by exploring more phase angles and the combined effect of moveable leading edge and trailing edge flaps.

6 References

1. Larsen, A., Ostenfeld, K.H. and Astiz, M.: "Aeroelastic stability study for the Gibraltar Bridge feasibility study". In IV International Colloquium on the Gibraltar Fixed Link, Seville 1995.

2. Frandsen, A.G.: "Wind stability of suspension bridges. Application of the theory of thin airfoils", Publication IX, Bygningsstatiske Meddelelser Vol. 41, 1970.

3. Gravelle, A.: "Active flutter control in transonic conditions". In Structural Control, H.H.E. Leipholz (ed.), IUTAM, 1980.

4. Ostenfeld, K.H.: European Patent EP 0 627 031 B 1, "A system and method for counteracting wind induced oscillations in a bridge girder."

5. Larsen, A. and Walther J.H.: "A new computational method for assessment of the aeroelastic stability of long span bridges", 15th IABSE Congress, Copenhagen 1996.

6. Larsen, A. and Walther J.H.: "Aeroelastic analysis of bridge girder sections based on discrete vortex simulations", 2nd International Symposium on Computational Wind Engineering, Colorado State University, Colorado, 1996.

Bearing Capacity of Foundations subjected to Impact Loads

Department of Civil Engineering, Aalborg University, Denmark

Lars Bo Ibsen & Kim Parsberg Jakobsen

1 Introduction

In the design process for foundations, the bearing capacity calculations are normally restricted to monotonic loads. Even in cases where the impact load is of significance the dynamic aspects are neglected by use of a traditional deterministic ultimate limit state analysis. Nevertheless it is common knowledge that the soil under such circumstances normally will produce a reaction, which exceed the static capacity. A new model, which takes these significant properties into account is presented.

To utilize this dynamic property it is sometimes assumed that the foundation is resting on an elastic halfspace, meaning a homogeneous, isotropic, elastic semi-infinite body of soil (Das 1983 and Kortenhaus et al. 1993). Such an assumption seems reasonable in the serviceability limit state where only small strains occur and the methods might under these conditions produce reliable results.

Generally the impact load under consideration is of such a magnitude that the monotonic design load or even the static bearing capacity might be exceeded. Due to this fact and a pronounced plastic behaviour of the soil, it is clear that the mentioned models can not describe the motion of the foundation near failure. The establishment of an alternative model is therefore needed.

The above mentioned facts lead to the first alternative model based on perfect plasticity, which implies a qualitative evaluation of different failure modes. Since the problems usually appears in design situations involving structures of a great size (vertical breakwaters, gravitational platforms and bridge piers) the problem are reduced to include plane failure modes. Theoretically these modes must be statically as well as the kinematically admissible, but since it is difficult to fulfil both conditions it is chosen to use the upper bound theory, which means that the failure modes are at least presumed to be kinematic admissible. The dynamic aspects are introduced as the geometrical change of the rupture figure, the inertia of the accelerated mass and an eventual increase in the soil strength. These constituent parts collectively form the equation of motion, for which reason the dynamic bearing capacity must be determined at an admissible irreversible displacement.

2 Description of the Dynamic Model

In a traditional upper bound solution the bearing capacity emanate from the strength parametres, the specific gravity of the soil and any overburden pressure. However the influence from the different elements will depend on whether drained or undrained conditions are considered. It is in the following chosen only to consider undrained conditions, but the approach to drained conditions is straight forward.

Since the model is based on perfect plasticity the foundation will stay at rest until the static load carrying capacity is exceeded. An exceedance will then cause the solid bodies of soil and the superstructure to move along the failure lines prescribed by the displacement diagram, and since the material is plastic any displacement is permanent and the movements will stop whenever the velocity of the bodies equals zero. Subsequently the dynamic elements are introduced by means of the acceleration in the displacement diagram, for which reason it is of great importance that the applied failure mode produces reliable results. Thus the dynamic load carrying capacity will depend on the choosen failure mode and hence it is found convenient to express the dynamic capacity by an overloading factor which solely describes the permissible overload in proportion to the static load carrying capacity of the current failure mode.

A more detailed description of the dynamic elements is given below.

2.1 The Dynamic Strength of Soil

As mentioned before it is found that the soil due to dynamic loading might produce an additional strength. This phenomenon has especially been studied by undrained triaxial compression tests with varying strain rates. The tests have been performed on cohesive as well as non-cohesive soils with quit different results.

Cohesive soils are found to exhibit a change in undrained shear strength (c_u) as a function of the strain rate ($\dot{\varepsilon}$) during loading. This partially viscous behavior is illustrated by Bjerrum 1971 and by Kulhawy et al. 1990. Thus the relationsship between undrained shear strength of clay and the strain rate may be described as.

$$c_{ud} = c_u + \Delta c_u^d \log \dot{\varepsilon} \approx c_u + \Delta c_u^d \dot{\varepsilon} \qquad (1)$$

The latter part is convenient, but only valid for small variations in the strain rate.

A similar relationsship is not observed for sand, where the strength seems independent of the strain rate. However, it is found that the failure under undrained conditions is controlled by the same limiting conditions as found for drained failure (Ibsen 1995). This means that the common stress path that in the literature often is considered to be the undrained failure envelope does not present any failure state in the sand; a shear strength corresponding to the drained strength must be used.

2.2 Forces of Inertia

In order to calculate the dynamic load carrying capacity it is necessary to include the inertia of the soil and the superstructure. The mass of the superstructure is often considerable and can therefore not be neglected.

By presuming that the soil and the structure moves as rigid bodies the displacement diagram can be used for the determination of the systems inertia. Thus the displacement diagram prescribes the direction and the magnitude of the displacement and the equivalent acceleration of the bodies.

2.3 Geometrical Changes

The development of failure in the foundations might in general cause significance damage to the superstructure. However, it is found that the development of such failure often results in geometrical changes which improve the overall stability. Whenever the bearing capacity is exceeded, soil will be pushed up by the side of the foundation and act as an overburden pressure. The upheaval in front of the foundation results in an increase in the stabilizing earth pressure, whereas the subsidence behind the foundation reduces the propulsive earth pressure. Coincident with the change in earth pressure, the displacement of the rigid bodies results in a shortening of the failure lines and the bearing capacity is hereby reduced. Totally the geometrical changes will either lead to a strengthening of the foundation or precipitate failure, for which reason the effect must be evaluated in each case.

2.4 Simplified Representation of the Load

In this context the load is presumed to consist in an external action, which within a short time exceeds the static load carrying capacity. Since various elements in general are important for the appearance of the actual load history the history are often jagged and inapplicable for mathematical formulations, for this reason a simplified representation of the load is necessary. The choice of such a simplified load substitution is found to be of great significance for the irreversible displacement and hereby for the bearing capacity. It is however desirable to attain a formulation of the impact load which in a simple way takes the significant properties into account.

To illustrate the characteristics of an impact load, a typical record of a maximum horizontal wave load is shown in Figure 2.1.
For this type of loads some interesting properties can be observed (Oumeraci et al. 1992).

- The impact has a magnitude (F_{dyn}) that is about twice the quasi-static load (F_{static}).
- The quasi-static load is only exceeded for a short period of time.

For the description of this phenomenon Oumeraci et al. 1992 have proposed a so-called

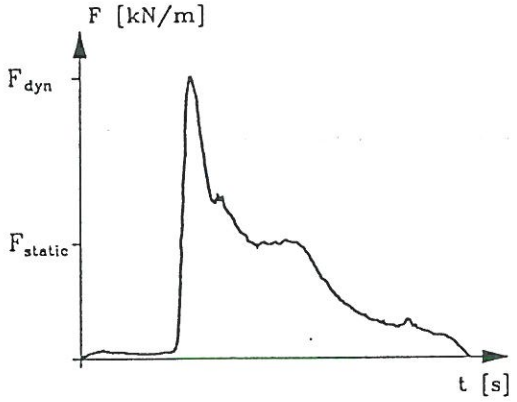

Fig. 2.1 Sketch of a typical horizontal wave load

"church-roof" load history (cf. Figure 2.2). Alternatively, a triangular load history is proposed whenever F_{dyn} is a factor two or more greater than F_{static}. The influence of the quasi-static part of the load is then neglected and the load is solely described by the maximum load, the rise time (t_r) and the decay time (t_d).

In cases where the rise time is very short, it is found convenient to use a simple exponential

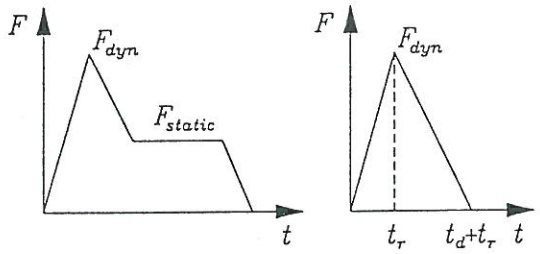

Fig. 2.2 Simple load substitutions. Redrawn from Oumeraci et al. 1992.

function for the description of the load. In this way a continuous formulation which more appropriately describes the decay and contain the total amount of energy in the the load signal is obtained. The load history is given by the maximum load and a constant describing the decay.

In both cases the maximum load is related to the static load carrying capacity of the current failure mode (q_u) by an overloading factor (S). The load substitutions are given in the equation 2 and 3, corresponding to the triangular and exponential load substitution, respectively. The load substitutions are furthermore illustrated in Figure 2.3.

$$q_d = \begin{cases} q_u\left(1-\frac{1-S}{t_a}t\right) & 0 \le t \le t_a \\ Sq_u\left(1-\frac{t-t_a}{t_b-t_a}\right) & t_a \le t \le t_b \\ 0 & t \ge t_b \end{cases} \qquad (2)$$

$$q_d = Sq_u e^{-kt} \qquad (3)$$

It is noticed, that in case of a triangular load history the static load carrying capacity has to be exceeded before the soil and the superstructure are affected.

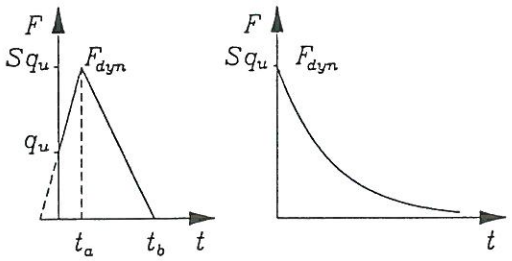

Fig. 2.3 Applied load substitutions.

2.5 Equation of Motion

It is in the following implied that the response can be described by uncoupled motions. Assuming that the time varying force acts in the same direction as the decisive displacement, it becomes possible to describe the motion by a system with only one degree of freedom. The equation of motion is established by demanding a balance between internal and external forces.

$$m\ddot{\alpha} + \Delta q_u^d \dot{\alpha} + \Delta q_u \alpha = f(t) \qquad (4)$$

where

Δq_u^d : dynamic strengthning of the soil.
Δq_u : effect of the geometrical changes.
m : total mass of the system.
$f(t)$: external force.
α : displacement.

The formulation is valid as long as the displacement is increasing.

3 References

Bjerrum, L. (1971). *Effect of Rate of Strain on Undrained Shear Strength of Soft Clay.* Norwegian Geotechnical Institute. Publ. 85. Oslo, pp. 41-42.

Das, Braja M. (1983). *Fundamentals of Soil Dynamics*. Elsvier, New York, pp. 153-211.

Ibsen, L.B. (1995). *The Static and Dynamic Strength of Sand.* XI ECSMFE, Copenhagen, 1995.

Kortenhaus, A. And Oumeraci, H. (1993) *Simple Model for Permanent Displacement of Caisson Breakwaters under Impact Loads*. Proceedings 1st. Project Workshop, MCS-Project, MAS2-CT92-0092, Part 1.

Kulhawy, F.H. and Mayne, P.W. (1990) *Manual on Estimating Soil Properties for Foundation Design.* Cornell University, Ithaca, New York, pp. 4.48-4.49.

Oumeraci, H. and Kortenhaus, A. (1992). *Analysis of the Dynamic Response of Caisson Breakwaters*, Technical report, Franzius-Institut, University of Hannover

Formulation and Integration of the Standard Linear Viscoelastic Solid with Integer and Fractional Rate Laws

Mikael Enelund
Division of Solid Mechanics, Chalmers University of Technology
SE–412 96 Göteborg, Sweden

Modeling of viscoelastic response has a long tradition for describing a variety of phenomena (such as creep, relaxation and energy dissipation or damping) in structural analysis. One particular issue, that has been discussed extensively, is how complex the linear viscoelastic model must be, *i.e.*, what is the minimum number of material parameters that is required for an accurate description of the observed material behavior?

Most engineering materials exhibit a weak frequency dependence of the damping characteristics, which is difficult to describe with classic linear viscoelasticity that are based on integer rate laws for the pertinent internal variables. However, if the integer time derivative is replaced by a fractional order derivative operator, the number of parameters to describe damping in an accurate fashion can be significantly reduced. Typically, it is sufficient to use four parameters for the uniaxial stress situation (two elastic constants, one relaxation constant and the non–dimensional fractional order), see Bagley and Torvik [1]. The reason for this is that the Fourier transforms of integer derivatives exhibit a frequency dependence that is proportional to integer order, while fractional derivatives exhibit a frequency dependence that is proportional to the fractional order. It thus follows that the order of fractional differentiation can be interpreted as a distribution variable for the corresponding continuous distribution of relaxation times. This is believed to be the main feature of using fractional derivative operators in this context. The linear viscoelastic model together with fractional derivatives has shown to be very flexible also for describing quasistatic response, such as creep and relaxation, see Enelund and Olsson [2].

Present Study and Original Features

It appears that some work concerning the use and the predictive capability of fractional derivatives have been carried out on the constitutive level, while less effort has been spent on the rational formulation for structural analysis. Although it is possible, at least in theory, to use transform techniques for evaluating the structural response for linear viscoelasticity, it appears useful in practical to employ numerical integration in time, in particular for evaluating the dynamic response. The formulation of viscoelasticity used in the present study are more general and lead to well–posed initial value problems when incorporated into a framework for structural analysis, see Enelund *et al.* [3].

In summary, thermodynamically consistent and physical sound formulations of the Standard Linear Viscoelastic Solid with integer as well as fractional order rate laws for a finite set of internal variables are presented. A time integration scheme, based on the Generalized midpoint rule, is employed for integrating the constitutive rate laws. The time integration scheme and the present viscoelastic formulation are implemented into the general purpose

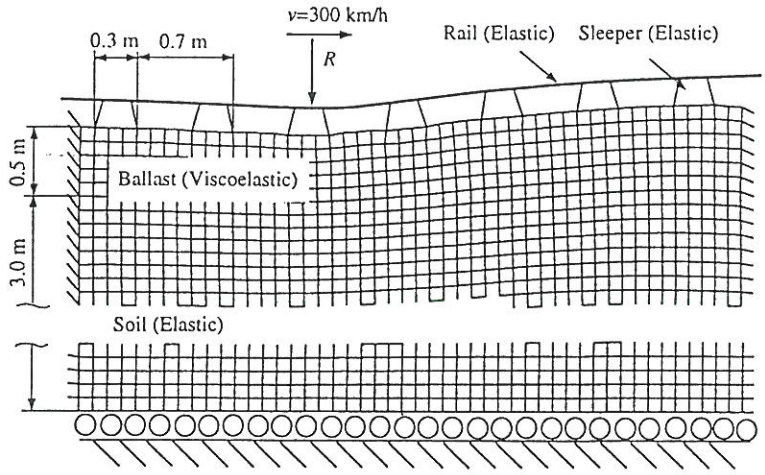

Figure 1: Geometry and magnified deformed mesh for railway track consisting of elastic sleepers and rails on a viscoelastic ballast material resting on an elastic soil layer. The system is subjected to a moving impulse load modeling a high-speeding train traveling with $v = 300$ km/h. The vertical boundaries are absorbing boundaries.

finite element code Abaqus. The integration scheme is then used together with an explicit integration scheme for integration of structural responses. The predictive capability of the present viscoelastic model is investigated both analytically and numerically. A few numerical examples consider the damped response of a layer of ballast material, that is subjected to the overrolling of high speed trains.

References

[1] Bagley, R. L., and Torvik, P. J., 1983, "Fractional calculus–A different approach to the analysis of viscoelastically damped structures", *AIAA Journal*, vol. 21, p. 741–748.

[2] Enelund, M., and Olsson P., 1995, "Damping described by fading memory models", In *Proceedings 36th AIAA/ASME/ASCE/AHS/ASC Structures, Structural Dynamics and Materials Conference*, New Orleans.

[3] Enelund, M., Mähler, L., Runesson, K., and Josefson, B. L., 1996, "Unified Formulation and Integration of the Standard Linear Viscoelastic Solid with Integer and Fractional Rate Laws", Report F192, Division of solid Mechanics, Chalmers University of Technology, Göteborg, Sweden. Presented at the *19 th International Congress of Theoretical and Applied Mechanics*, in Kyoto, Japan, August 25–31, 1996.

FRACTURE AND CRACK CROWTH IN CONCRETE
A new approach to predict crack propagation

T. Cornelius Hansen
Department of Structural Engineering, Building 118
Technical University of Denmark, 2800 Lyngby, Denmark

ABSTRACT.

It is an interesting fact, that very few theoretical crack growth formulas have been developed in the literature. Crack growth in concrete has up to now mainly been studied by using the Hillerborg Fictitious Crack Model. For metals empirical formulas, e.g. the Paris formula, have been dominating. Crack growth studies are extremely important for the design of many metal structures. For reinforced concrete structures the problem is not so obvious, because dangerous crack growth normally is prevented by the reinforcement, leaving the crack growth problem to be of importance only for massive unreinforced concrete structures like dams. There are some cases of reinforced concrete structures, however, where the failure seems to be determined by crack growth.
A newly developed crack growth model [1] based on an energy balance criterion is presented in the paper. The model leads to a first order differential equation which can predict crack propagation in mode I, and determine the strength and deformations for any loading condition. The model has recently been used to predict crack growth in metals subjected to dynamic loading [2]. Further the model has been used to estimate the crack growth in welded connections taking the effect from crack closure and residual stresses into account [3].
In this paper the model is as example compared with three point bending tests on plain concrete beams, where several parameters have been varied: the beam dimensions, the strength and the aggregate size. The paper is based on the work presented in [4].

1. INTRODUCTION.

A newly developed fracture mechanical model [1], based on an energy balance criterion is presented in the paper. The model leads to a first order differential equation which can predict crack propagation, and determine the strength and deformations for any loading condition. The purpose of this paper is to determine the load-deflection relationship for plain concrete beams in three point bending using this model.
The advantage of the model presented in this paper compared to other models of fracture mechanics for concrete is that the energy calculation is based on simple linear elastic calculations, which demand very little computation time. The non-linear behavior is taken into account, using a crack length correction based on the Irwin concept [5].
Determining the total elastic energy W in a cracked specimen using linear elasticity gives results close to the correct values, due to the fact that the stress concentration effects in the process zone close to the crack tip are negligible. Introducing an effective crack length $a_{eff} = a + l_e$, where l_e is Irwins crack length correction [5], which represent a part of the process zone, it is possible to take the non-linear behavior into account.

2. THE ENERGY BALANCE CRACK PROPAGATION FORMULA.

In the following the *energy balance crack propagation formula* (ECP) will shortly be presented. For further details the reader is referred to [1]. ECP is based on an energy criterion. Energy criteria were introduced in fracture mechanics by Griffith [6].

For a displacement controlled test, where the crack length **a** and the deflection **u** are the independent variables, the energy balance equation can be written, see [1]:

$$\frac{\partial W}{\partial a}da + G_F b da = 0 \tag{1}$$

Here **W** is the elastic energy, G_F is the fracture energy, defined as the energy needed to propagate the crack a unit area and **b** is the thickness of the specimen.

Taking the correction l_e of the crack length into account we get:

$$\frac{\partial W}{\partial a}da + \frac{\partial W}{\partial a}dl_e + G_F b da = 0 \tag{2}$$

which can be rearranged to:

$$da = \frac{-\frac{\partial W}{\partial a}dl_e}{G_F b + \frac{\partial W}{\partial a}} \tag{3}$$

Since the crack length correction l_e depends on a as well as u we have:

$$dl_e = \frac{\partial l_e}{\partial u}du + \frac{\partial l_e}{\partial a}da \tag{4}$$

Inserting this into (3) and making a few rearrangements we get:

$$\frac{da}{du} = \frac{-\frac{\partial W}{\partial a}\frac{\partial l_e}{\partial u}}{G_F b + \frac{\partial W}{\partial a}(1 + \frac{\partial l_e}{\partial a})} \tag{5}$$

The derivatives $\partial W/\partial a$ should be taken at $a+l_e$, while $\partial l_e/\partial u$ and $\partial l_e/\partial a$ may be taken at **a**. This expression is called the *energy balance crack propagation formula.*
In the symmetrical case, meaning a crack with two tips and the crack length 2a, G_F in the formula must be replaced by $2G_F$, W still being the total elastic energy.

3. NUMERICAL DETERMINATION OF CRACK GROWTH.

As described earlier the crack propagation formula is based on an energy balance criterion. It is therefore necessary to determine the elastic energy in the actual cracked body (beam,disk etc.) for arbitrary values of the load.
The elastic strain energy **W** can be determined by means of a finite element calculation. In this way **W** will be expressed as a function of the force **P** or the displacement **u** and the crack length **a**.
In the case where one wishes to determine the load-deflection curve of a concrete specimen, it is convenient to express the energy **W** by the displacement **u** and **a**.
It is common knowledge that the elastic strain energy is proportional to the square of the displacement and proportional to the modulus of elasticity. This means if we have determined W in the case of constant displacement and constant modulus of elasticity for any crack length, then we can express the energy as:

$$W(u,a) = \left(\frac{u}{u_0}\right)^2 \cdot \left(\frac{E}{E_0}\right) \cdot W_{\text{const } E,u}(a) \qquad (6)$$

The problem is now reduced to determine the elastic energy of the actual cracked body as a function of the crack length - only depending on the geometry. Very simple finite element models can be used to determine this function. We only have to calculate a number of models with similar geometry, except for the length of the crack, subject all these models to a constant displacement and determine the force P. The elastic strain energy can then be determined as a function of P and u. In the case of only one concentrated load the elastic strain energy is given by:

$$W = \tfrac{1}{2} \cdot P \cdot u \qquad (7)$$

When the elastic strain energy is determined for each crack length, a simple polynomial fit may be used to determine the elastic strain energy for constant displacement at any crack length. By increasing the crack length, the energy curve (for constant displacement) decreases as shown in figure 1 in the case of three point bending of notched beams with rectangular section.
W_0 is the strain energy related to a non cracked beam. From this curve the change in the elastic energy $\partial W/\partial a$ can be determined for any value of u and a using formula (6).

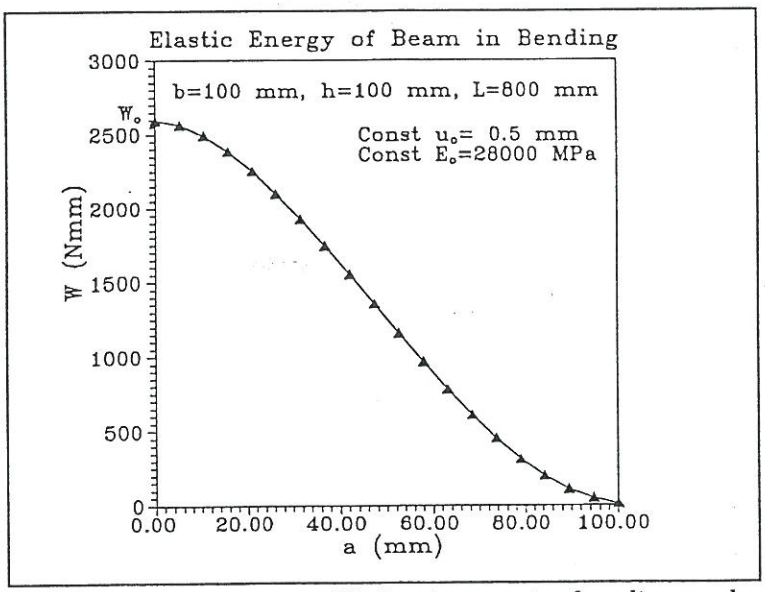

Figure 1 *Elastic energy W for three point bending under constant displacement.*

Taking into account the non-linear effects we introduce, as mentioned, the effective crack length $a_{eff} = a + l_e$. The correction length l_e is determined on the basis of Irwins concept [5]. Some energy considerations presented in [1] leads to the formula (8).

$$l_e = 0.4 \cdot \frac{K_I^2}{\pi f_t^2} \tag{8}$$

Here the stress intensity factor K_I is determined by formula (9).

$$K_I^2 = -\frac{\partial W}{\partial a}\frac{E}{b} \tag{9}$$

The correction length l_e is increasing for increasing crack length **a**, meaning that for a certain value of the crack length, the process zone a_p, which approximately is $a_p = 2.5 \cdot l_e$, see [1], will reach the top of the beam. At that point the calculation must stop, and therefore the theory does not predict fully the descending part, as will be shown in the next section.

4. COMPARISON WITH TEST RESULTS.

In this section the new theory of crack propagation will be compared with notched three point bending tests. The three point bending tests were performed at the Department of Structural Engineering, Technical University of Denmark, see [7] and [8].
For the purpose of verifying the crack propagation formula three different test series have been carried out. Several parameters were varied. Four different compression strength levels were used (f_c = 30, 50, 70 and 100 MPa). Further the ratio of the start notch and the depth of the beam a_0/h was varied being 0.1, 0.25 and 0.5. Finally the aggregate size was varied for each strength level. The maximum aggregate size d_{max} was: 0 mm, 4 mm, 8 mm and 16 mm.
As described in section 3 the theory is not able to predict the whole load-deflection curve, due to the fact that when the process zone reaches the top of the beam the assumptions used fail to be valid. Therefore the calculation is only carried out for a part of the load-deflection curve. To determine the load-deflection curve using the crack propagation theory, the following parameters have to be known: the fracture energy G_F, the tensile strength f_t and the modulus of elasticity E. As far as possible they should be determined independently of the bending test results.

The fracture energy G_F is in [7] determined using the three point bending method in accordance with the recommedations of the RILEM Technical Commity 50-FMC [9]. In this method the measured load-deflection curve does not give the total amount of energy consumed, due to the fact that the energy is not only supplied from the applied force but also from the netweight of the beam, which has to be taken into account when determining G_F. This is done using the method suggested by Hillerborg [10], putting the total energy equal to the area under the measured load-deflection curve plus the secondary part from the netweight. G_F used in the theoretical calculations will be determined on the basis of formula (10), having $\Delta a = h - a_0$ and ΔA being the full area under the measured load-deflection curves. The calculated load-deflection curves have been determined for a concentrated load only, disregarding the netweight of the beam. These curves are compared with the measured load-deflection curves, the load meaning the applied concentrated load and the deflection meaning the deflection

measured in the test having zero value when the beam is acted upon only by its own weight.

The splitting strength f_{sp} was determined for each concrete mix using standard procedures, see [7]. The tensile strength f_t used in the theory is put equal to $f_t = 1.25 \cdot f_{sp}$. This value is close to the flexural modulus f_b found in bending tests, which are higher than the uniaxial tensile strength f_u and the splitting strength f_{sp}.

The modulus of elasticity **E** was determined for all the concrete mixes by separate cylinder tests using standard procedures, see [8].
The parameters used in the calculations are listed in table 4 - 6.

	E (MPa)	G_F (N/m)	a_o (mm)	f_{sp} (MPa)	$f_t=1.25 \cdot f_{sp}$
A_303N	25160	81.1	50	2.90	3.63
A_503N	32950	64.0	50	3.76	4.70
A_703	35300	85.8	50	4.82	6.03
A_1003	42210	95.7	50	5.49	6.86

Table 4 *Parameters used in the calculations shown in figure 4.* d_{max} *= 16 mm for all specimens.*

	E (MPa)	G_F (N/m)	a_o (mm)	f_{sp} (MPa)	$f_t=1.25 \cdot f_{sp}$
A_501	33640	113.2	10	3.87	4.85
A_502	32490	106.2	25	3.72	4.65
A_503N	32950	64.0	50	3.76	4.70

Table 5 *Parameters used in the calculations shown in figure 5.* d_{max} *= 16 mm for all specimens.*

	E (MPa)	G_F (N/m)	d_{max} (mm)	f_{sp} (MPa)	$f_t=1.25 \cdot f_{sp}$
C_301	10450	3.7	0	2.00*	2.50
C_302	22120	18.0	4	2.27	2.84
C_303	27460	32.7	8	2.51	3.14
A_303N	25160	81.1	16	2.90	3.63

Table 6 *Parameters used in the calculations shown in figure 6.* a_o *= 50 mm for all specimens.*

* The splitting strength for this test series was not measured. The value is based on interpolation from the other splitting strength measurements.

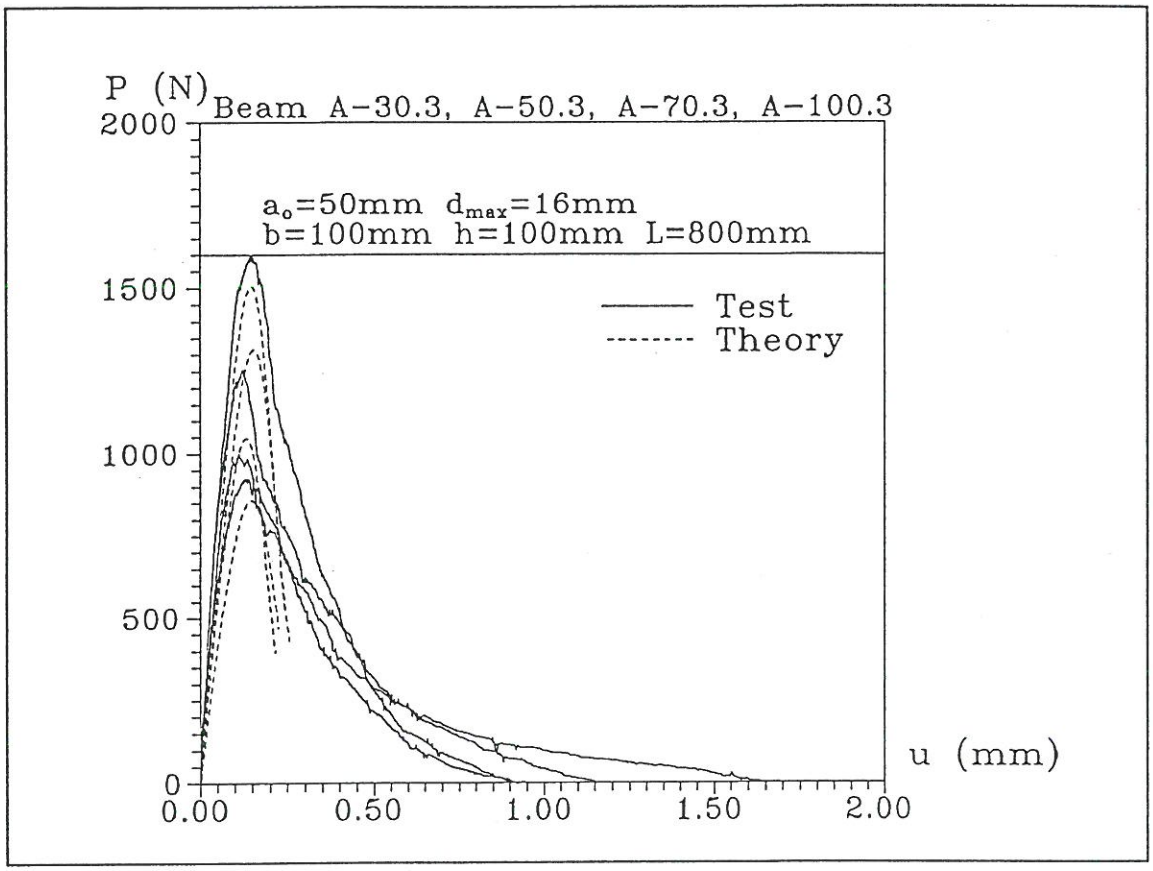

Figure 2 *Variation of Strength*

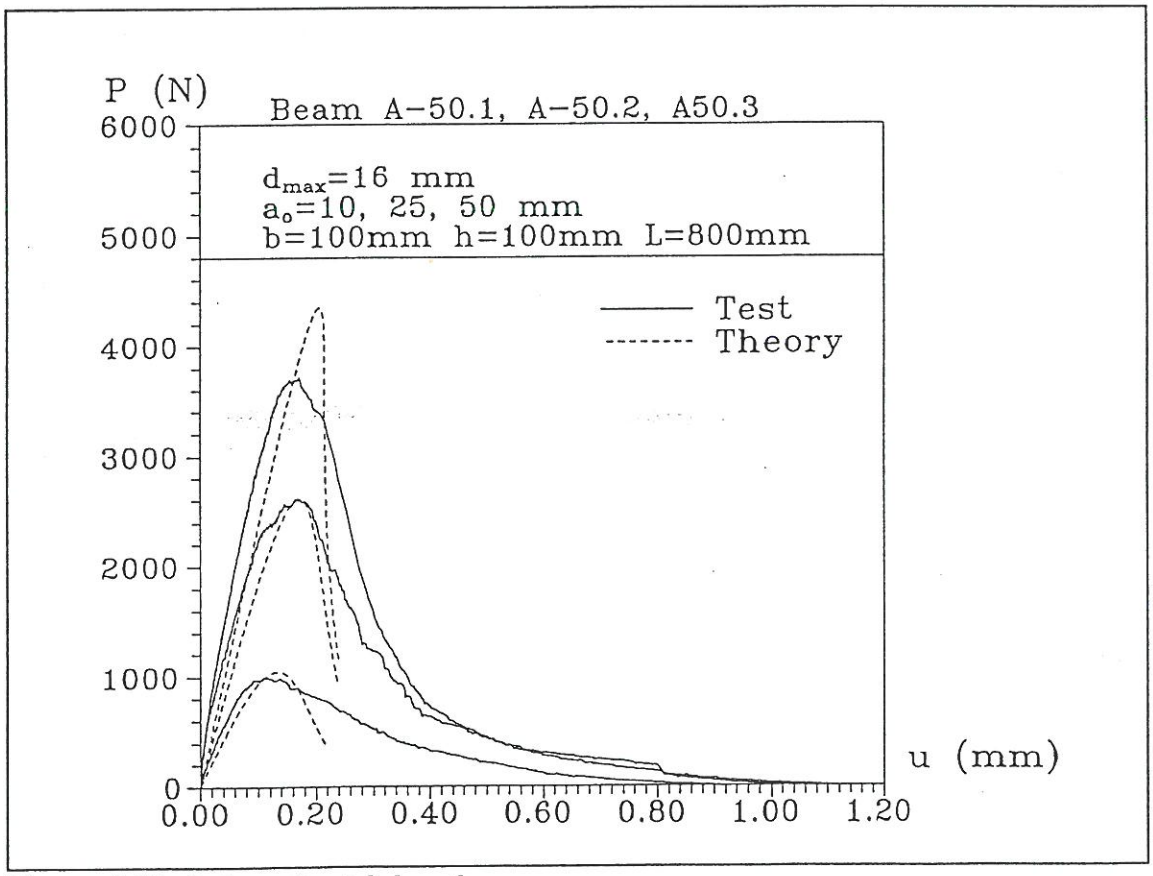

Figure 3 *Variation of notch length*

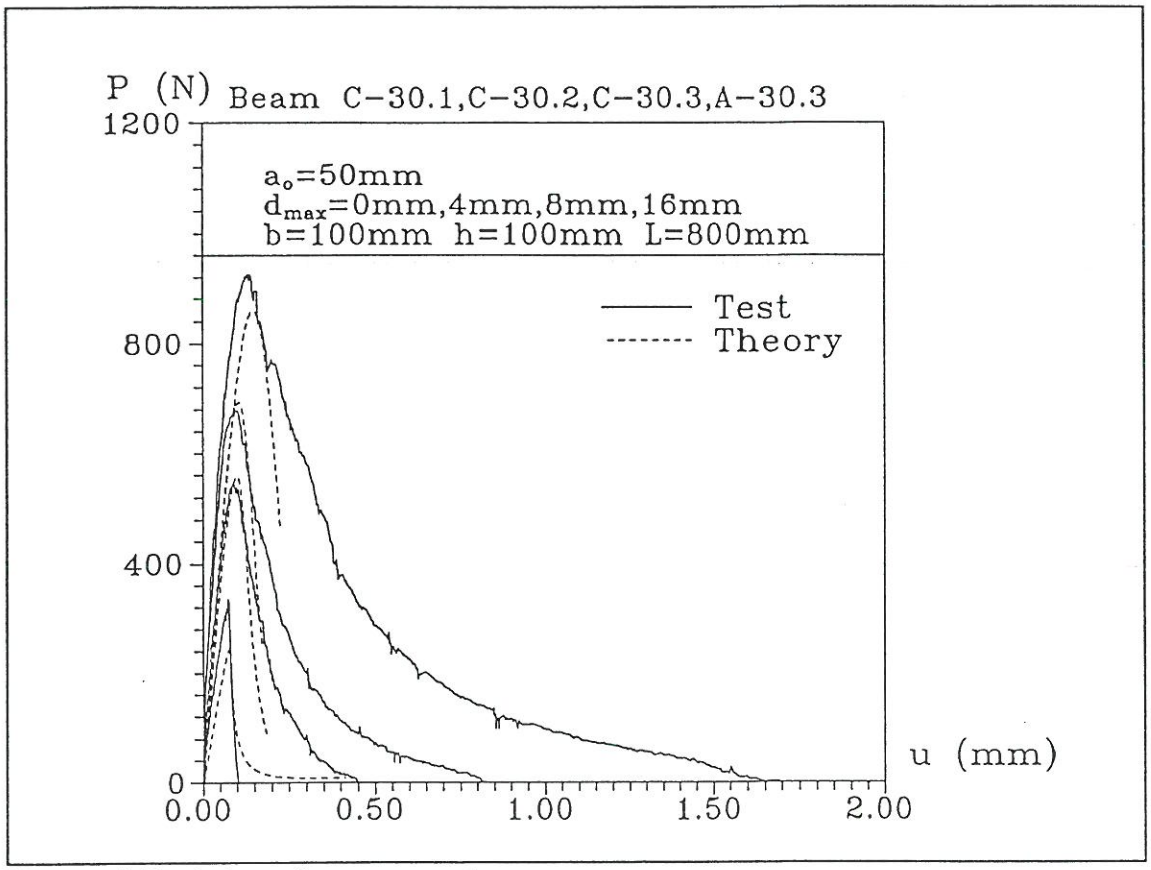

Figure 4 *Variation of aggregate size*

Figures 4-6 show the measured load-deflection curves and the ones calculated by the crack propagation formula. The aggrement is in most cases found to be excellent.

5. CONCLUSION.

The purpose of this paper has been to present a theoretical crack propagation formula and compare it to three point bending test results of plain concrete beams.
The main conclusions are that the new crack propagation theory presented is able to predict the peak value and some part of the descending part of the load deflection curve excellently in most of the cases, both for different strength levels, different ratios of start notch length and depth (a_o/h) and finally for different kinds of concrete materials (aggregate variation).

One of the main advantages of the theory is that the theory needs very small computation times to reach the results, contrary to other methods of fracture mechanics.

6. NOMENCLATURE.

a	Crack Length	E,E_o	Modulus of Elasticity
a_{eff}	Effective Crack Length	f_t	Tensile Strength
a_o	Start Notch Length	f_b	Flexural Modulus
l_e	Crack Length Correction	f_u	Uniaxial Tensile Strength
a_p	Process Zone Length	f_{sp}	Splitting Strength
u,u_o	Displacement	W	Elastic Strain Energy
b	Width	K_I	Stress Intensity Factor
h	Depth	G_F	Fracture Energy
L	Length	σ_o	Stress
A	Area	P	Load

7. REFERENCES.

[1] Nielsen, M.P., *An Energy Balance Crack Growth Formula*, Bygningsstatiske Meddelelser, nr 3-4, pp 71-125, Sept 1990.

[2] Hansen, T.C., *Fatigue and Crack Propagation*, Department of Structural Engineering, Technical University of Denmark, Report No. R316, 1994.

[3] Hansen, T.C., *Fatigue in Welded Connection,* Department of Structural Engineering, Technical University of Denmark, Report No. R10, 1996.

[4] T.C.Hansen and D.H.Olsen, *Fracture and Crack Growth in Concrete, A new approach to predict crack propagation*, Department of Structural Engineering, Technical University of Denmark, Report No.11, 1996.

[5] Irwin, G.R., *Plastic Zone Near a Crack and Fracture Toughness*, Proc, 7th Sagamore Conf, pp IV-63, 1960.

[6] Griffith, A.A., *The Phenomena of Rupture and Flow in Solids*, Phil.Trans.Soc.of London,A221, pp 163-197, 1921.

[7] Olsen, D.H., *Fracture of Concrete. A Test Series*, Department of Structural Engineering, Technical University of Denmark, Report No. R312, 1994.

[8] Olsen, D.H., *Fracture of Concrete. A Test Series. Appendix I*, Department of Structural Engineering, Technical University of Denmark, Report No. R313, 1994.

[9] RILEM, *Determination of the Fracture Energy of Mortar and Concrete by Means of Three-Point Bend Tests on Notched Beams*, Materiaux et Constructions, Vol 18, No. 106, pp.285-290, 1985.

[10] Hillerborg, A., *The Theoretical Basis of a Method to Determine the Fracture Energy G_F of Concrete*, Materiaux et Constructions, Vol 18, No. 106, pp.291-296, 1985.

Numerical analysis of damage evolution in cyclic elastic-plastic crack growth problems

B. Skallerud' and Z.L. Zhang"
' Div. Applied Mechanics, The Norwegian Institute of Technology, N-7034, Trondheim, Norway [1]
" Sintef Materials Technology, N-7034, Trondheim, Norway

Abstract

Structures subjected to severe cyclic loading may fail due to low cycle fatigue. During the latter part of the fatigue life the crack growth rate may increase due to the occurence of crack growth from static failure modes, e.g. void growth. The present investigation attempts to predict the combined crack growth by means of nonlinear FE methods. The case studied is an axially loaded flat plate with embedded, circular cracks growing under nominal cyclic plasticity, as test data for this case has been obtained previously. The fatigue part of the crack growth is determined by using the computed cyclic J-integral, and the static mode crack growth from ductile tearing is determined from computations accounting for void nucleation/growth/coalescence by means of a modified Gurson-Tvergaard model. Comparison with the test results shows acceptable correspondence in the last part of the number of cycles to failure.

Introduction

In typical fatigue loading, the structural life consists mainly of loading corresponding to high cycle fatigue. In some structures the operational loads may contain cycles in the fully plastic regime, i.e. low cycle fatigue. Additionaly, structures designed according to high cycle fatigue criteria may be subjected to accidental loads or extreme environmental loads (waves, earthquakes), leading to low cycle fatigue damage (Skallerud et al, 1995). Due to the intense loading in cyclic plasticity, the high maximum tensile loads may also lead to ductile tearing crack growth when the crack has reached a certain size. Most research in the past addresses these topics separately. In the present investigation cyclic elastic-plastic crack growth is analysed by means of nonlinear FE methods. Fig.1 illustrates the major effects in a cracked component subjected to cyclic plasticity. During the cycles the crack tip is blunting and resharpening, this is a contribution to the fatigue damage accumulation (i.e. fatigue crack growth). Furthermore, the intensely deformed material ahead of the crack tip develops voids that finally coalesce when the material follows a ductile damage mechanism. Finally, for the bulk material the stress-strain behaviour usually exhibit a transient behaviour given by cyclic hardening/softening and mean stress relaxation/ cyclic creep. For the steel under investigation in the present study this transient phase is quite short, therefore the material is assumed to follow a stabilised (saturated) behaviour from the beginning described by a cyclic stress-strain curve. One notes from Fig.1 that in addition to the complex material behaviour and large deformations, the closing and opening of the crack surface yields a contact problem. So it is fair to state that the

[1] work partially carried out during a stay at Dep.Building Tech., Univ.Aalborg, Denmark

problem is highly nonlinear. The case analysed subsequently is an axially loaded plate with embedded, circular cracks, as some test data have been obtained previously (Skallerud, 1992a). The fatigue crack growth is predicted by extension of the J-integral (Rice, 1968) to cyclic loading, ΔJ (Dowling and Begley, 1976), followed by application of this parameter in a fatigue crack growth model. The ductile tearing is predicted from the Gurson-Tvergaard model (denoted G-T model subsequently), i.e. a porous material model representative for ductile damage (Gurson, 1977, Tvergaard, 1981,1982). A refined failure criterion by Zhang and Niemi(1995a), based on a void coalescence mechanism, has been used in the fitting of the damage parameters. All numerical simulations were carried out with the ABAQUS software, and the UMAT subroutine facility is employed for the implementation of the G-T model with the refined failure criterion (Zhang, 1995b). More details may be obtained in (Skallerud and Zhang, 1996).

Damage mechanisms and models in fatigue and ductile tearing

In small scale yielding conditions the relationship between the J-integral for linear elastic materials and the Mode I stress intensity factor reads

$$\begin{aligned} J_e &= K_I^2/E' \Rightarrow K_{I,J} = \sqrt{E' J_e} \\ E' &= [\frac{E}{1-\nu^2}|_{P\epsilon}, E|_{P\sigma}] \end{aligned} \tag{1}$$

The crack tip opening displacement relates to J as:

$$J = m\sigma_y \delta_{tip} \tag{2}$$

Here, m is a constraint factor close to 1 in plane stress and approximately 2 in plane strain, for low hardening materials, presuming that J characterises the crack tip stress-strain field (HRR field) (Shih, 1981, Hutchinson, 1968, Rice and Rosengren, 1968).

In cyclic loading under small scale yielding, unloading from σ_{max} to σ_{min} (without crack closure) governs the change in δ_{tip} according to the following relationship (Rice, 1967)

$$\begin{aligned} \delta_{tip} &\propto K_I^2/E'\sigma_y \\ \Delta\delta_{tip} &\propto (\Delta K)^2/(E'2\sigma_y) \\ \Delta K &= K_{max} - K_{min} \propto (\sigma_{max} - \sigma_{min})\sqrt{\pi a} \end{aligned} \tag{3}$$

The crack tip blunting model is one way of describing fatigue damage. It is based on the cyclic process of blunting and resharpening of the crack tip (Laird and Smith, 1962, Neumann, 1974). A result from this model is that the crack advance is proportional to $\Delta\delta_{tip}$. The striation mechanism with crack advance in each cycle then leads to the following crack growth model:

$$da/dN \propto (\Delta K)^2 \tag{4}$$

A semi-empirical model usually has to be utilised (Paris and Erdogan, 1963):

$$da/dN = C_1(\Delta K)^{n_1} \tag{5}$$

n_1 is typically between 2 and 4, and close to 3 for structural steel. Fig.2a illustrates schematically typical fatigue crack growth rates in log-log axes. For high cyclic loading in the ligament (due to a large crack or small crack/high nominal load), the small scale yielding parameter K_I is invalidated. Now the J-integral is a possible parameter for describing control of the crack tip damage process zone. J is derived for a nonlinear elastic (deformation plastic) material, and may be written as the sum of an elastic and a plastic contribution (Shih and Hutchinson, 1976):

$$J = \int_\Gamma (W n_1 - t \cdot \frac{\partial u}{\partial x_1}) ds \approx J_e + J_p \tag{6}$$

$$W = \int_0^\epsilon \sigma : d\epsilon, \sigma = \frac{\partial W}{\partial \epsilon} \tag{7}$$

Although application of J in cyclic loading does not have a firm theoretical basis as for monotonic loading, it is still a relevant candidate for correlation of fatigue crack growth under large scale yielding. The energy dissipated per cycle at the crack tip is also a possible damage parameter. The requirement of proportional straining is not necessary in such an approach. However, the link between K and J yields a possibility to obtain fatigue crack growth parameters applicable in the elastic-plastic regime also, utilising the linear elastic region parameters . Dowling(1978) utilised the connection between J and the elastic and plastic strain energy in cyclic loading for axially loaded specimens, where the strain energy in a cycle was taken as the area under the stress-strain curve starting at $(\sigma_{min}, \epsilon_{min})$ and ending at $(\sigma_{max}, \epsilon_{max})$:

$$\Delta J = F_{g,el} \Delta W_e a + F_p(a,n) \Delta W_p a \tag{8}$$

$$\Delta K_J = \sqrt{E' \Delta J} \tag{9}$$

This approach presumes insignificant effects of crack closure, and employs the the Masing-hypothesis (Masing, 1926). The F factors account for finite geometry, crack shape and strain hardening (Shih and Hutchinson, 1976). Note that the energies should account for eventual effects of crack closure, i.e. ΔJ is effective. By correlating ΔK_J to the low cycle fatigue crack growth, a linear relationship was obtained in log-log axes, located in the *extrapolated* Paris' region (Dowling and Iyyer, 1987, McClung and Hudak, 1994, Joyce et al, 1994):

$$da/dN = C_2(\Delta K_J)^{n_2} \approx C_1(\Delta K_J)^{n_1} \tag{10}$$

The definition of ΔJ is (Tanaka, 1983)

$$\begin{aligned} \Delta J &= \int_\Gamma (\Delta W n_1 - \Delta t \cdot \frac{\partial \Delta u}{\partial x_1}) ds \\ &\approx \Delta J_e + \Delta J_p \\ \Delta W &= \int_{\epsilon_{min}}^{\epsilon_{max}} (\sigma - \sigma_{min}) : d\epsilon, \\ \Delta \sigma &= \frac{\partial \Delta W(\Delta \epsilon)}{\partial \Delta \epsilon}, \Delta t = t_{max} - t_{min} \end{aligned} \tag{11}$$

Eqn.(11) is only valid for a stabilised material response (Yoon and Saxena, 1991), i.e. cyclic hardening/softening is saturated. For the steel analysed subsequently this transient

material behaviour is moderate and quite rapid (Skallerud, 1992b). Hence, ΔJ determination should be acceptable. Note that $\Delta J \neq J_{max} - J_{min}$, but is obtained by developing Eqn.(11)

$$\Delta J = J_{max} - J_{min} - \int_{\Gamma}(\sigma_{min} : (\epsilon_{max} - \epsilon_{min})n_1 - t_{max} \cdot \frac{\partial u_{min}}{\partial x_1} + t_{min} \cdot \frac{\partial u_{max}}{\partial x_1})ds \quad (12)$$

This means that the computed J_{max}, J_{min} by means of Eqn.(6) or the virtual crack extension method implemented in ABAQUS is not feasible. The only implementation of Eqn.(11) known to the authors has been performed by Lambert et al(1988), where the results computed corresponded well with ΔJ values both calculated from the load-displacement curves in tests and the numerically determined load-displacement curves, hence according to the area under the loading part of the load-displacement curve, see Figs.2b and 2c. A way of utilising the results from ABAQUS for ΔJ determination is presented subsequently.

Considering Fig.2a, for a further increase in ΔK_J, the log-linear relationship breaks down, and an increase in crack growth rate develops. This increase may be attributted to static fracture modes, e.g. from ductile tearing. Previous studies show that for some materials the interaction between the fatigue mode and static modes is negligible (Kaiser, 1983, Chell, 1984, Neale and Priddle, 1988), and the increased crack growth due to ductile tearing may be simulated by an amplification factor obtained from a monotonic J_R curve:

$$da/dN = da/dN|_{fatigue} + da/dN|_{tearing} \quad (13)$$

$$\Rightarrow da/dN = C_3(\Delta J)^{n_3}/(1 - \frac{T_{max}}{T_{mat}}) \quad (14)$$

$$\frac{T_{max}}{T_{mat}} = \frac{dJ_{max}/da}{dJ_{mat}/da}$$

By this method the upturn of the $da/dN - \Delta K$ curve, Fig.2a, is obtained.

Eqn.(14) is not utilised herein. Instead, as the damage process in ductile tearing usually consists of void nucleation/growth/coalescence, a micro-mechanical model originally proposed by Gurson(1977), and later modified by Tvergaard(1981) and Tvergaard and Needleman(1984), is employed with some modifications. By assuming that the matrix material is characterised by a Mises material and the void shape is kept spherical, using upper bound theory, Gurson derived a plastic potential for a voided solid that returns to the Mises yield surface for zero void volume fraction:

$$\Phi(\sigma, f, \overline{\sigma}) = \frac{q^2}{\overline{\sigma}^2} + 2q_1 f cosh(\frac{3q_2\sigma_m}{2\overline{\sigma}}) - 1 - (q_1 f)^2 = 0 \quad (15)$$

$$q^2 = \frac{3}{2}s : s \quad , \quad s = \sigma - \sigma_m I, \sigma_m = \frac{1}{3}\sigma : I$$

Here f is the void volume fraction, $\overline{\sigma}$ is the matrix material yield stress, $q_1 = 1.5$ and $q_2 = 1$ are parameters introduced by Tvergaard for better correspondence to FE results, σ is the Cauchy stress tensor, I is the second order unit tensor.

During loading the void volume fraction increase is governed by:

$$df = df_{nucleation} + df_{growth} \quad (16)$$

$$df_{growth} = (1-f)d\epsilon^p : I$$
$$df_{nucleation} = Ad\bar{\epsilon}^p$$

where ϵ^p is the plastic strain tensor, $d\bar{\epsilon}^p$ is the equivalent plastic strain increment, and A the void nucleation parameter described by (Chu and Needleman, 1980). By equivalence of overall and matrix plastic work, the equivalent plastic strain increment controlling matrix hardening reads

$$d\bar{\epsilon}^p = \frac{\sigma : d\epsilon^p}{(1-f)\bar{\sigma}} \tag{17}$$

The overall plastic strain increment is given by the associated flow rule $d\epsilon^p = d\lambda\partial\Phi/\partial\sigma$. The Gurson model itself is not able to predict void coalescence. An extra criterion for void coalescence should be used. To account for this, f is replaced by f^* in Eqn.(15). f^* equals f for $f \leq f_c$, and $f_c + \frac{f_u^* - f_c}{f_F^* - f_c}(f - f_c)$ otherwise. Note that a failure criterion is inherent, namely the void volume fraction at coalescence, f_c, and it is determined by numerical simulations of simple tensile tests. Zhang and Niemi(1995a) modified f_c, taking it to be the value of f when a void coalescence criterion, based on Thomason's localisation criterion (Thomason, 1989), is fulfilled. Hence, a physical criterion is employed.

In the investigation by Skallerud(1992a), the test specimen shown in Fig.3a was used. It is a flat plate buttwelded at midsection. The base material is of type St52-3N, a normalised CMn structural steel typically applied in the offshore industry. The monotonic and cyclic stress-strain curves are plotted in Fig.3b. The weld matched the base material.

The testing was carried out in axial loading, with the base metal nominal axial strain as controlling parameter, analogous to LCF testing of cylindrical specimens. The strain was monitored by means of clip gages with a measurement length of 10mm. None of the specimens contained fatigue precracks.

Although the crack growth initiated and grew differently among the ten plates tested, the crack growth rate could be correlated to the nominal strain amplitude as

$$da/dN = 35600\epsilon_a^{3.09}a \tag{18}$$

Two of the specimens developed cracks growing from a weld root inclusion as an embedded, approximately circular crack. The micrographs in Fig.4 show one of the crack surfaces, with clear striation patterns. For this test the nominal strain amplitude was 1.3% and the number of cycles to failure was 80. The insets show the fracture surfaces at a≈1mm and 7mm, respectively. For the smallest crack, no sign of dimples representing necking between voids is observed, whereas for the large crack dimples clearly are visible. Fig.5 shows the comparison between the measured crack growth for this specimen and that predicted by Eqn.(18).

In the following it is attemted to predict da/dN from fatigue and ductile tearing contributions according to Eqn.(13) by means of computed values of fatigue and tearing crack growth. The specimen described above is used in all simulations, as it have a well defined crack shape and growth behaviour.

FE formulation and modelling

Large deformations are accounted for in all analyses, i.e. an updated Lagrangian formulation combined with the algorithm presented by Hughes and Winget(1980) accounting for large rigid body rotations (Hibbitt et al,1992).

In the tearing analyses the large deformations are important due to the intense straining at the crack tip and the simultaneous void nucleation/ growth/coalescence. Utilising the G-T model in the FE analyses, hence accounting for the voids, the tangent stiffness at an integration point provides a vanishing stress carrying capability after void coalescence, and tearing is simulated element by element for increasing external loading. The continuum expression for the tangent stiffness reads:

$$\hat{\tau}_{ij} = C^{ep}_{ijkl} : dD_{kl} \forall (\Phi = 0, d\sigma : \frac{\partial \Phi}{\partial \sigma} > 0) \tag{19}$$

$$C^{ep}_{ijkl} = \frac{E}{1+\nu}(\delta_{ik}\delta_{jl} + \frac{\nu}{1-2\nu}\delta_{ij}\delta_{kl} - \frac{P_{ij}P_{kl}}{\overline{E}}) \tag{20}$$

$$P_{ij} = \frac{3}{2}\frac{s_{ij}}{\overline{\sigma}} + \eta\frac{1+\nu}{1-2\nu}\delta_{ij}$$

$$\eta = \frac{f}{2}q_1 q_2 sinh\frac{3q_2\sigma_m}{2\overline{\sigma}}$$

$$\overline{E} = (1+\nu)\frac{\overline{H}}{E} + \frac{3q^2}{2\overline{\sigma}^2} + 3\eta^2\frac{1+\nu}{1-2\nu}$$

$$\overline{H} = -\frac{\overline{\sigma}}{2}[3\eta(1-f)\frac{\partial \Phi}{\partial f} + (\frac{\partial \Phi}{\partial \overline{\sigma}} + A\overline{h}\frac{\partial \Phi}{\partial f})(\frac{q^2}{\overline{\sigma}^2} - \eta\frac{3q_2\sigma_m}{2\overline{\sigma}})\frac{\overline{h}}{1-f}]$$

$$\overline{h} = d\overline{\sigma}/d\overline{\epsilon}^p$$

Here $\hat{\tau}_{ij}$ is the Jaumann rate of the Kirchoff stress, and D_{kl} is the rate of deformation tensor components. The constitutive equations were implemented via the user material facility in ABAQUS by means of the backward Euler integration method. A consistent tangent operator was utilised, hence the quadratic rate of convergence in the Newton method solving the global equilibrium was preserved. Confer Zhang and Niemi(1995b) and Zhang(1995b) for details.

In the cyclic analyses a bi-linear kinematic hardening model as implemented in ABAQUS is applied. The continuum expression reads:

$$\hat{\tau}_{ij} = \frac{E}{1+\nu}[\delta_{ik}\delta_{jl} + \frac{\nu}{1-2\nu}\delta_{ij}\delta_{kl} - \frac{3(s_{ij}-\alpha^*_{ij})(s_{kl}-\alpha^*_{kl})}{2\sigma_y^2(1+\frac{\overline{h}}{3G})}]D_{kl} \tag{21}$$

Here α^*_{kl} represents the deviatoric part of the back stress tensor, and G is the shear modulus. $\sigma_y = 360MPa$ and $\overline{h} = 2200MPa$ were applied as an approximate description of the cyclic stress-strain behaviour. This represents closing of the hysteresis loops, and contains no transient material behaviour. Modelling of the transient behaviour is given in (Skallerud, 1992b).

Initially some plane strain analyses were carried out. These did not give acceptable results. Therefore, it was decided to run 3D analyses of the component. Due to symmetries, only 1/8 of the specimen was modelled. The crack sizes analysed subsequently are a=c=3mm, 5mm, 6mm, 7mm, and 8mm, respectively. The local mesh arrangements in

the crack tip region for the three models are excactly the same. Fig.6 illustrates the FE mesh for a=c=5mm. The size of the brick elements at the crack tip, and in the prospective crack growth direction, was 0.033mm. In most cases a 20 noded solid element with reduced integration (2x2x2 Gauss points) was applied. In the cyclic analyses the same mesh, but with 8 noded solid elements instead, were used due to computer time consumption. In the cyclic analyses uniaxial gap elements were used at the crack surface. Hence, the numerical results accounted for crack opening and closure, and these effects could be monitored. The analyses were run in displacement control, with boundary displacements corresponding to the nominal strain amplitude in the test.

The calibration of the Gurson model parameters was obtained from a tensile test of the steel. The results are: $q_1 = 1.25$, $q_2 = 1.0$, $f_0 = 0.00033$, $f_c = 0.026$, $f_N = 0.006$, $f_F = 0.15$. Confer Skallerud and Zhang(1996) for details.

Numerical simulations

Ductile tearing analyses

Fig.6 shows the finite element mesh for the 5 mm crack. The dimensions of the model are 60·30·10mm. As normal practice for ductile tearing analyses, uniform square elements have been used. There are 4368 nodes and 808 20-node elements in the 5 mm crack mm model. The number of elements in all models are of the same magnitude. The void volume fractions as a function of the nominal strain at the most critical integration point at crack tip location A (largest ligament) for the three models are compared in Fig.7a. It is interesting to note that for the 3 mm crack model, there is no ductile crack growth even when the nominal strain is larger than 2%. According to the damage model, however, the ductile tearing will start to appear when the nominal strain is about 0.5%. For the 5 mm crack model the ductile crack growth will start at the nominal strain 1.4%. In other words, the ductile tearing will begin to contribute to the total crack growth in the fatigue test when the overall crack size has reached 5 mm.

Fig.7b shows the ductile crack growth at location A (largest ligament) as a function of the nominal strain for the 5,6,7,8 mm crack models. The numerical crack is defined as the part of material in the crack plane where the loading capacity has "disappeared". In the numerical analyses, a small amount of the loading capacity was remaining even when the crack has advanced in order to avoid numerical problems. The crack growth for the 6,7,8 mm models at the applied nominal strain amplitude 1.3% is about 0.05mm, 0.15mm, 0.45mm, respectively.

Cyclic analyses

Fig.8a shows one (stable) computed load-displacement loop for the specimen with the 5mm crack. It is observed that globally, no sign of crack closure is detected in this 3D model. This complies with test results.

Fig.8b illustrates the evolution of the load in the gap element nearest to the crack tip (location A in the 3D model) during 1.5 cycle. The force is zero as long as the crack is open, then just after unloading, this element makes contact. During further unloading this element force reduces slightly as the other gap elements come into contact. At (fictitious) time 1.0 the slope of the nominal load-displacement curve changes from negative to positive as the tensile excursion begins. Almost immidiately the gap force vanish, i.e. the crack

crack a(mm)	da/dN, fatigue(mm/cycle)	da/dN, tearing(mm)	Total pred.	Total,test
3	0.02	0.0	0.02	0.16
5	0.09	0.0	0.09	0.26
6	0.15	0.05	0.2	0.32
7	0.24	0.15	0.37	0.37
8	0.39	0.45	0.84	0.42

Table 1: Predicted and observed crack growth rates

opening load corresponds approximately to minimum load. This is in accordance with the study by Dowling and Iyyer(1987), showing low crack opening loads for axially loaded specimens tested in cyclic plasticity. Hence, it is reasonable to take the full loading branch into account when computing J integrals, cfr. Fig.2c. The simulations showed that after the first tensile excursion the gap element displacements saturated to constant values.

As $\Delta J \neq J_{max} - J_{min}$, the J values obtained by ABAQUS during the cyclic loading could not be utilised. However, as the crack opens near the minimum load, a numerical ΔJ may be calculated by taking the doubled stress-strain curve as material model (Masing-hypothesis), and subject the cracked component to $2\epsilon_a$ monotonically. This is analogous to the way the area under the load- displacement curve in cyclic loading is used in obtaining test result ΔJ, see Fig. 2b and 2c (Dowling,1978, Lambert et al, 1988). Using this method the J integral evolution for the three crack sizes is plotted in Fig.9. The x-axis is the fictitious analysis time, a similar evolution is exhibited in terms of nominal strain. Nine locations at the crack tip, each with six contours, were employed in calculation of J. Fig.9 shows the J-values at points A and B, and some contour values for point A in order to assess path dependecies. The path dependency is small (but increasing for increasing crack size) . For the 3mm, 5mm, 7mm cracks the following ΔJ values are obtained: 150 N/mm, 400 N/mm, 800 N/mm, respectively.

Correlation to test data

Determining the crack growth rates in the test for a=3mm,5mm,6mm,7mm,8mm , utilising Eqn.(18), gives the following results: 0.16mm/cycle, 0.26mm/cycle, 0.32mm, 0.37mm/cycle, 0.42mm, respectively. As the steel under consideration is a typical structural steel, representative crack growth in the small scale yielding regime is given as (Barsom, 1971):

$$da/dN = 3.5 \cdot 10^{-12}(\Delta K_J)^3, MPa\sqrt{m}, m/cycle \qquad (22)$$

Extrapolating this curve into the large scale yielding regime, see Fig.2a, and employing the computed ΔJ values to determine ΔK_J, the fatigue crack growth rates obtained from Eqn.(22) are listed in Table 1, second column. One observes that the crack growth rate is significantly underpredicted for the two smallest cracks, and in reasonable correspondence for a$\geq$6mm. The crack size versus number of cycles in the last part of the fatigue life is plotted in Fig.10, both for predictions and test results. It is assumed that the crack has been correctly calculated for a$\leq$5mm. This is done since the too gentle slope of the predicted curve, due to the inaccurate fatigue crack growth calculation, would obscure the last part of the prediction where both damage mechanisms operate.

Discussion

The maximum J-values (at strain amplitude 0.013) corresponding to crack size 3mm, 5mm, and 7mm are: less than the numerical crack initiation value (J_c), approximately at the initiation value, and above, respectively. This corresponds to the micrographs of the fracture surface that shows a slight tendency of ductile damage for a=5mm, and a significant ductile damage development for a=7mm.

During the cyclic loading, for a<5mm the fatigue damage mechanism dominates the crack growth. The predicted fatigue crack growth is under-estimated by a factor of 8 and 2.5 for a=3mm and 5mm, respectively. There are several sources for this deviation from the observed behaviour:

1) The crack grows through the weld material from the weld root and outwards. The analyses assume homogenous material in the weld, the real material will exhibit spatial variations both with respect to fatigue crack growth characteristics and stress-strain behaviour.

2) In the ΔJ calculation the cyclic stress-strain behaviour has been simplified by a bi-linear stress-strain curve. The crack growth parameters in the Paris' equation (Eqn.(26)) for the steel will also be an approximation, as it is a mean curve, with typical scatter of ± 2 on crack growth.

3) The way of calulating ΔJ is a simplified method utilising a purely monotonic analysis with the Masing-hypothesis in material behaviour and strain *range* as input. Although this approach seems to be reasonable, the test for its accuracy is obtained if an implementation of Eqn.(11) is carried out.

4) The finite element analyses show that the crack opens near minimum load. Therefore, it is assumed that the full loading branch is contributing to crack growth, i.e. negligible crack closure. This result corresponds to a stationary crack. For the real situation (a growing crack), some actual crack closure variation affecting the fatigue crack growth may, however, be operative. But due to the intense compressive loading, this effect is probably small.

For a>5mm the ductile tearing starts to contribute to the crack growth. In our analyses it is assumed that this growth can be determined by analysing the virgin material monotonically, and utilise the G-T based constitutive model. Considering a nucleated void in the material in front of the advancing crack tip, the assumption of a spherical shape may be invalidated. A void, initially spherical, may change into an oblate shape during the large compressive loading applied in the analyses. The oblate void could actually approach a penny shaped defect if the compressive loading is large enough. When this void is reloaded in tension, the material around the void is more intensively strained compared to a spherical void. How this may increase damage growth during the load cycling is a topic for future investigations.

In summary, the predicted crack growth by adding up fatigue contributions and ductile crack growth contributions is considered to be in acceptable accordance to the test result. But there is a need for more numerical work on the feasibility of the ΔJ determination, and experimental work on other materials in order to reveal possible damage interaction that invalidates a simple linear sum of fatigue and tearing crack growth rate.

References

•Barsom, J.M. (1971) Fatigue crack propagation in steels of various strengths, *J. Engng Ind., ASME*, no.4, 1190.
• Brocks, W. (1995). Numerical round robin on micromechanical models. Fh-IWM report T8/95.
• Chell, G.G. (1984) Fatigue crack growth laws for brittle and ductile materials including the effects of static modes and elastic-plastic deformation. *Fatigue Fract. Engng Mater. and Struct.*, **7**, 237-250.
• Chu, C.C, and Needleman, A. (1980) Void nucleation effects in biaxially stretched sheets. *J. Engng Mater. Tech.*, **102**, 249-256.
• Dowling, N.E., Begley, J.A. (1976). Fatigue crack growth during gross plasticity and J-integral. *ASTM STP 590*, 82-103.
• Dowling, N.E. (1978). Crack growth during low cycle fatigue of smooth axial specimens. *ASTM STP 637*, 97-121.
• Dowling, N.E, and Iyyer, N.S. (1987) Fatigue crack growth and closure at high cyclic strains. *Mater. Science Engng*, **96**, 99-107.
• Franklin A. G. (1969) Comparison between a quantitative microscopic and chemical method for assessment on non-metallic inclusions. *J. Iron and Steel Inst.*, **207**, 181-186.
• Gurson, A.L. (1977). Continuum theory of ductile rupture by void nucleation and growth: Part I - Yield criteria and flow rules for porous ductile media. *J. Engng Mater. Tech.*, **99**, 2-15.
• Hibbitt, Karlson, and Sorensen (1992) ABAQUS Theory manual.
• Hughes, T.J.R, and Winget, J. (1980) Finite rotation effects in numerical integration of rate constitutive equations arising in large deformation analysis. *Int.J. Numerical Meth. Engng*, **15**, 1862-1867.
• Hutchinson, J. (1968). Singular behaviour at the end of a tensile crack in a hardening material. *J. Mech. Phys. Solids*, **16**, 13-31.
• Joyce, J.A., Hackett, E.M., and Roe, C. (1994) Effects of cyclic loading on the deformation and elastic plastic fracture behaviour of a cast stainless steel. *ASTM STP 1202*, eds. Landes, McCabe, and Boulet, 722-744.
• Kaiser, S. (1983) On the relation between stable crack growth and fatigue. *Fatigue Fract. Engng Mater. and Struct.*, **6**, 33-49.
• Koplik J. and Needleman A. (1988) Void growth and coalescence in porous plastic solids. *Int. J. Solids Struct.*,**24**, 835-853.
• Laird, C., and Smith, G.C. (1962). Crack propagation in high stress fatigue. *Philosophical Magazine*, **7**, 847-857.
• Lambert, Y., Saillard, P., and Bathias, C. (1988) Application of the J concept to fatigue crack growth in large scale yielding. *ASTM STP 969*, ed. T.A.Cruse, 318-329.
• Masing, G. (1926) Eigenspannungen und verfestigung beim messing. *Proc. 2. Int. Congress Applied Mech.*, Zhurich, 332-335.
• McClung, R.C., and Hudak, S.J. (1994) Surface crack growth in Inconel 718 during large unload-reload cycles. *ASTM STP 1202*, eds. Landes, McCabe, and Boulet, 706-721.
• McEvily, A.J. (1982) On the quantitative analysis of fatigue crack propagation. *ASTM STP 811*, eds. J.Lankford, D.L.Davidson, W.L.Morris, and R.P.Wei, 283-312.
• Neumann, P. (1974). *Acta Metall.*, **22**, 1155-1165.

• Neale, B.K., and Priddle, E.K. (1988) On fatigue crack growth and stable tearing. *Fatigue Fract. Engng Mater. and Struct.*, **11**, 31-43.
• Paris, P.C., and Erdogan, F. (1963) A critical analysis of crack propagation laws. *J. Basic Engng*, **85**, 528-534.
• Rice, J. (1967). Mechanics of crack tip deformation and extension by fatigue. *ASTM STP 415*, 247-309.
• Rice, J. (1968). A path independent integral and the approximate analysis of strain concentration by notches and cracks. *J. Applied Mech.*, **35**, 379-386.
• Rice, J., and Rosengren, G.F. (1968). Plane strain deformation near a crack tip in a power law hardening material. *J. Mech. Phys. Solids*, **16**, 1-12.
• Shih, C.F., and Hutchinson, J.W. (1976). Fully plastic solutions and large scale yielding estimates for plane stress crack problems. *J. Engng Mater. Tech.* , **98**, 289-295.
• Shih, C.F. (1981). Relationships between the J-integral and the crack opening displacement for stationary and opening cracks. *J. Mech. Phys. Solids*, **29**, 305-326.
• Skallerud, B. (1992a). On the relationship between low cycle fatigue and crack growth rate properties in welded steel components. *Fatigue Fract. Engng Mater. and Struct.*, **15**, 43-56.
• Skallerud, B. (1992b). Constitutive modelling of cyclic plasticity and some implications for the computation of biaxial low cycle fatigue. *Engng Fract. Mech.*, **41**, 753-769.
• Skallerud, B., Amdahl, J., Eide, O.I., and Johansen, A. (1995). On the capacity of tubular T-joints subjected to severe cyclic loading. *Proc. Offshore Mechanics and Arctic Engng (OMAE)*, Copenhagen, **1***B*,133-143.
• Skallerud, B., and Zhang, Z. (1996). A 3D numerical study of ductile tearing and fatigue crack growth under nominal cyclic plasticity. *Int. J. Solids Struct.*, in press.
• Sun D. Z., Siegele D., Voss B. and Schmitt W. (1989) Application of Local Damage Models to the Numerical Analysis of Ductile Rupture. *Fatigue Fract. Engng Mater. Struct.*, **12**, 210-212.
• Tanaka, K. (1989) Mechanics and micromechanics of fatigue crack propagation, *ASTM STP 1020*, eds. R.P.Wei and R.P.Gangloff, 151-183.
• Thomason, P.F. (1989) *Ductile fracture of metals.* Pergamon Press.
• Tvergaard V. (1981) Influence of voids on shear band instabilities under plane strain conditions. *Int. J. Fract.*, **17**, 389-407.
• Tvergaard V. (1982) On localization in ductile materials containing spherical voids. *Int. J. Fract.*, **18**, 237-252.
• Tvergaard V. and Needleman A. (1984) Analysis of the cup-cone fracture in a round tensile bar. *Acta Metall.*, **32**,157-169.
• Xia, L., and Shih, C.F. (1995) Ductile crack growth-I. A numerical study using computational cells with microstructurally based length scales, *J.Mech.Phys. Solids*, **43**, 233-259.
• Yoon, K.B., and Saxena, A. (1991). An interpretaion of ΔJ for cyclically unsaturated materials. *Int.J. Fract,*, **49**, 3-9.
• Zhang Z. L. (1995a) A methodology for determining the Gurson parameters, work in preparation.
• Zhang Z. L. (1995b) Explicit consistent tangent moduli with a return mapping algorithm for pressure-dependent elastoplasticity models. *Comput. Meths. Appl. Mech. Engng*, **121**, 29-44.
• Zhang Z. L. and Niemi E. (1995a) A new failure criterion for the Gurson-Tvergaard

dilatational constitutive model. *Int. J. Fract.*, 70, 321-334.
• Zhang, Z.L:, and Niemi, E. (1995b). A class of generalised mid-point algorithms for the Gurson-Tvergaard material model. *Int, J. Numerical Meth. Engng*, 38, 2033-2053.

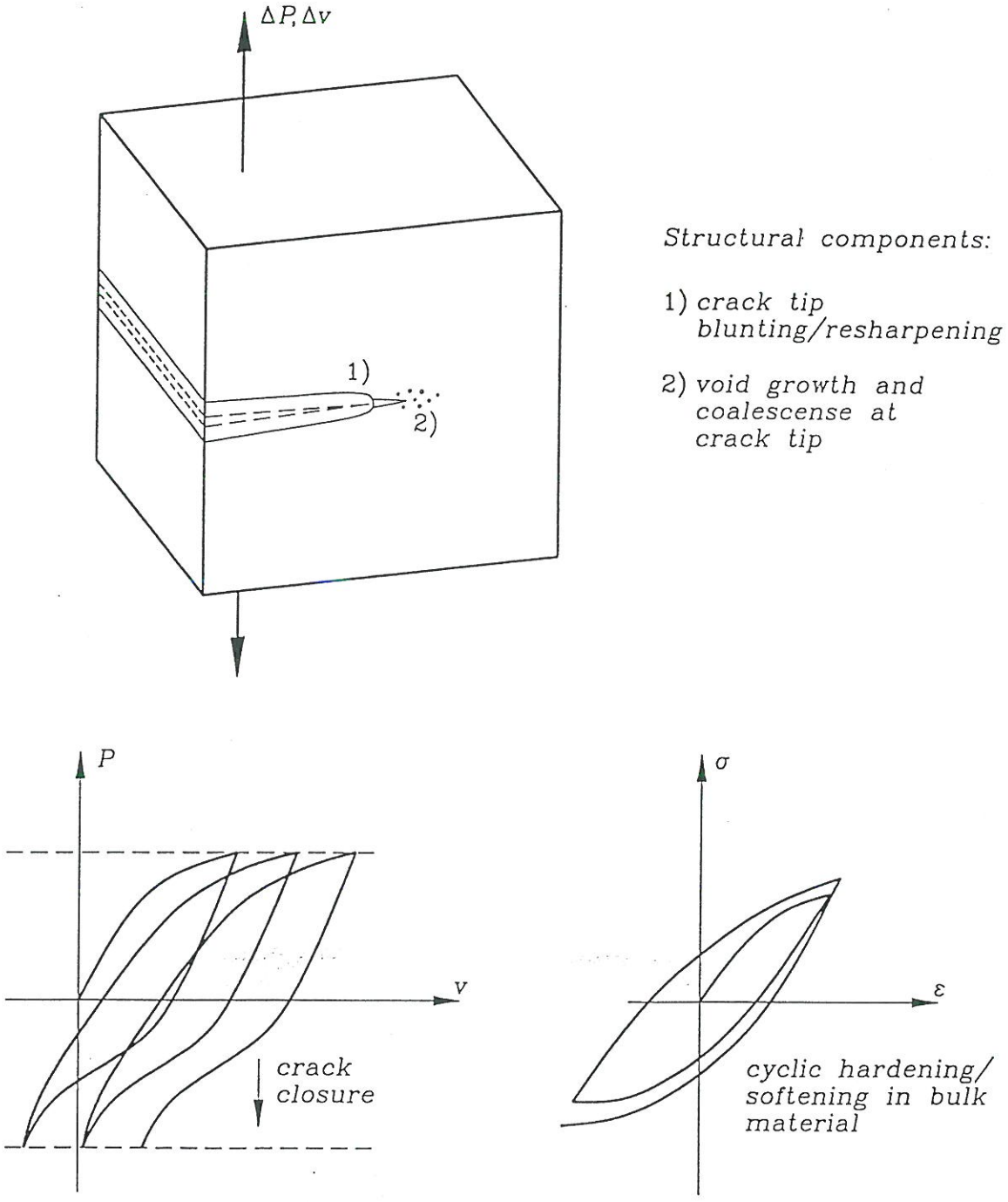

Figure 1: Constitutive model and damage evolution effects in cyclic elastic-plastic crack growth.

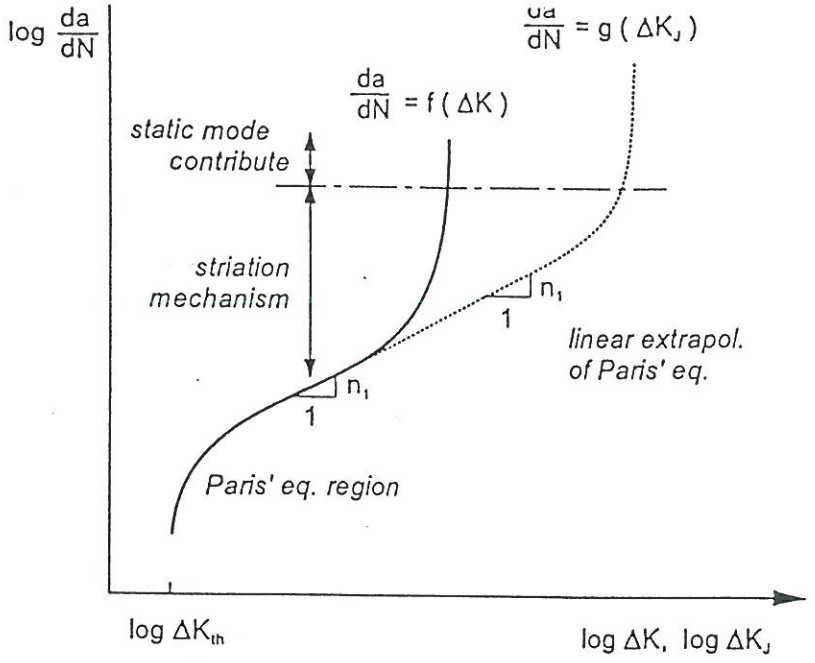

(a)

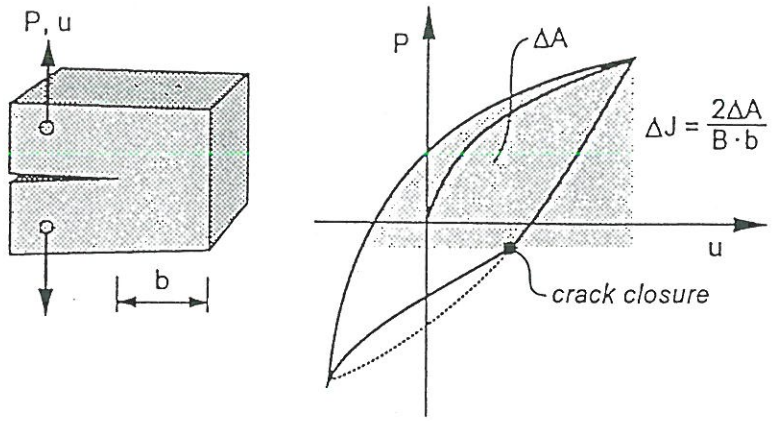

(b)

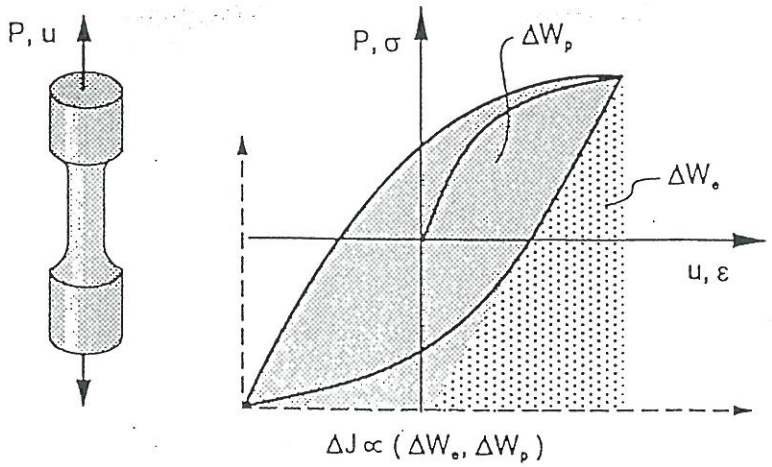

(c)

Figure 2: Crack growth rate behaviour and ΔJ determination with/without sigificant crack closure

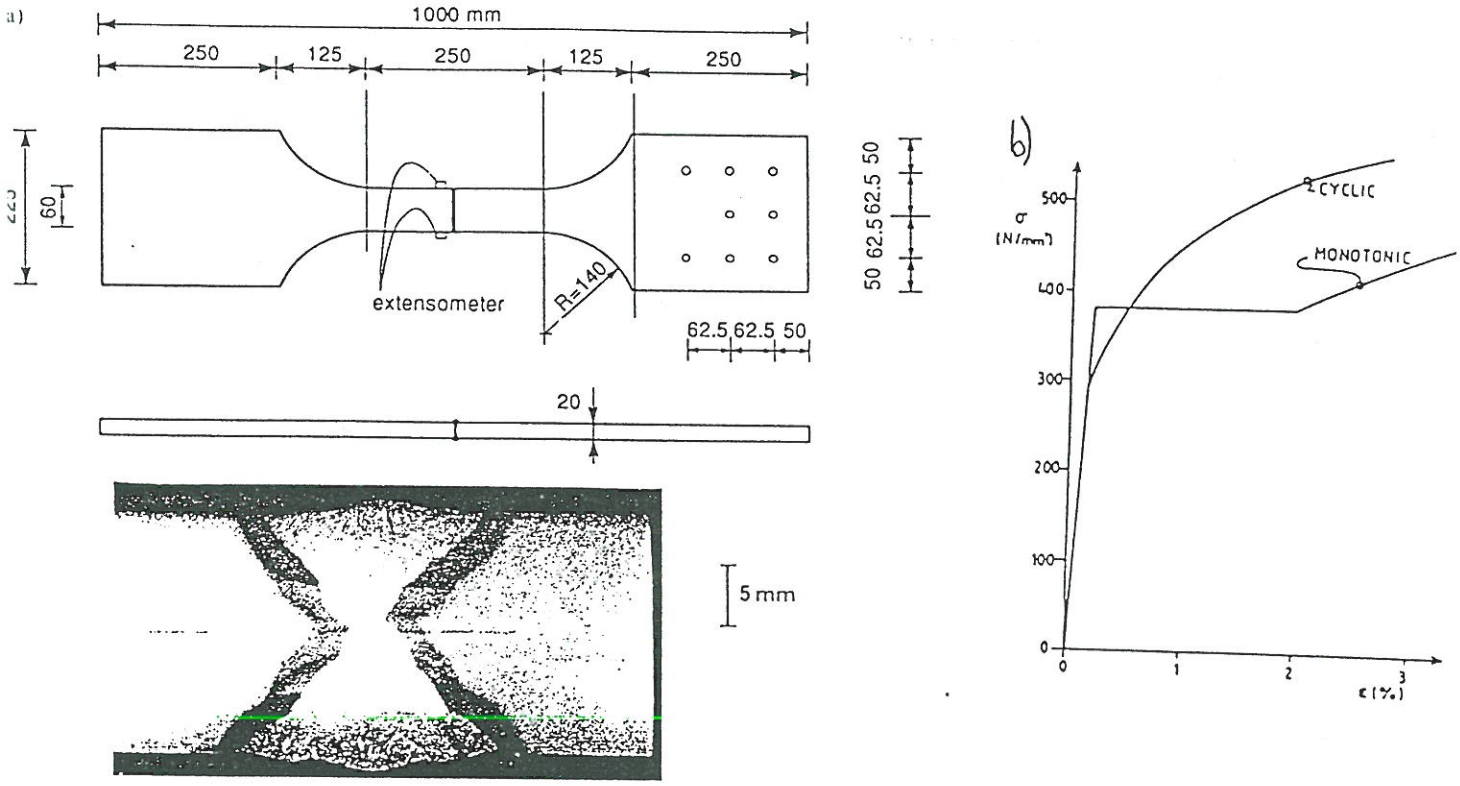

Figure 3: a) Test specimen and buttweld geometry, b) monotonic and cyclic stress-strain curve

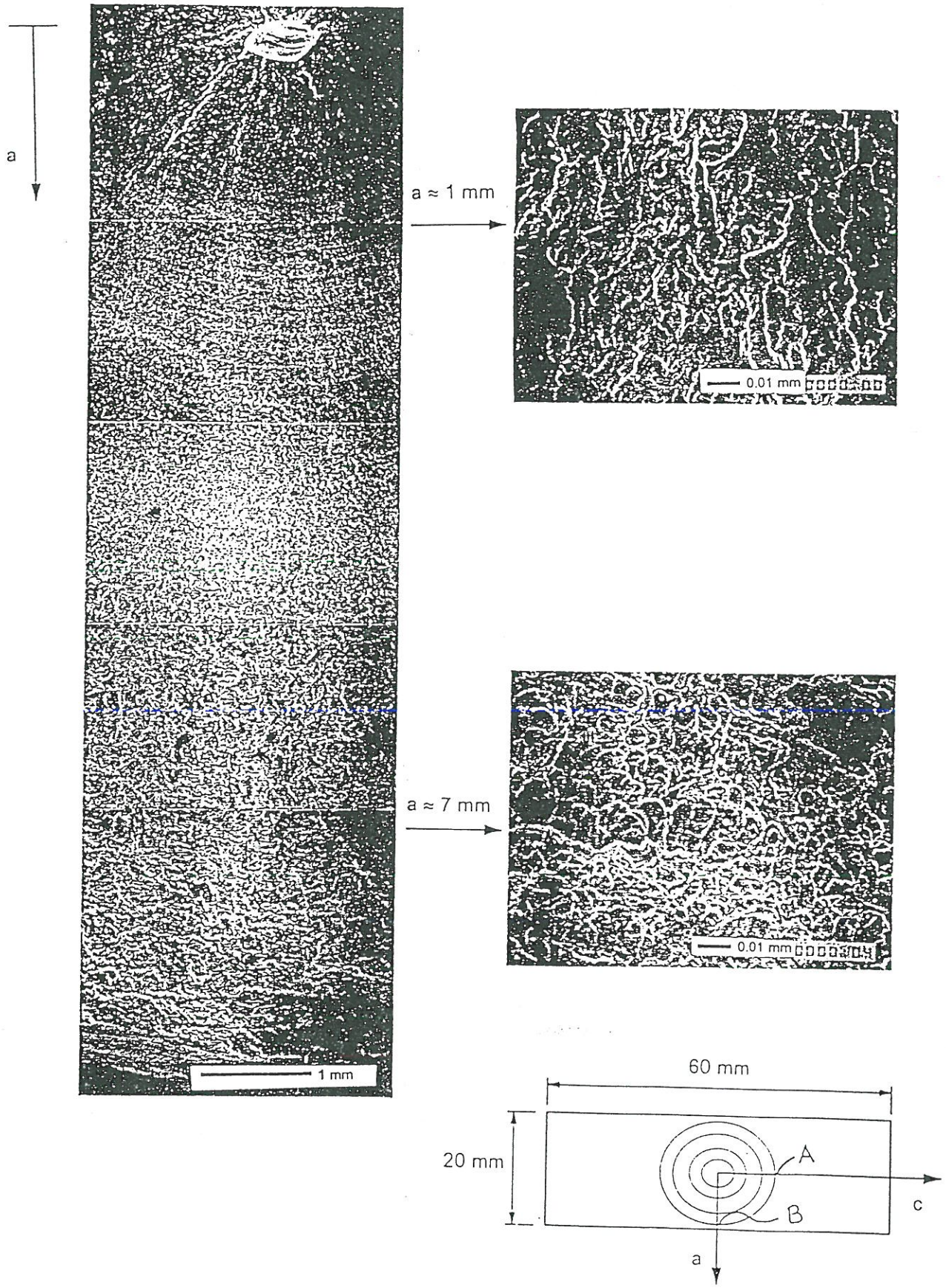

Figure 4: Striation pattern and crack surface details.

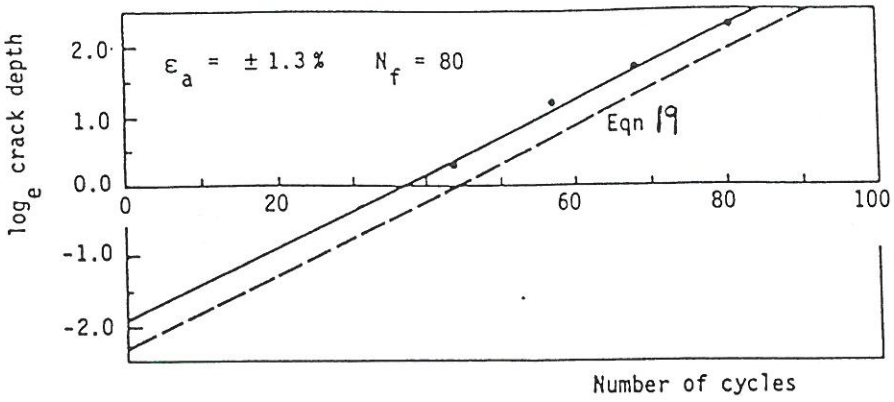

Figure 5: Crack depth versus number of cycles

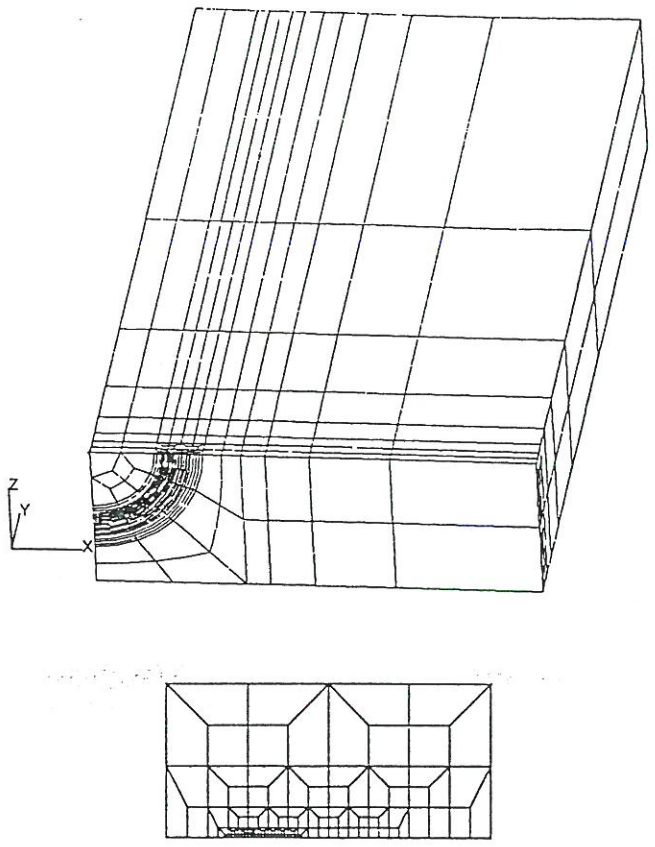

Figure 6: FE mesh for a=5mm, 1/8 of specimen

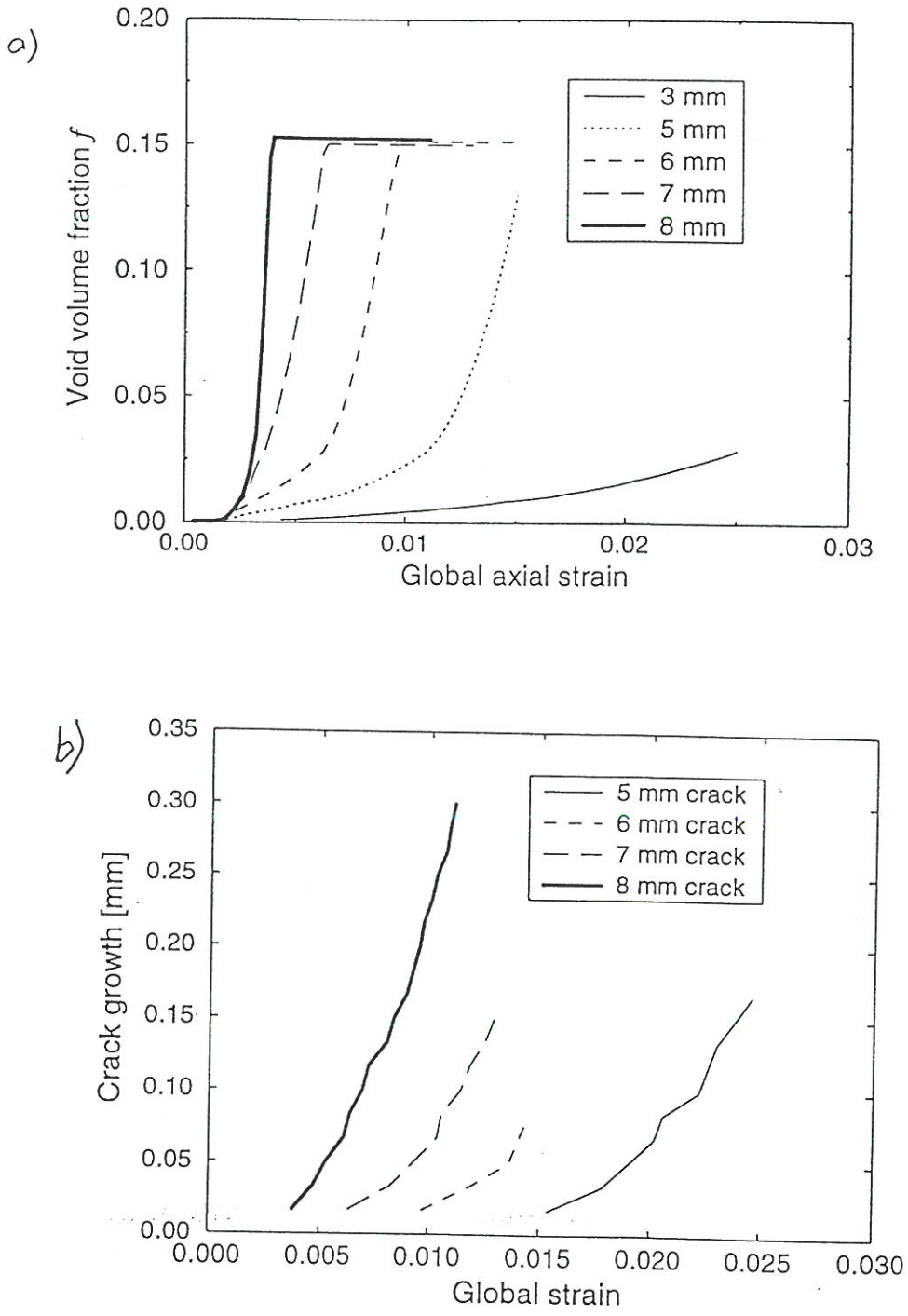

Figure 7: a) Evolution of void volume fraction in near tip integration point (location A) for a=3,5,6,7,8mm, b) ductile tearing crack growth for location A.

a)

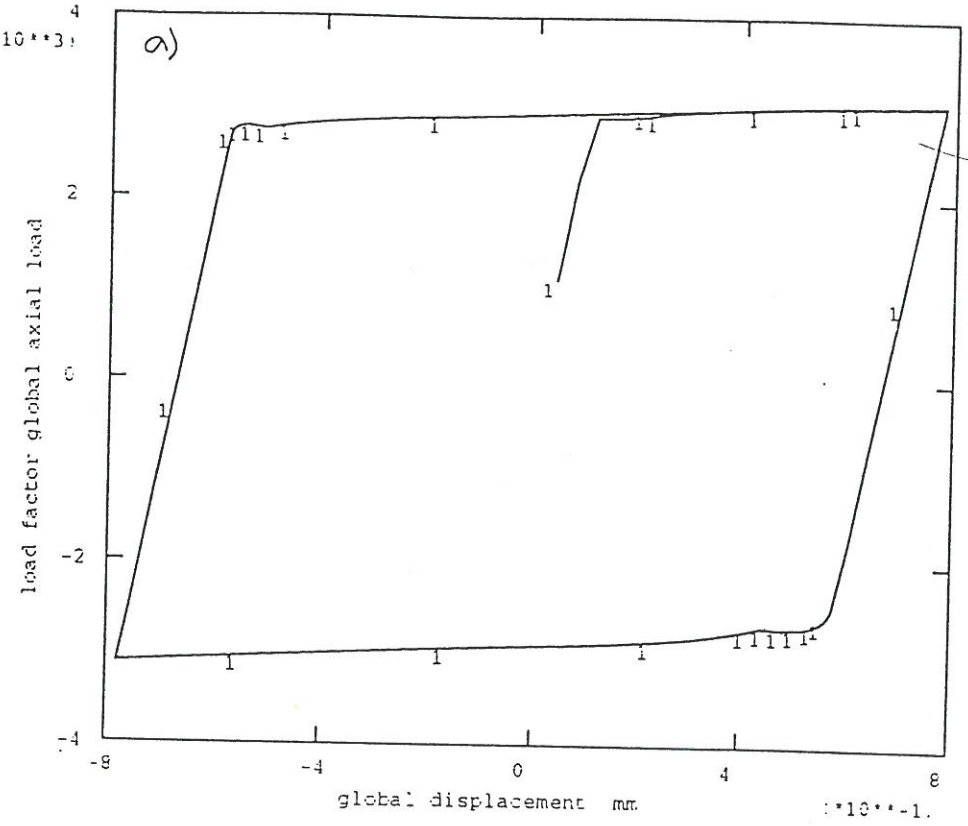

b)

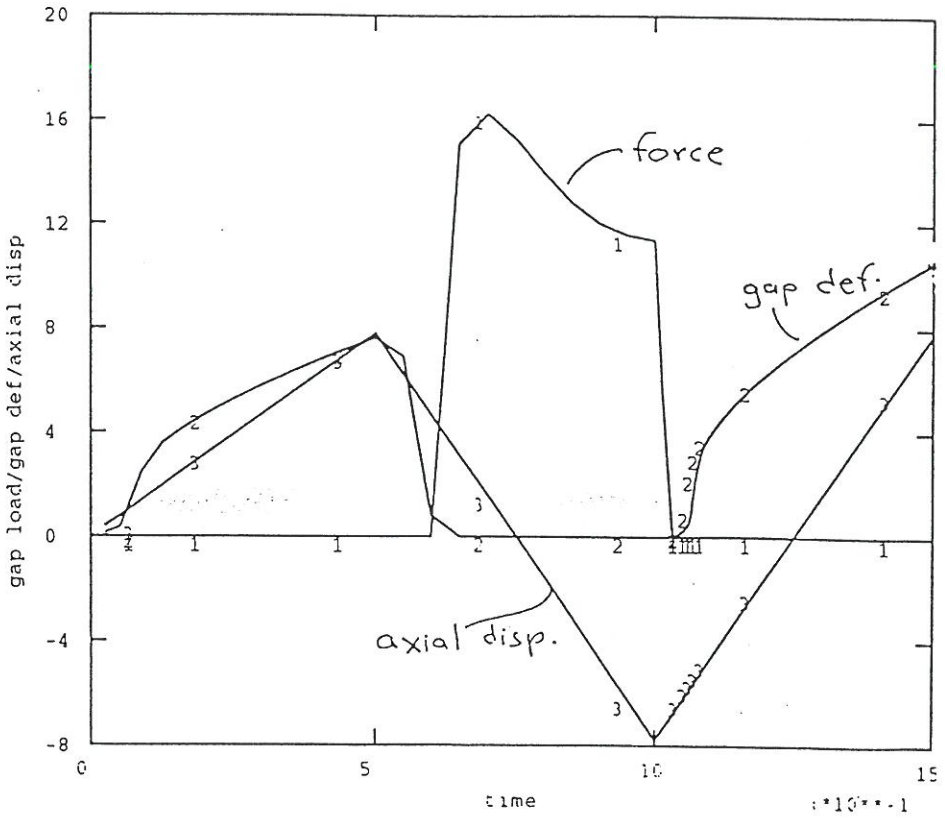

Figure 8: a) Load versus displacement behaviour for a=5mm, b) gap element behaviour near tip element at location A

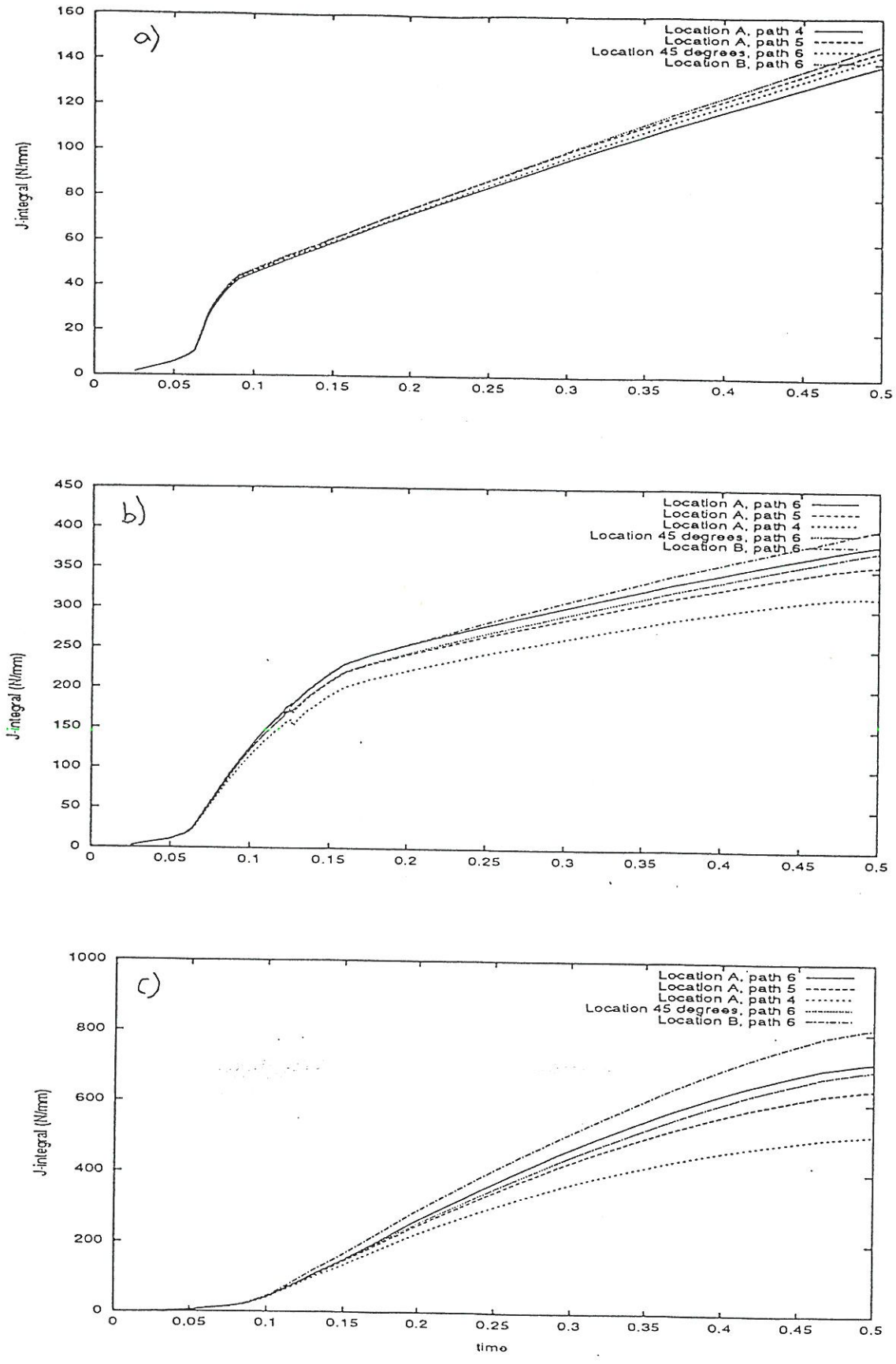

Figure 9: J-evolution for a=3,5,7mm.

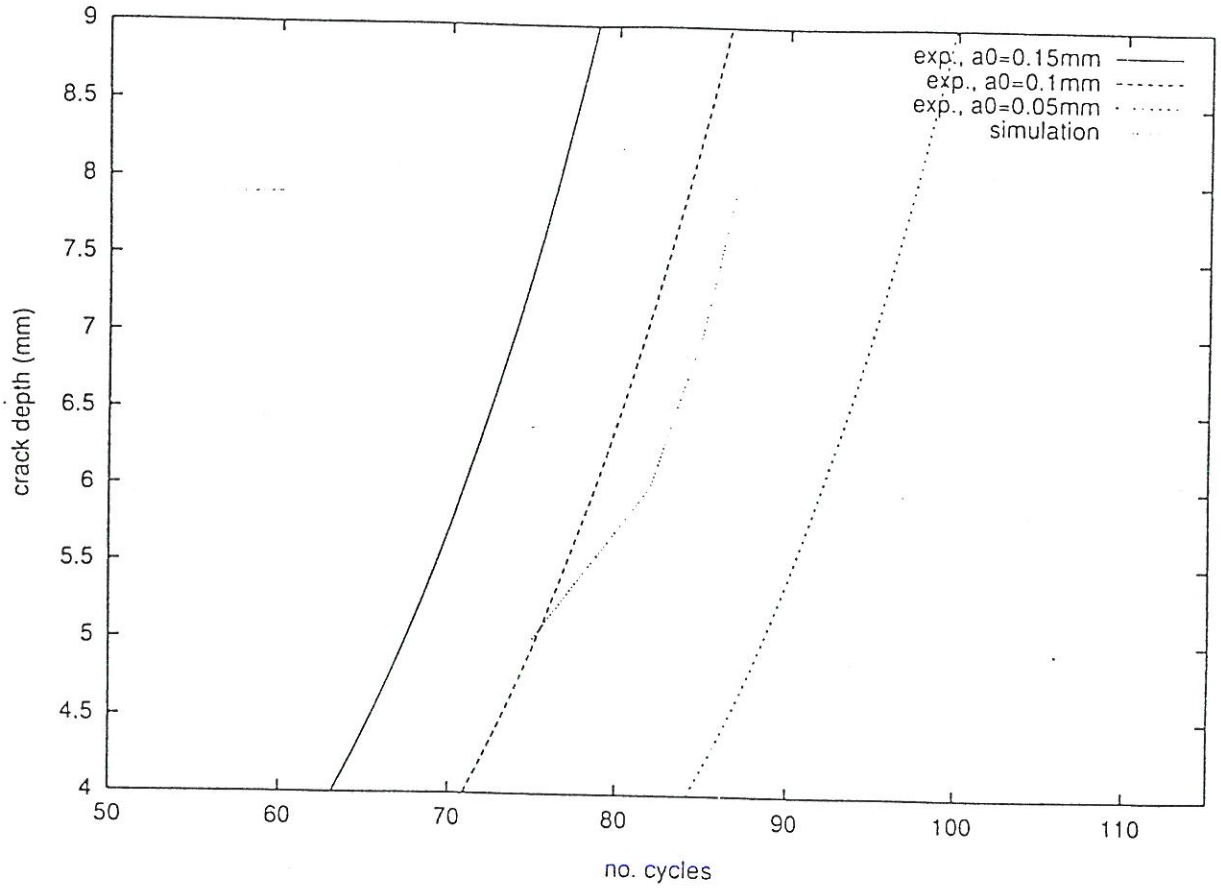

Figure 10: Crack depth versus number of cycles in last part of fatigue life, simulation and test.

Rotational Kinematic Hardening Model for Sand

by

Poul V. Lade
Department of Civil Engineering
The Johns Hopkins University
Baltimore, Maryland 21218, U.S.A.

Modeling the behavior of soils during large stress reversals and large changes in stress involving unloading and reloading is required to capture the behavior of earth structures and soil-structure interaction problems under static as well as dynamic loading conditions. Large stress reversals and stress rotations occur in the ground during most construction projects due to removal and addition of soil and structures. General three-dimensional stress reversals occur during earthquakes and due to fluctuating loads caused by pile driving, wind, waves, and other transient events.

To capture the soil behavior during large stress reversals, a new kinematic hardening model is presented. An existing elasto-plastic model with isotropic hardening is used as the basic framework to which the rotational kinematic hardening mechanism is added. This involves rotation and intersection of yield surfaces to achieve a more consistent and physically rational fit with experimentally observed behavior in both triaxial and octahedral planes. The proposed yield and plastic potential behavior is shown to be consistent with experimental observations. The existing, isotropic work hardening law is shown to apply to isotropic as well as kinematic behavior of sand. The behavior of the proposed plastic potential is verified by studying the behavior of sand during large stress reversals on the basis of results from an experimental program incorporating conventional triaxial tests. Experiments were performed with various simple and complex stress paths involving large changes in stress during unloading and reloading, and the results are evaluated in terms of directions of plastic strain increment vectors superimposed on the stress space. Predicted plastic strain increment directions are compared with experimental data and it is shown that the proposed model can capture soil behavior with reasonable accuracy within the scatter of test results. The capability of the proposed model is examined by comparing predictions with experimental data for simple and complex stress paths involving large stress reversals in the triaxial plane. Comparisons show that the proposed model can capture the behavior of sand during large stress reversals in the triaxial plane with reasonable accuracy.

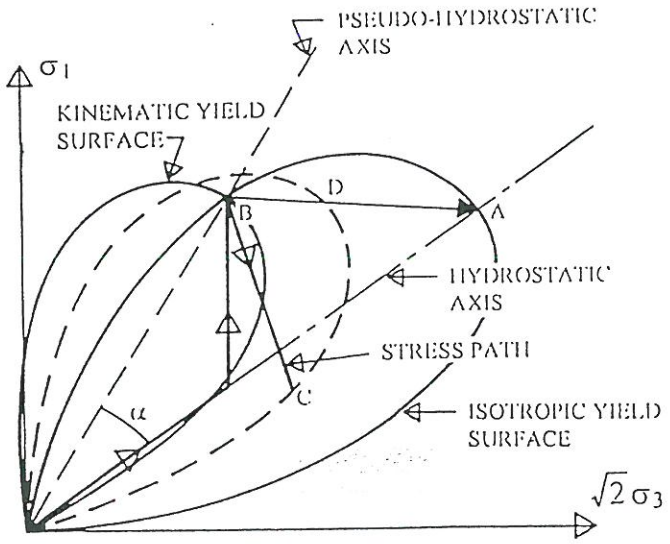

Active Vibration Control of a Monopile Offshore Structure

S.R.K. Nielsen & P.H. Kirkegaard
Aalborg University
Department of Building Technology and Structural Engineering
Sohngaardsholmsvej 57
DK-9000 Aalborg, Denmark

&

Leo Thesbjerg
Rambøll A/S , Esbjerg

Abstract

In the Danish part of the North Sea it has been found that marginal fields can be exploited using monopile offshore platforms which present significant advantages with respect to the costs involved in fabrication and installation and can therefore tip the economic balance favourably. Monopile platforms have been developed for approximately 35 m water depth and to be remotely operated. However, there has recently been a wish to use the monopile concept on 75 m water depth. Using monopiles in such water depths can imply significantly dynamic problems. Therefore, in order to reduce the vibrations, it can be necessary to use an active or a passive vibration control system. However, for a monopile with severe space problems it can be difficult to locate a passive control system such as e.g. a tuned mass damper. Therefore, in order to active control wave introduced vibrations of a monopile structure an active control technique has been proposed in corporation with the consulting company Rambøll, Esbjerg, Denmark. The proposed control technique is based on the relationship between the position of the separation points of the boundary layer flow and the drag term in the wave force on the cylinder. This concept has been experimentally investigated with a test model in stationary flow tests. The idea is to have a large drag coefficient when the cylinder moves opposite of the wave direction implying a relatively large damping excitation. When the structure moves in the wave direction a small drag coefficient should be obtained in order to have a relatively small excitation on the cylinder. The drag coefficient can be controlled if the separation points of the boundary layers can be controlled. It is proposed to control the separation points by blowing compressed air out of the holes in the cylinder. If the natural separation points of the boundary layers are rejected by blowing air out of the holes the drag coefficient will increase while it will decrease if it is possible to attach the boundary layer. The results from the experimental test have shown that it is possible to increase the drag coefficient with a factor 1.5-2 by blowing air out of the holes in a cylinder vibrating in a stationary water flow.

1. INTRODUCTION

Many of the oil fields discovered in the North Sea are marginal fields. Furthermore, the layers in which the reservoirs are located may have very small permeability. Consequently, it is very difficult to predict the production rate for these fields. To develop this type of oil fields it is necessary to minimize the initial investments in the field in order to limit the consequences of a production smaller than predicted. This can be accomplished by means of a smaller remotely operated installation with provision for only one or a few wells.
In the Danish part of the North Sea it has been found that marginal fields can be exploited using monopile offshore platforms, see figure 1, which present significant advantages with respect to the costs involved in fabrication and installation and can therefore tip the economic balance favourably.

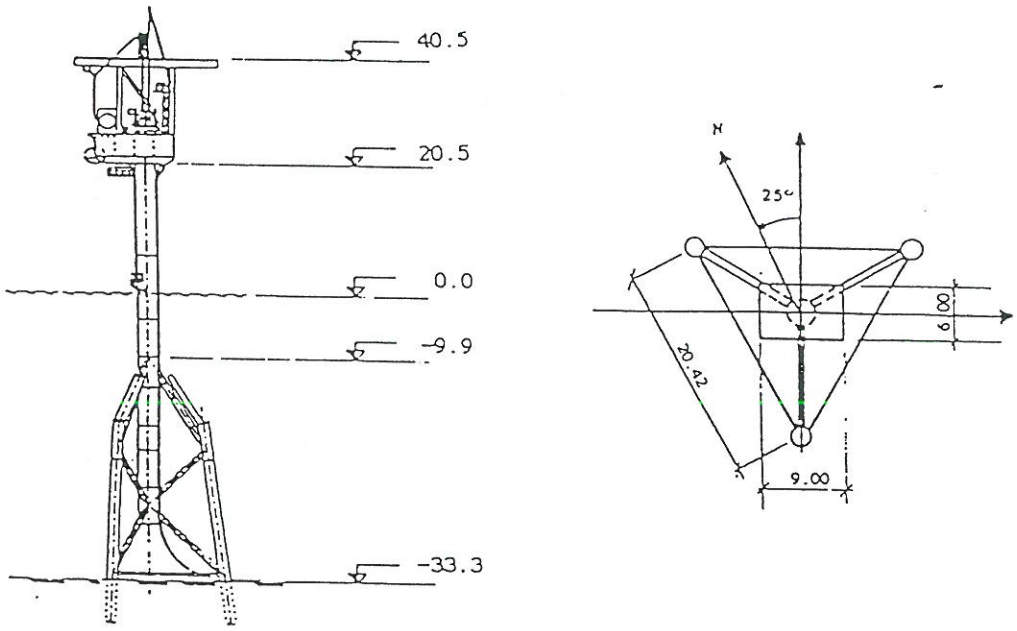

Figure 1: Elevation of a monopile offshore structure used in the Danish part of the North Sea.

The monopile platform shown in figure 1 was developed for approximately 35 m water depth and was remotely operated. This means that in 35 m water depth the free standing structure is governed by its dynamic behaviour and thus prone to fatigue. However, since the structure is remotely operated comfort criteria can be neglected in the design phase. The monopile design has been found not to be governed by the extreme storm load case, but more significantly influenced of fatigue life.
Recently, there has been a wish to use the monopile concept on 75 m water depth. Using monopiles in such water depths can imply significantly dynamic problems. Therefore, in order to reduce the vibrations, it can be necessary to use an active vibration control system. Active vibration control of civil engineering structures can be done using different techniques, see e.g. Soong et al. [1] and Thesbjerg [2]. Active control implies an external excitation in order to obtain a vibration suppression of a structure which is dynamically loaded. Active control is an alternative to passive control which has been seriously considered during the last 50 years.

Passive control implies an arrangement which can reduce the response of the structure. The general subject concerning active control of dynamic systems has been studied longer than active control of civil engineering structures. For many decades, the basic concepts of active control have been the staple of electrical and control engineering and they have been applied successfully in a variety of disciplines, such as aerospace engineering and mechanical engineering.
In order to reduce the vibrations of a monopile structure passive control techniques can be used, e.g. a tuned mass damper, see Soong et al. [1]. However, for a monopile with severe space limitation it can be difficult to locate a tuned mass damper.
In order to active control wave introduced vibration of a monopile structure a control technique has been proposed in corporation with the consulting company Rambøll, Esbjerg, Denmark.
The proposed control technique is based on the relationship between the boundary layer flow and the drag term in the wave force on the structure. It is well known that the wave force consists of a drag term and an inertia term. Normally, the drag term can be estimated using a so-called drag coefficient approximately equal to 0.6 for a cylinder. However, this drag coefficient is a function of the geometry of the structure, but the drag coefficient also depends on the separation points of the boundary layers. This means that the drag coefficient can be controlled if the separation points of the boundary layers can be controlled. One way to control these points could be to perforate the structure and blow air out of the holes. How this concept can be used to reduce the vibrations is explained in the following section.

2. THEORY

This section outlines how the vibrations of a monopile offshore structure can be reduced by controlling the boundary layer separation points. Further, the mathematical model which has been used to experimentally investigate the idea is given.

2.1 Relationship between Vibrations and Wave Force

It is well known that the force on a vertically placed cylinder subjected to wave action consists of a drag f_D as well as an inertia f_I component, see e.g. Sarpkaya et al.[3]. It is generally assumed that the total wave force per unit length of a fixed vertical cylinder of the diameter D is

$$f = f_D + f_I = \frac{1}{2}C_D\rho D|\dot{u} - \dot{v}|(\dot{u} - \dot{v}) + \frac{\pi}{4}C_M\rho D^2\ddot{u} - (C_M-1)\frac{\pi}{4}\rho D^2(\ddot{v}) \qquad (1)$$

where $\dot{u}$ and $\ddot{u}$ and $\dot{v}$ and $\ddot{v}$ are the velocity and the acceleration of the fluid and the structure, respectively. C_D and C_M are the drag and inertia coefficients, respectively. ρ is the density of water.
The idea of the active vibration control system proposed in this research relies on changes in the drag term. Normally, the drag term can be estimated using a drag coefficient approximately equal to 0.6 for a cylinder. However, this drag coefficient is a function of the geometry of the structure, but the drag coefficient also depends on the position of the separation points of the boundary layers. This means that the drag coefficient can be controlled if the position of the separation points of the boundary layers can be controlled. One way to control these points could be to perforate the structure and blow air out of the holes. If the boundary layers are forced to separate

by blowing air out of the holes the drag coefficient will increase. This is the opposite of the well-known principle that the drag force can be reduced by suction.The idea is now to have a large drag coefficient when the cylinder moves opposite of the wave direction, see figure 2a, implying a relatively large damping excitation. When the structure moves in the wave direction a small drag coefficient should be obtained in order to have a relatively small excitation on the cylinder, see figure 2b.

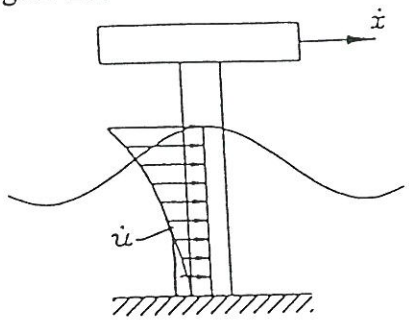

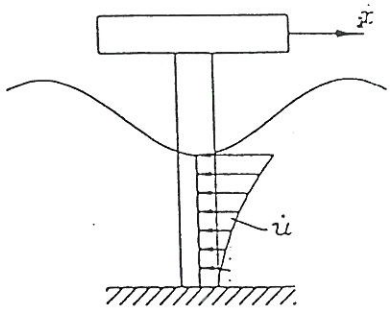

Figure 2a:Wave velocity u and cylinder velocity in opposite direction

2b: Wave velocity and cylinder velocity in same direction

2.2 Mathematical Model

The following model was proposed to be used in an experimental investigation of the change in drag coefficient as a function of air blown out of the holes in a cylinder vibrating in a stationary flow.

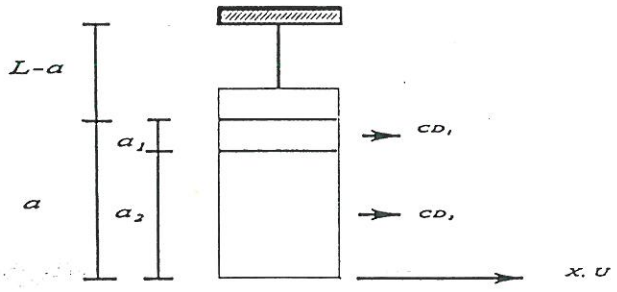

Figure 3: Definition of parameters in mathematical model of a monopile offshore structure

A test model consisting of a steel cylinder has been made as explained in section 3. This model is tested in a stationary flow with the velocity $\dot{U}$. L and a are the distances from the bottom of the cylinder to the beam where the model is attached and water level, respectively. The cylinder is perforated from water level and to $a_1$under water level. It is assumed that the force on the structure now can be estimated using two drag coefficients. C_{D_1} is the drag coefficient or the area where the cylinder is perforated and C_{D_2} is the drag coefficient or the area where the cylinder is

not perforated.The model is assumed to be described using one degree-of-freedom which is selected as the displacement x of the cylinder bottom. The eigenmode is a linearly variating function, so $v(z,t) \approx x(t)z/L$ where z is a vertical coordinate.This means that the governing differential equation for the model in figure 3 can be written in the following way using (1) with $\dot{u}(z,t)=\dot{U}(t)$ and $\ddot{u}(z,t)=\ddot{U}(t)$, i.e the flow is independent of z

$$m_s(\ddot{x} + 2\zeta_0\omega_0\dot{x} + \omega_0^2 x) =$$
$$C_{D_1}\frac{1}{2}\rho DLf_0\left(1-\frac{a}{L},1-\frac{a_2}{L},\dot{U},\dot{x}\right) + C_{D_2}\frac{1}{2}\rho DLf_0\left(1-\frac{a_2}{L},1,\dot{U},\dot{x}\right) - m_h\ddot{x} + m_1\ddot{U} \quad (2)$$

where ω_0 and ζ_0 are the frequency and damping ratio of the system, respectively. The structural mass m_s, the modal hydrodynamic mass m_h and the induced mass m_1,respectively are given by

$$m_s = \int_0^L \mu(z)\left(\frac{z}{L}\right)^2 dz \quad , \quad m_h = \frac{\pi}{4}(C_M-1)\rho D^2\int_{L-a}^{L}\left(\frac{z}{L}\right)^2 dz \quad , \quad m_1 = \frac{\pi}{4}C_M\rho D^2\int_{L-a}^{L}\left(\frac{z}{L}\right)dz \quad (3)$$

The function$f_0(\alpha,\beta,\dot{U},\dot{x})$ is given by

$$f_0(\alpha,\beta,\dot{U},\dot{x}) = \int_\alpha^\beta \xi|\dot{U}-\dot{x}\xi|(\dot{U}-\dot{x}\xi)d\xi \quad (4)$$

which can be analytically calculated as (where $\eta = \frac{\dot{x}}{\dot{U}}$)

$$f_0(\alpha,\beta,\dot{U},\dot{x}) = \frac{\dot{U}|\dot{U}|}{12}\begin{cases} 6(\beta^2-\alpha^2)-8(\beta^3-\alpha^3)\eta+3(\beta^4-\alpha^4)\eta^2 & , \ \infty < \eta \le \frac{1}{\beta} \\ \frac{2}{\eta^2}-6(\beta^2+\alpha^2)+8(\beta^3+\alpha^3)\eta-3(\beta^4+\alpha^4)\eta^2, & \frac{1}{\beta} < \eta \le \frac{1}{\alpha} \\ -6(\beta^2-\alpha^2)+8(\beta^3-\alpha^3)\eta-3(\beta^4-\alpha^4)\eta^2 & , \ \frac{1}{\alpha} < \eta \le \infty \end{cases} \quad (5)$$

$$f_0(\alpha,\beta,0,\dot{x}) = -\frac{1}{4}(\beta^4-\alpha^4)\dot{x}|\dot{x}| \quad (6)$$

3. DESCRIPTION OF TEST MODEL AND INSTRUMENTATION

The model presented in figure 3 was produced and instrumentated as described in this section.

3.1 Model used in Experimental Investigations

Figures 4 and 5, respectively, show pictures of the produced test model. The model consists of a 0.5 m high steel cylinder with a diameter at 0.16 m which is closed in the bottom with a steel plate. The cylinder is mounted to a steel beam across the flow channel with a 0.16 m long, 0.03 m width and 0.003 m thick steel plate. The cylinder is 0.2 and 0.24 m from the top of the cylinder perforated with 12 holes with equidistant distance, i.e the cylinder is perforated with 24 holes. Compressed air can be blown out of these holes since each hole is connected with a rubber tubing. It is possible to open and close each rubber tubing with a valve. All the 24 valves are placed on a connection box which is connected to one high-pressure rubber tubing having a manometer and a valve. This implies that it is possible to regulate the pressure of the air submitted to the connection box and to the 24 rubber tubings.

3.2 Instrumentation

The test programme was divided into two parts. The first part without water in the flow channel consisted of static tests to calibrate a strain gauge mounted on the steel plate which connects the steel cylinder to the beam across the flow channel. Further, some free decay tests without water in the flow channel were performed in order to estimate the structural parameters in equation (4).The second part of the test consisted of free decay tests with stationary water flow in the flow channel and different air pressure out of the holes in the cylinder. These tests were used to estimate C_{D_1} and C_{D_2} in (2).The flow was measured using an ultra sonic flow meter.The strain gauge signal and flow signal were both recorded using a data acquisition system based on a personal computer 386-40 MHz with an add-on A/D 16 bit simultaneous DT-2829 data acquisition board.The signal was samples at 135 Hz with a time series length at 30 sec.

3.3 Measurements Conditions

The tests were performed on December 22 and 23, 1995, in a 2-dimensional flow channel in the Hydraulics and Costal Engineering Laboratory at Aalborg University, Sohngaardsholmsvej 57, DK-9000 Aalborg, Denmark. During the tests the water level was changing approximately ± 0.01 m. The water level a was 0.355 m and the distance a_2 from the bottom of cylinder to the lowest holes in the cylinder was 0.238 m. The free decay tests were performed by giving the cylinder, using the hand, a deflection corresponding to approximately the same number of strains each time.

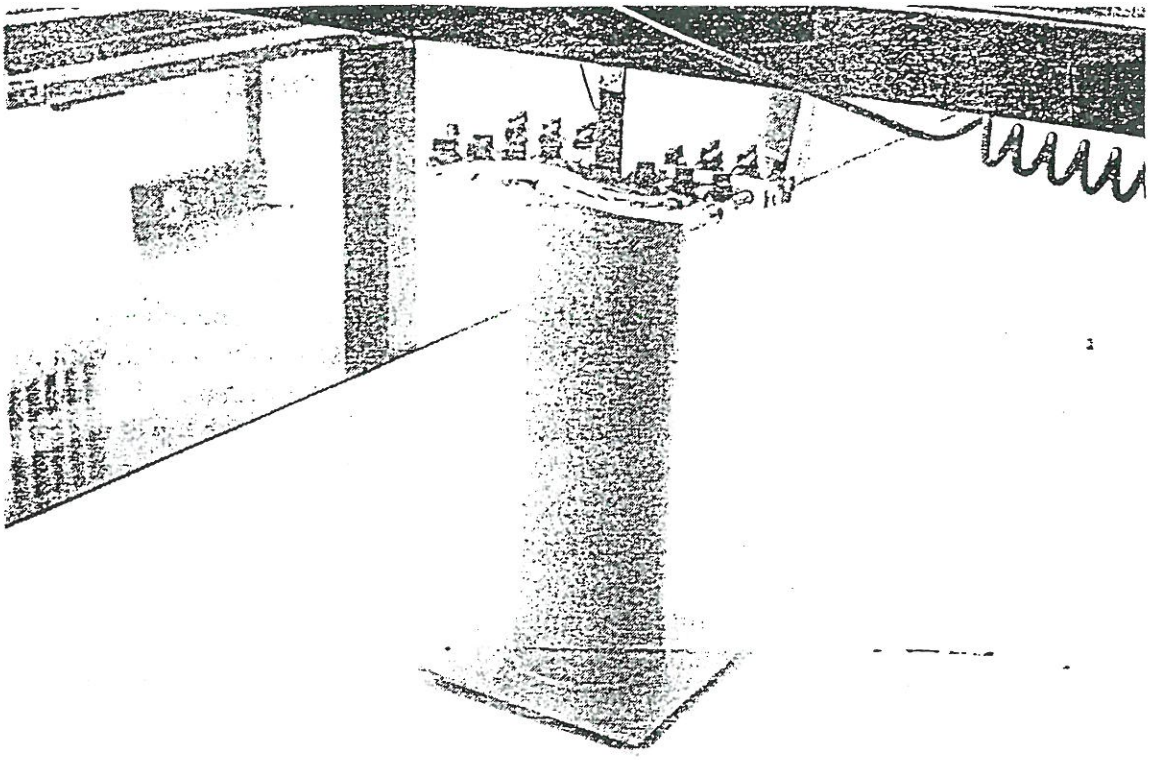

Figure 4. Picture of the monopile test model.

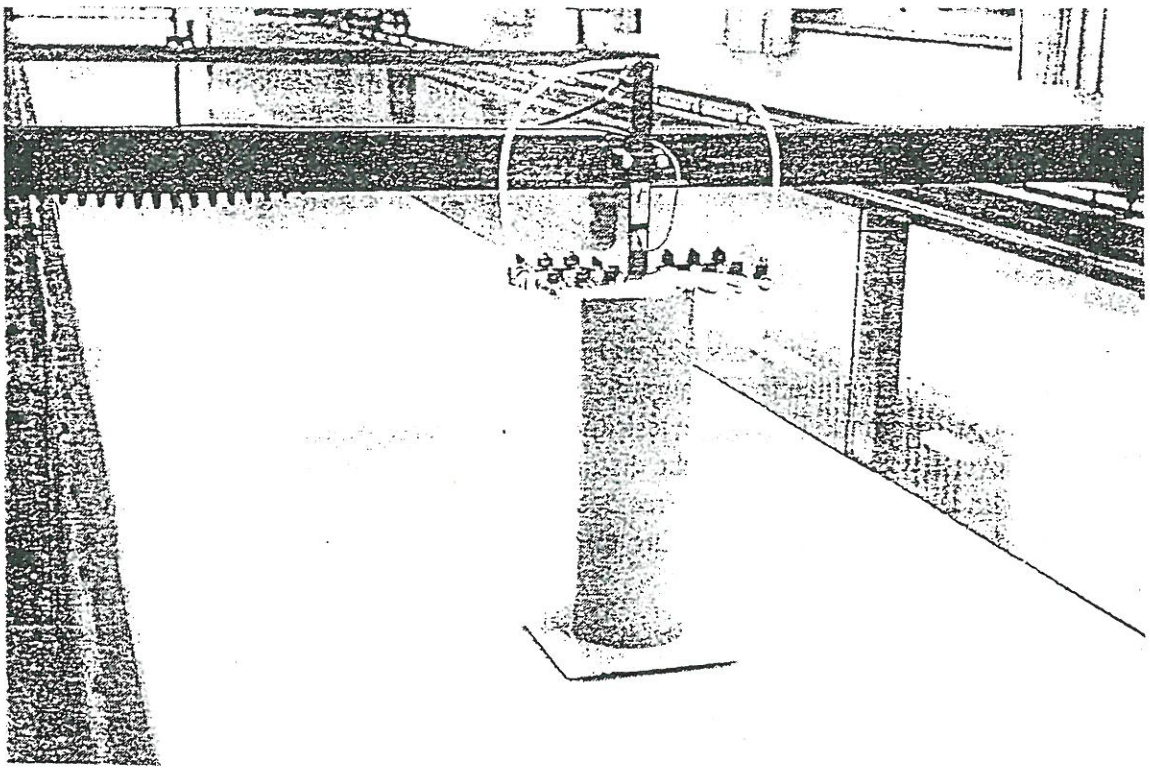

Figure 5. Picture of the monopile test model.

4. RESULTS

In the following section the results will be presented and discussed. Section 4.1 describes the results performed to calibrate the strain gauge and the test model while section 4.2 presents the results from the test used to estimate C_{D_1} and C_{D_2} in (2).

4.1 Estimation of Structural Parameters

In order to find the calibration factor between measured strains S and deflection x of the bottom of the test model and to find the stiffness of the system some static tests were performed. A string combined to a pulley and a plumb bob were connected to the bottom of the cylinder in the longitudinal direction of the flow channel. The results from a test where the weight of the plum bob was $P1$ were repeated five times and are shown in table 1

$P1$ (g)	x (mm)	S ($\mu\epsilon$)
0	0.00	-5
294.5	7.05	254
294.5 +294.7	14.28	502
0	0.11	0
294.5	7.01	247
294.5 +294.7	11.31	496
0	0.31	2
294.5	6.99	248
294.5 +294.7	14.24	496
0	0.22	-3
294.5	6.98	250
294.5 +294.7	14.33	501
0	0.01	-3
294.5	7.11	248
294.5 +294.7	14.35	495

Table 1: Static tests to calibration of strain gauge and estimation of stiffness.

From table 1 estimates of the calibration factor between strain and displacement are found. Further, the stiffness of the system is estimated. Next, 10 free decay tests without water in the flow channel and 8 tests with water in the flow channel were performed. These tests were performed in order to estimate the natural frequencies f_0 and f_1 of the system, respectively. The detrended time series were analysed using an Auto-Regressive model of order 6, see e.g. Pandit [4]. From the mean values of the natural frequencies results from tests without water flow in the channel the generalised mass was estimated as

$$m_s = \frac{k}{(2\pi f_0)^2} = 7.46 \ kg \tag{7}$$

From (7) and the mean value of the natural frequencies results from tests with water flow in the channel the modal hydrodynamic mass m_h can now be estimated from the following relation as

$$m_h = k\left(\frac{1}{(2\pi f_1)^2} - \frac{1}{(2\pi f_0)^2}\right) = 7.96 \ kg \tag{8}$$

4.2 Estimation of CD_1 and CD_2

With the parameters estimated in section 4.2 the only unknowns in equation (2) are the drag coefficients C_{D_1} and C_{D_2} . Since the tests are performed in stationary flow the last term in equation (2) is equal to zero. In order to estimate the drag coefficients C_{D_1} and C_{D_2} the Extendend Kalman Filtering technique was used, see e.g. Ljung [5] and Söderström [6].It was decided to test the model blowing air with pressure p = {0, 0.5, 1.0, 1.5, 2.5 , 5.0} bar out of the holes in the cylinder. Further, the tests were performed with some of the valves closed. Four different layout valve positions were selected. One layout with all valves opened, another with only 5 valves opened in each side of the cylinder and at last two layouts where the valves were open upstream and downstream, respectively. The relative changes of the drag coefficient estimates $C_{D_1}^i$ are shown in figures 5 and 6, respectively, for the two different water flows. It is seen from these figures that a significant change of the drag coefficient can be obtained when air is blown out of the holes in the cylinder.

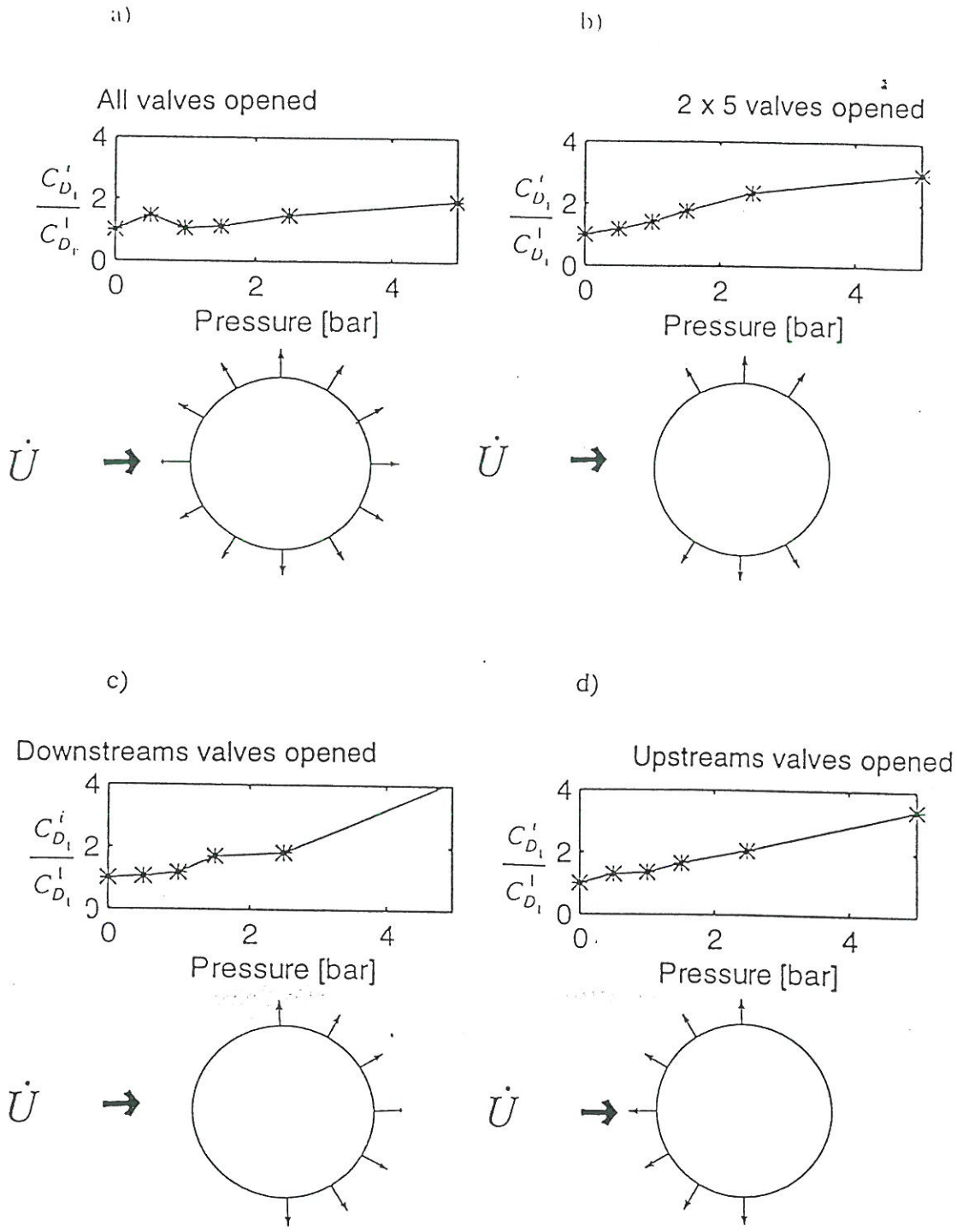

Figure 3: Relative changes in drag coefficients as a function of air pressure. a) All valves opened. b) 2 x 5 valves opened. c) Downstream valves opened. d) Upstream valves opened. ($\dot{U}$≈0.1 *m/s*)

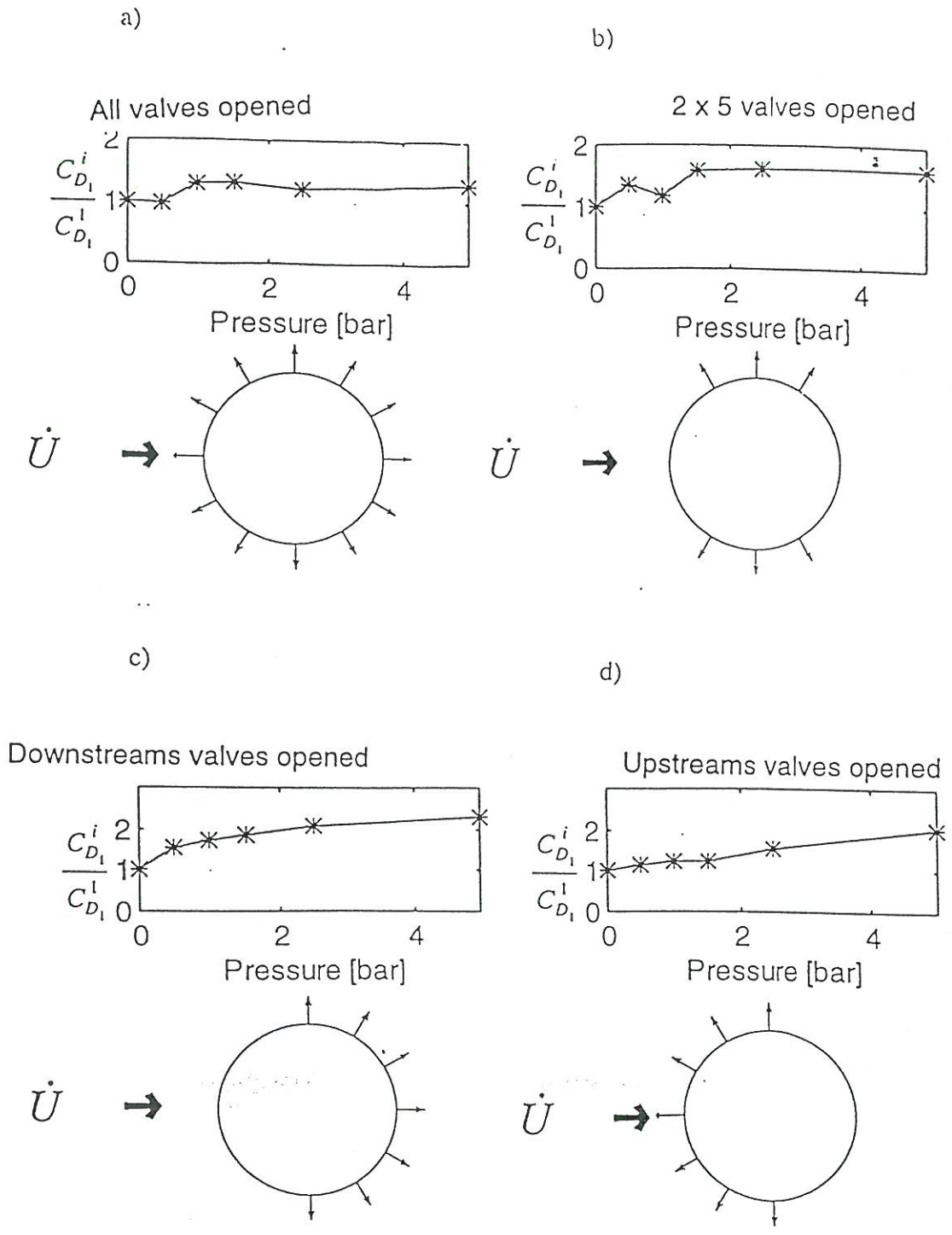

Figure 4: Relative changes in drag coefficients as a function of air pressure. a) All valves opened. b) 2 x 5 valves opened. c) Downstream valves opened. d) Upstream valves opened. ($\dot{U} \approx 0.2$ *m/s*)

5. CONCLUSIONS

The results presented in the present report *Active Vibration Control of a Monopile Offshore Structure - Part One* show that it is possible to increase the drag coefficient with a factor 1.5-2 by blowing air out of the holes in a cylinder vibrating in a stationary water flow. This means that the proposed control technique based on the relationship between the position of the separation points of the boundary layer flow and the drag term in the wave force on the cylinder should be expected to work. However, before a final conclusion can be done, the test model should be tested in nonstationary water flow, i.e. in a test facility where it is possible to excite the model using waves. This will be the subject for research in the future.

6. ACKNOWLEDGEMENTS

The present research was partially supported by The Danish Technical Research Council within the project: "Dynamics of Structures".

7. REFERENCES

[1] Soong, T.T.: Active Vibration Control in Civil Engineering. State-of-the-Art, Eng. Structural, Vol.10, 1988.

[2] Thesbjerg, L: Optimal Vibration Control of Civil Engineering Structures. Ph.D thesis, Structural Reliability Paper No. 93, Aalborg University, 1992

[3] Sarpkaya,T & M. Isaacson: Mechanics of Wave Forces on Offshore Structures. Van Nostrand Reinhold Company, 1981.

[4] Pandit, S.M & S.M. Wu: *Time Series and System Analysis with Applications.* John Wiley and sons, 1983.

[5] Ljung, L.: *System Identification - Theory for the User.* Prentice Hall, Englewood Cliffs, 1987.

[6] Söderström, T. & P. Stoica: *System Identification.* Prentice Hall, 1987.

Active Control of Long Suspension Bridges

Henriette I. Hansen
Aalborg University

Abstract

Along with the apperance of still more sophisticated structural analysis methods there has been a tendency to build more slender and flexible civil engineering structures. In return of these material savings, structures has become highly sensible to vibrations from dynamic loadings. Because this problem has become actual, further material savings will rely on whether the structures can be equipped with damping devices, which reduces the vibration to an acceptable level.

The present abstract deals with the application of a active closed-loop control system for the limitation of vibrations of long suspension bridges. The control system is of the variable geometry type, where the wind flow around the oscillating bridge is controlled by flaps in a way, that the forces from the wind always opposes the velocity of the bridge section.

To investigate the principle to use flaps to control the vibrations of the bridge, wind tunnel experiments are planned with a bridge section model equipped with flaps. The experiments will take place in the wind tunnel for building aerodynamics at the Instituto Superior Technico in Lisbon, Portugal. The cross-section of the testsection is 1.5×1.5 m. and the wind velocity can be regulated in the interval 4–40 $^{m}/_{s}$.

The bridge section model is dimensioned to fit in the wind tunnel, whereby a practical usable model is dimensioned. The model is realistic compared to a real bridge, but no specific bridge is investigated. The bridge section model is designed so the length is 1.48 m and the flutter wind velocity is approximately 10 $^{m}/_{s}$. Characteristics for the 'prototype' and the model are shown below.

	'Prototype'	Model
Width B (excl. flaps) [m]	25	0.625
Mass per unit length m [kg/m]	25000	15.6
First eigenfrequency f_1 (bending) [Hz]	0.08	0.8
Second eigenfrequency f_2 (torsion) [Hz]	0.16	1.6

The bridge section model is made of foam with an aluminium frame. Where it has been possible there are holes in the aluminium frame to reduce the weight.

It is of interest to investigate flaps with different lengths. Therefore, flaps with lengths $0.15\,B$ and $0.25\,B$ are investigated, where B is the width of the model excl. flaps. The flaps can be regulated independently, they are able to rotate approximately 20° from the horizontal positions.

The model is connected to a horizontal extension rod in each side which is going through holes in the wind tunnel walls. The suspension system is the same in both sides. The extension rod is connected to an ams with dummy masses that can be moved on the arm so the model can represent the correct mass inertia. Each side of the arm is suspended in a spring. The suspension system is very flexible as it can be regulated in both horizontal and vertical directions.

The active control system consists of:

1. Sensors to measure the motion of the model. The displacements of the model are measured by using load cells connected to the ends of the springs.
2. Calculation of the optimal flap positions (closed-loop control). The methods used are: optimal control and neural network control.
3. Regulation system to position the flaps in the desired positions. This system consists of two seperate systems as the flaps can be regulated independently. Each system consists of a servo motor, reduction gear and servo amplifier. The systems are controlled by a software regulation program.

Theoretically, it is possible to use the flaps to change the magnitude and the direction of the forces from the wind and thereby increase the flutter wind velocity.

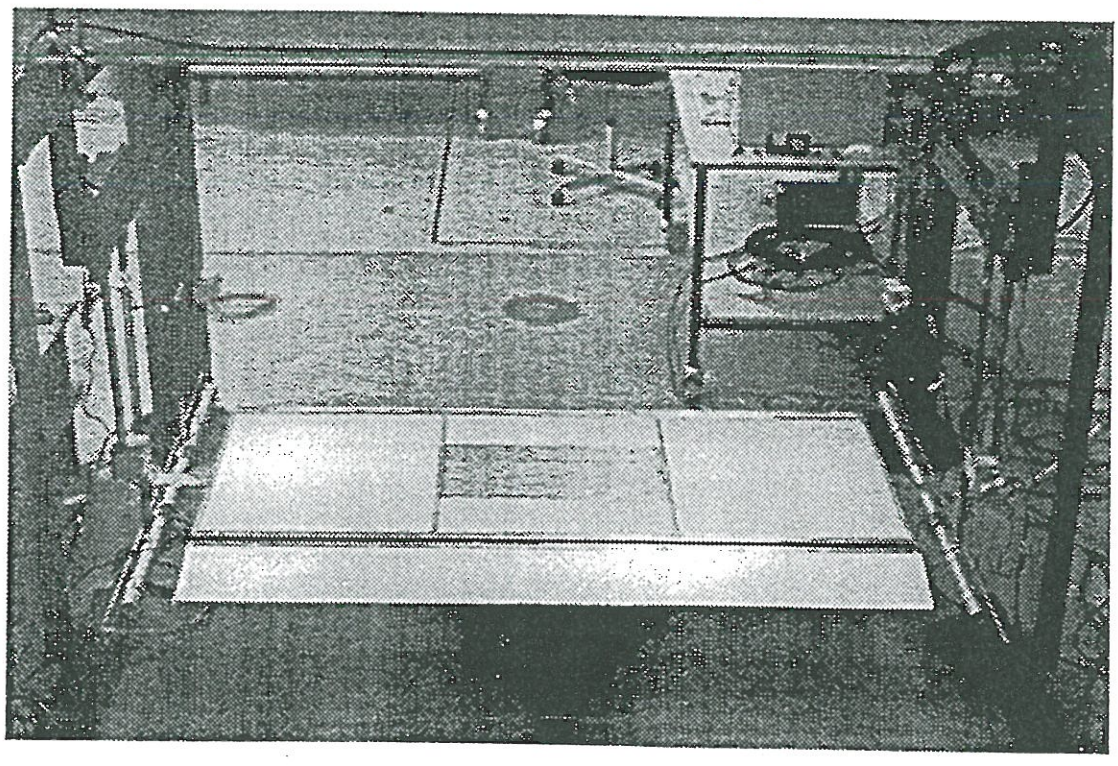

Displacements of Øresund bridge piers from ship impact

Helge Gravesen Morten Faurschou Carl Bro
Civil & Transportation a/s
Chief Consultant Senior Engineer Glostrup, Denmark

Abstract

The present paper describes main results of an analysis of the ship impact to the Øresund bridge piers carried out in connection with the tender for bridge contracts for the Øresund Link. The analysis has included a non-linear foundation analysis and a 2-dimensional displacement calculation. Examples of results for head-on-bow (HOB) collision for piers at approach span group 4 is described. Group 4 includes 3.7 km centrally around the navigation span except from 2 x 2 approach spans closest to the cable stayed bridge.

1. Design requirements and specifications

1.1 Ship impact load

The main design requirements were maximum allowable displacements of pier top and/or pier foundation: 100 mm for pylons and 400 mm for approach span and side span piers for maximum load. Basis for the analysis is idealized load time curves for the design ships given in the design requirements (Fig. 1).

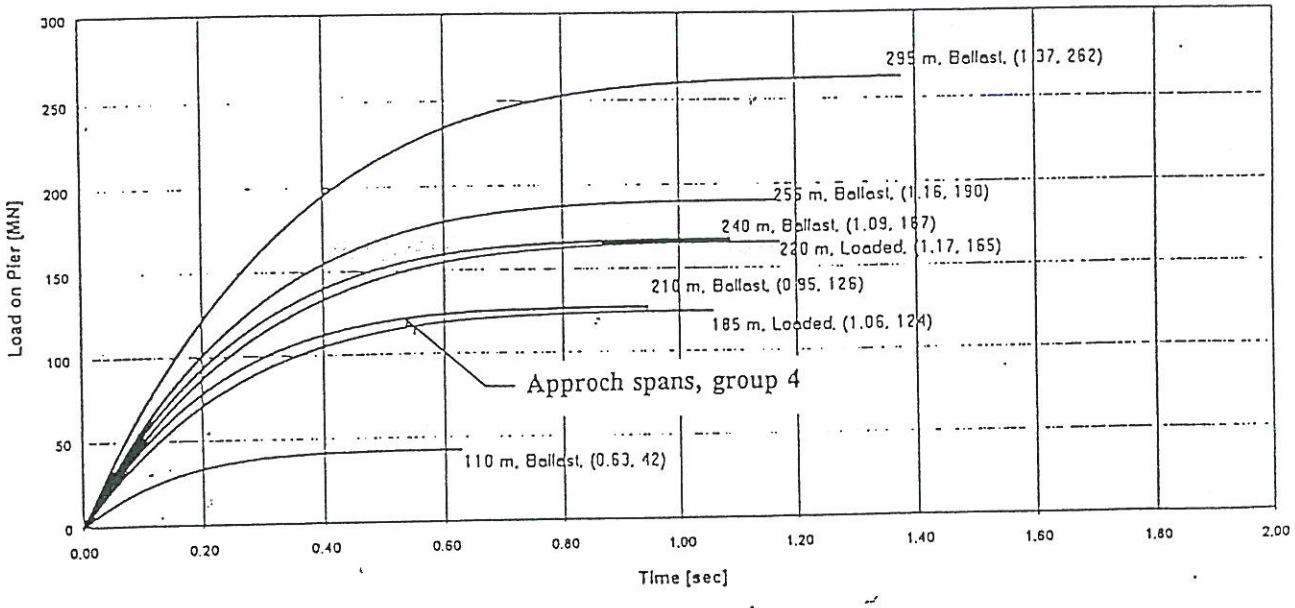

Fig. 1 Length overall, load condition and force versus time for design ship impact

1.2 "Yielding curve" for limestone

The "yielding curve" (rupture) for the limestone was specified in the tender materials.

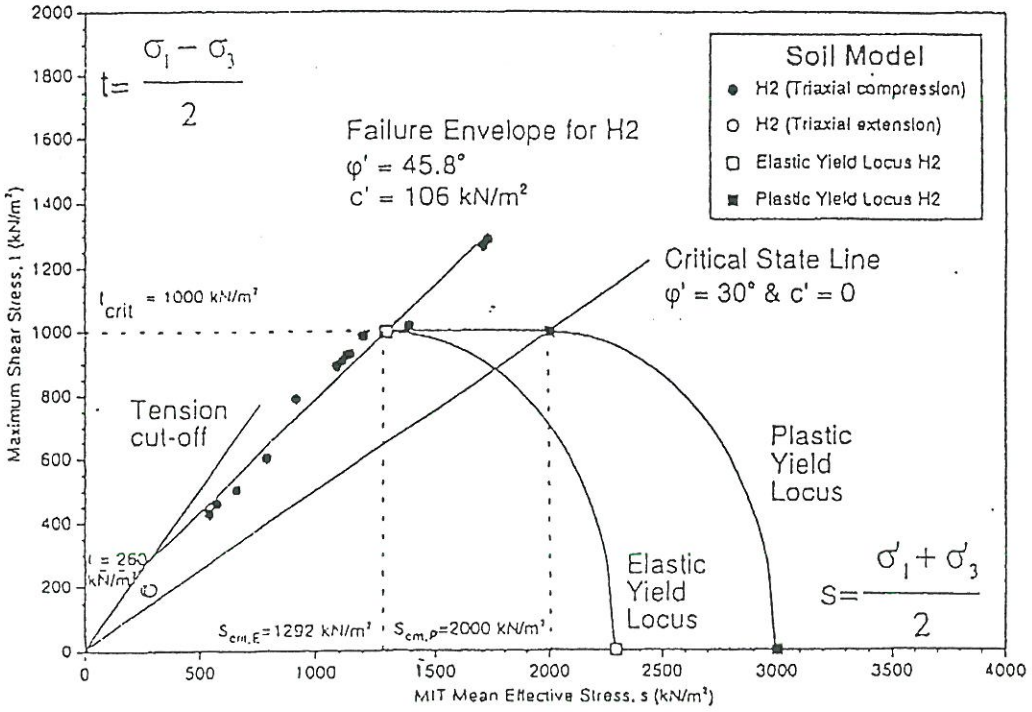

Fig. 2 Yielding curve specified for limestone

2. Principal pier design (group 4 piers)

The distance between the piers were 140 m. The Piers consisted of two parts, the Pier Shafts and the Caissons. The shape of the piers shafts was dictated by the Employer. Structurally it was designed as a prefabricated reinforced concrete cell structure with three cells. Pier Shafts in group 4 were partly filled with sand in order to obtain adequate vertical load for stability during ship impact.

The caissons too were designed as prefabricated reinforced concrete structures. Above sea bed the shape of the caissons were approximately as prescribed for the piers, but with sligthly larger dimensions in order to allow for some placing tolerances of the caissons. The dimensions above sea bed were appr. 7 × 19 m with three longitudinal walls and 6 transverse walls forming 2 x 5 cells. On top of the walls a 1 m plinth formed part of the prefabricated structure.

Below sea bed the cell structure was extended to 4 × 9 cells, with overall dimensions of 29 × 20 m. All side cells of group 4 caissons were covered by a sligthly inclined concrete slab. The excavation around the caissons as well as the inner cells of the caissons were to be filled with a 3 m tremie concrete plug. Above the tremie concrete the cells were filled with sand. A 1 m band of the tremie concrete outside the caissons was included in the effective area of the base.

Fig. 3 below illustrates the preliminary design as described above.

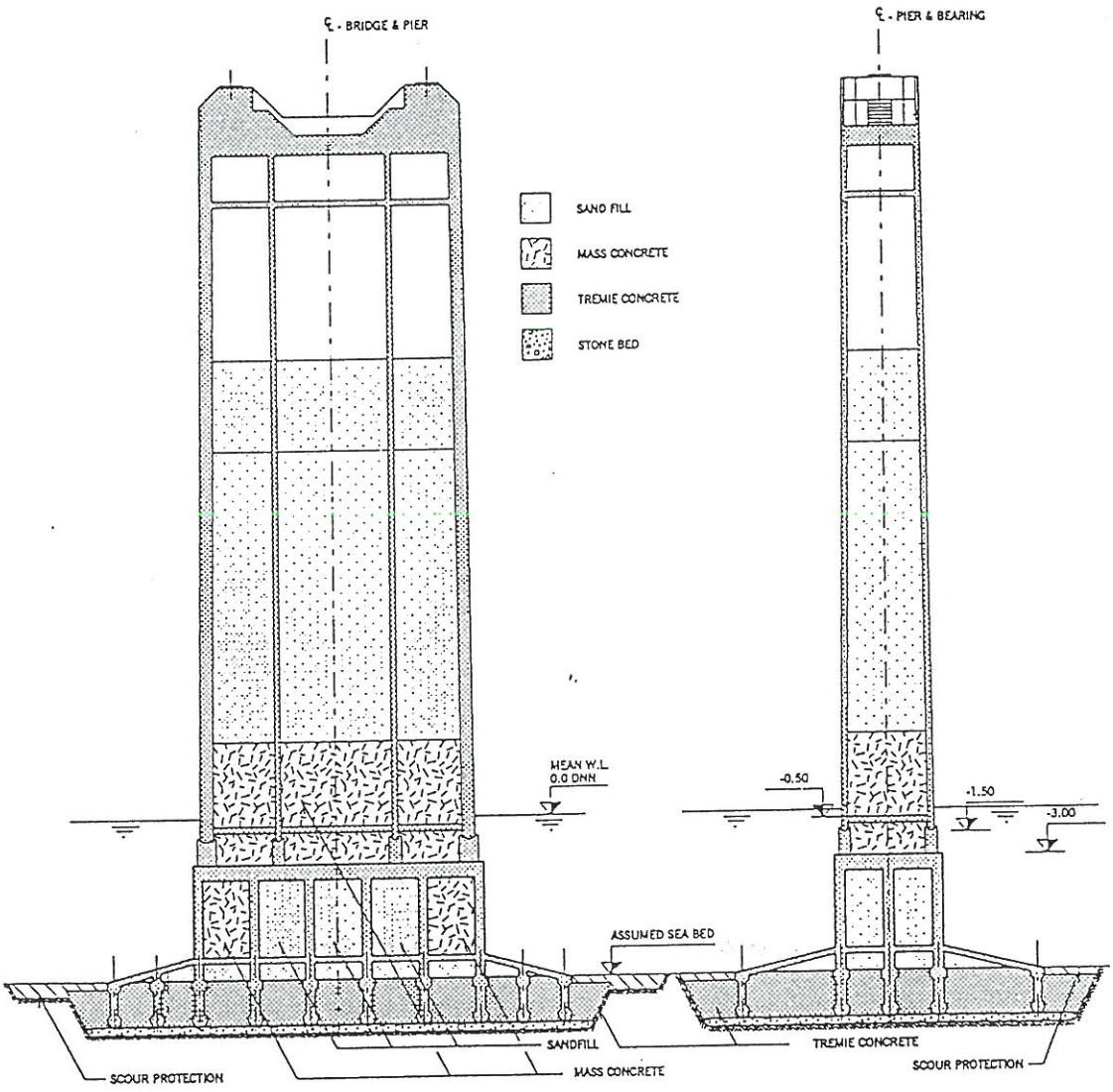

Fig. 3 Preliminary design of bridge pier for approach bridge

3. Non-linear foundation analysis

3.1 Linear Plaxis simulation superimposed by a non-linear analysis

The moment/angle deformation curve for a certain foundation length has been estimated by means of a series of simulations carried out on the soil-structure computer programme Plaxis for various effective foundation lengths (defined as the length to the rotation point), when exposed to a selected unit load. The determined angle deformations are shown in Fig. 4.

Caisson base stiffness			Soil characteristics			
Case	EI 10^3 MNm^2/m	EA 10^3 MN/m	Case	E MPa	G MPa	υ
1 2	8.3 41	3.6 9.0	1 2	500 1,500	192 577	0.3 0.3

Table 1 Basic parameters for the simulations

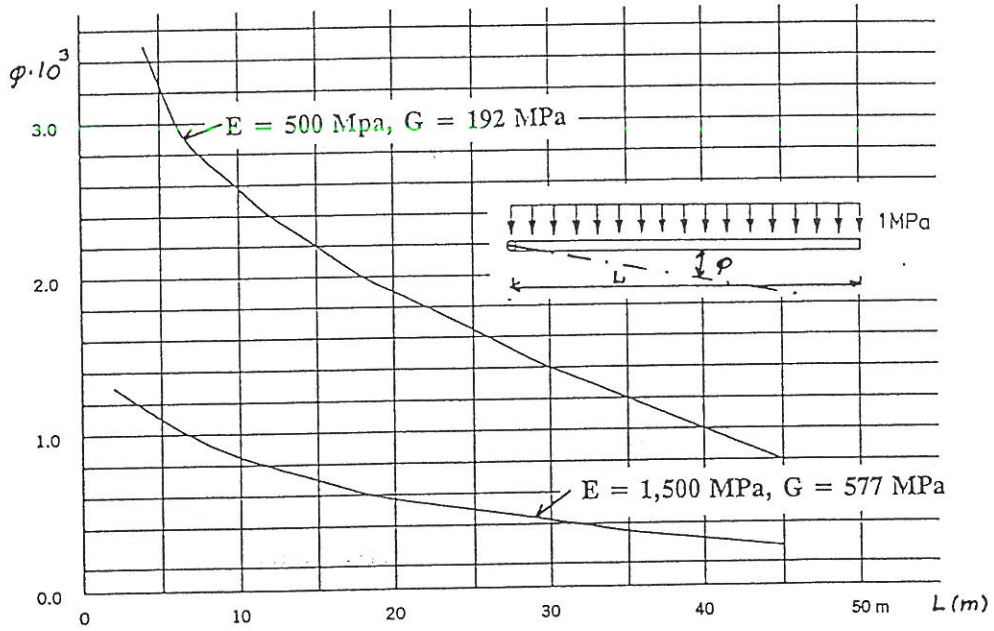

Fig. 4 Pier base rotation for various soil conditions and effective foundation lengths, when exposed to a vertical unit load on the foundation of 1 MPa with a fixed rotation point

The pressure distribution (see Fig. 5) showed two distinct characteristics:

- the vertical pressure was negative or less than zero until typically 2 m from the turning point

- at the boundary with the maximum deformation a relative large boundary stress peak was experienced first been reduced around 1 m outside the foundation

This is the case when the caisson basis is relatively stiff compared to the soil stiffness so limited bending in the caisson basis occurs. So under a stiff caisson basis it was possible to approximate the actual pressure distribution with a standard distribution, which also is shown on Fig. 5.

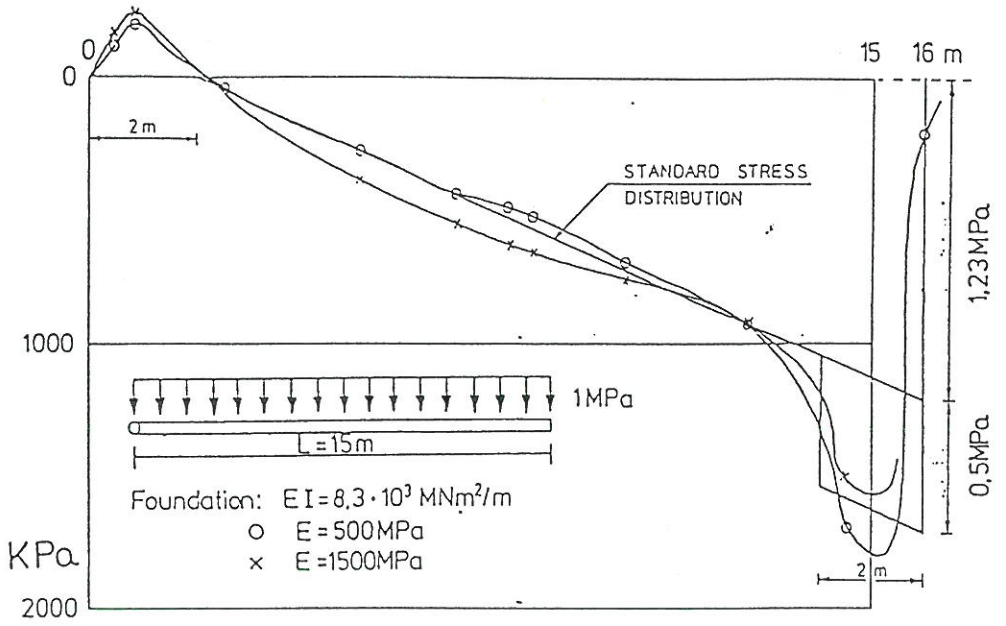

Fig. 5 Examples of stress distributions for a pier foundation exposed to the standard load and the applied approximative standard distribution

The effect of yielding could be included by maintaining the relative ratio between angle deformation and stress in the linear range but limit the vertical stress under the foundation to a certain "yield" value. Fig. 6 show an example of the moment angle deformation curve for a certain vertical load (weight of foundation) with an assumed vertical yield stress of 2 MPa and 1.5 MPa, respectively.

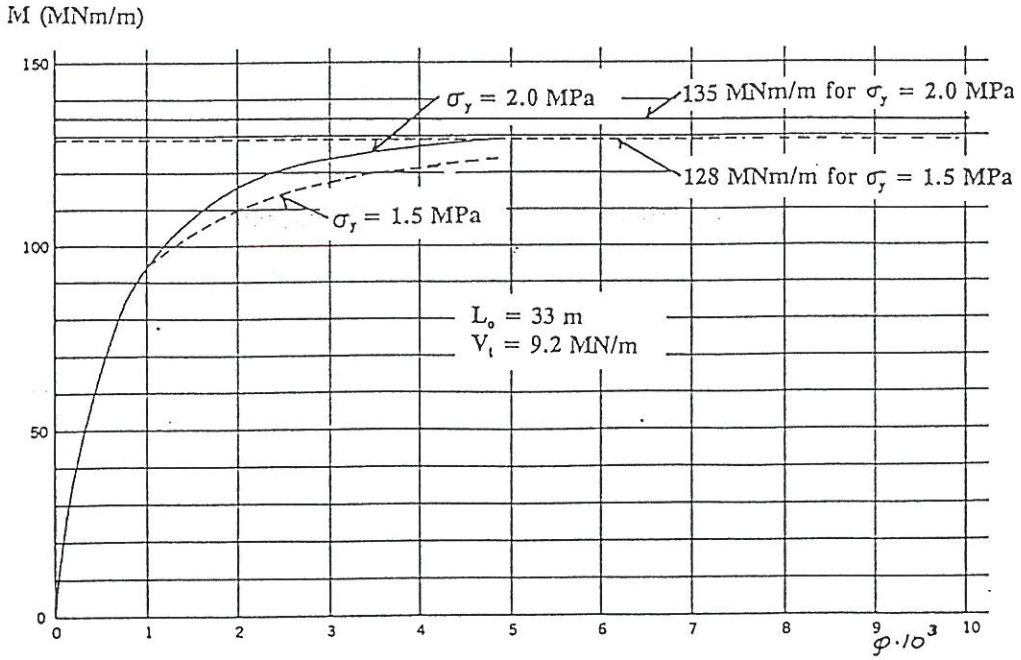

Fig. 6 Example of moment/angular caisson basis deformation curve. Simplified yield criteria 2.0 MPa and 1.5 MPa

3.2 Application of a non-linear Plaxis simulation

A check analysis with a full non-linear Plaxis simulation was performed by Norwegian Geotechnical Institute for a foundation with a length of 33 m (weight 9.2 MN/m, max shear force 4.4 MN/m and moment 132 MNm/m for a soil of E = 500 MPa and a foundation stiffness of EI = 41 x 103 MNm^2/m). The main results are illustrated in Fig. 7. The centre to toe rotation is considered most characteristic in a comparison with the simplified method, so the simplified method results in quite accurate estimate.

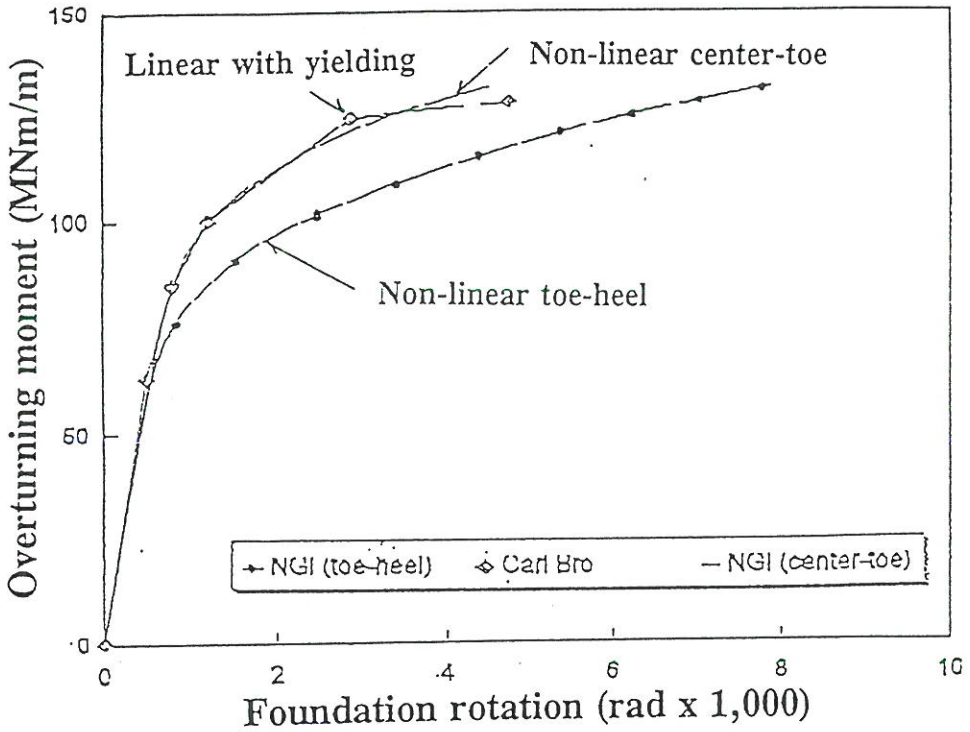

Fig. 7 Moment/angular caisson basis deformation curves from 2-dimensional non-linear analysis and estimates from a linear model superimposed by a simplified yielding assumption

3.3 Examples from Storebælt West Bridge with simplified method

A method based on a simple yield criteria is less accurate than a fully non-linear analysis. On the other hand it maintains a good physical understanding by the direct use of the elastic case and the associated stress distribution.

In cases with less accurate defined yield criteria the estimated ultimate bearing capacity may be directly applied as equivalent vertical yield stress. Then the complete moment/angle deformation curve may be estimated with reasonable accuracy.

This is illustrated in Fig. 8 where a standard case treated in connection with the Storebælt West Bridge is been recalculated applying the above mentioned simplified method. Please note, that the original West Bridge analysis was 3-dimensional applying an elliptical approximation to the reaction from the rectangular caisson basis.

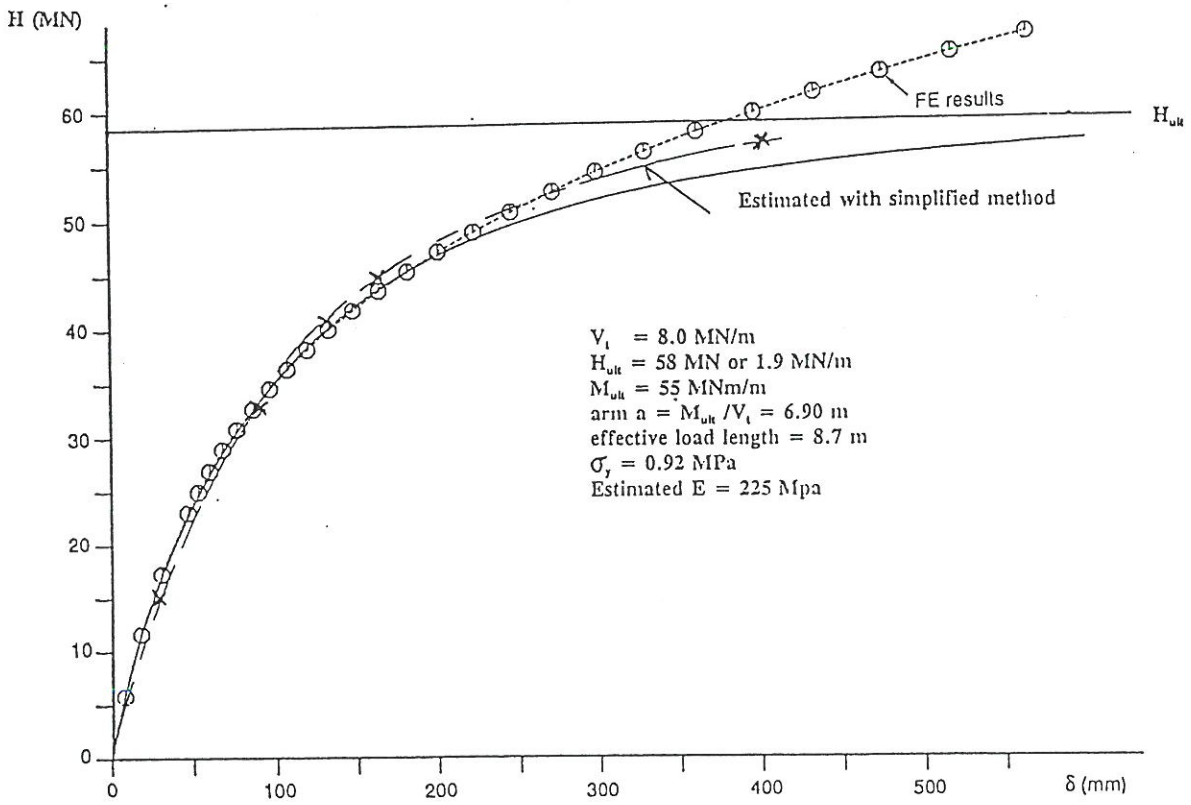

Fig. 8 Reanalysis of the moment/angular caisson basis deformation curves for a selected typical case from the West Bridge in Storebælt

4. Estimates of deformations in piers and girders

The analysis of top of pier deformation was divided in translation (from horizontal force) and rotation (from overturning moment). Due to the relative deep foundation level, typically 5 m below sea bed, it appeared that the largest deformations were induced by the overturning moment. On the basis of known masses/inertia masses (M/ summa M r^2) and estimates of added masses/inertia masses the two non-linear motion equation could be solved in a calculation sheet. Fig. 9 shows the result of the overturning moment/rotation analysis and Fig. 10 shows the total top of pier displacement.

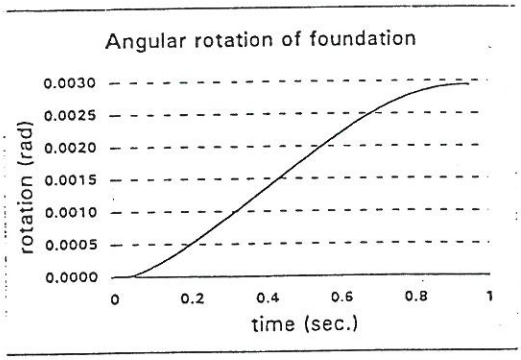

Fig. 9 Angular rotation versus time

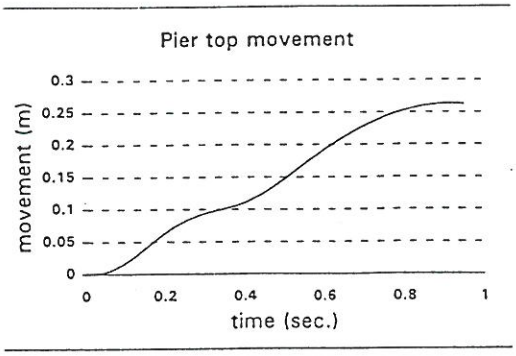

Fig 10 Total top of pier movement versus time

5. Conclusions

On the poster a 2-dimensional non-linear analysis of pier deformation due to ship impact have been presented.

The deformations have been calculated with

- a simplified method using results from an elastic analysis, an assumed standard stress distribution and a simple yield criteria

- a non-linear Plaxis model modelling the complex yielding

For the most practical cases the simplified methods provide sufficient accurate estimates of the overturning moment/rotation curve, which frequently is the determining element for the displacement of the piers.

However, for the Øresund project a full non-linear analysis was needed because "exact" (= contractual) yield curves were specified for the limestone

In this connection it can be added that up to now the effect of pore pressures have rarely been included in the analysis although this effect in certain cases easily may increase the bearing capacity by a two factor.

Earthquake Tests of Reinforced Concrete Frames

P.S. Skjærbæk, S.R.K. Nielsen, P.H. Kirkegaard
Department of Building Technology and Structural Engineering,
Aalborg University, DK-9000 Aalborg, Denmark

Abstract *The paper presents a series of shaking table experiments performed at the Structural Laboratory at Aalborg University, Denmark during the autumn of 1996. A brief description of the purpose and aim of the tests are given and some selected results are presented. The considered structure is a 2-bay, 6-storey reinforced concrete frame in scale 1:5 with the outer measures 2.4 × 3.3 m. The test structure consists of two identical frames spaced 1000 mm on a shaking table. The dead-load of deck elements and pay load is modelled by 8 RC-beams placed on each storey in span between the two frames. One of the frames is instrumented with accelerometers at each storey and the shaking table is equipped with an accelerometer as well. Initially the modal parameters of the test structure are determined from a free decay test, where the top storey is pulled approximately 5 mm out from the equilibrium state. Afterwards the test structure is subjected to the three strong ground motion oscillations where the two first sequences are followed by a free decay test. No free decay test was performed after the third earthquake due to collapse of the test structure during the third strong motion oscillation. After each of the strong motion sequences the structure is visually examined to reveal cracks etc., and this visual damage assessment is compared to the observed reduction in the two lowest eigenfrequencies of the structure which can be extracted from the measured top storey accelerations during the strong motion events.*

Keywords: Shaking Table Testing, RC-frames, Damage Assessment, Modal Identification.

1 Introduction

When civil engineering structures are subjected to sufficiently high dynamic loads it is well known that some kind of damage will occur in the structure. In RC-structures the damage may start as cracking, eventually developing into crushing of concrete and yielding of reinforcement. The damage may be highly localized or more spread out in the structure. During an earthquake both types of damage may develop in the structure and there is a need for methods to assess the damage in the structure. The traditional way of assessing damage in RC-structures is by visual inspection of the structure by measuring cracks, permanent deformations, etc. This is often very cumbersome, since panels and other walls covering beams and columns, need to be removed. Furthermore, internal damage such as bond slippage can be very difficult to determine by visual inspection. However, a much more attractive method is measuring of the structural response at a given location of the structure. From this response time series, damage indicators based on e.g. changes in dynamic characteristics, accumulated dissipated energy, low cycle fatigue models, stiffness or flexibility changes etc. can be calculated. In the literature several methods for damage assessment from measured responses have been presented during the last 2 decades, see Banon et

al. [1] Stubbs et al. [20], Penny et al., [11], Casas [2], DiPasquale et al. [3], Hassiotis et al. [4], Kirkegaard et al. [5], Koh et al. [7], Nielsen et al. [8], Pandey et al. [9], Park et al. [10], Penny et al. [11], Reinhorn et al. [12], Rodriguez-Gomes [13], Skjærbæk et al. [15], [16], Stephens et al. [17], [18], [19] and Vestroni et al. [22].

The motivation for performing earthquake experiments with a scale 1:5 6-storey, 2-bay model test frames are to provide data for verification of methods for non-destructive damage assessment of RC-frames based on measured reponses of the structure during the previous damaging event. The aim of this paper is to show the applicability of the maximum softening damage index as a damage indicator for reinforced concrete frames subject to earthquakes, see e.g. Nielsen et al. [8].

A schematic view of the test set-up is shown in figure 1.

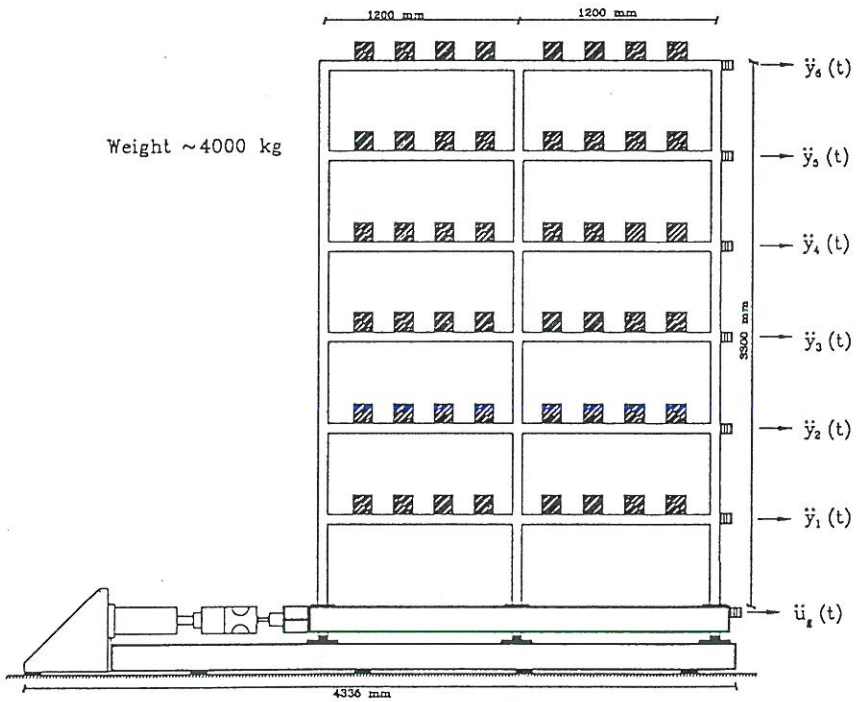

Figure 1: A schematic view of the setup of the considered frame.

The frame considered in this paper is exposed to three earthquake like ground motions of increasing magnitude.

2 Damage Assessment

2.1 The Maximum Softening Damage Index

The maximum softening concept is based on the variation of the vibrational periods of a structure during a seismic event. A strong correlation between the damage state of a reinforced concrete structure that has experienced earthquake and the global maximum softening δ_M has been documented. In order to use the maximum softening as a measure of the damage of the structure it is nessecary to establish a quantitative relationship between the numerical value of the maximum softening and engineering features of damage. This relationship is obviously very complicated and

has to be found by measurement from real structures by regression analysis. DiPasquale et al. [3] investigated a series of buildings damaged during earthquakes and found a very small variation coefficient for the maximum softening damage index, see figure 2.

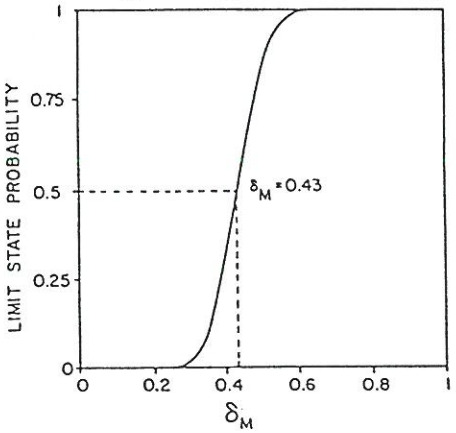

Figure 2: Distribution function of observed limit state values of one-dimensional maximum softening reported by DiPasquale et al. [3].

Nielsen and Çakmak [8] and DiPasquale and Çakmak [3] extended the maximum softening to substructures based on a multi-dimensional maximum softening $\delta_{M,i}$ defined as

$$\delta_{M,i} = 1 - \frac{T_{i,initial}}{T_{i,\max}}, \tag{1}$$

Where $T_{i,initial}$ is the initial value of the ith eigenperiod for the undamaged structure and $T_{i,\max}$ is the maximum value of the ith eigenperiod during the earthquake, see figure 3. Explicit expressions for the damage localization were developed for the 2-dimensional case.

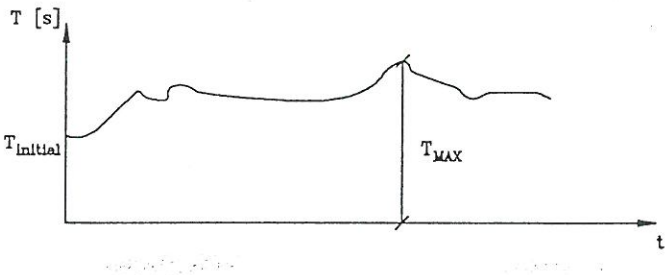

Figure 3: Definition of maximum value of the fundamental eigenperiod.

It is clear from the definition of this index that in case the maximum softening is 0 no damage has occurred in the structure, and when $\delta_M = 1$ there has been a total loss of global stiffness in the structure.

2.2 Visual Inspection

After each series of ground motions the entire structure is visually examined and the damage state of each storey of the building is given one of the following 6 classifications: Undamaged (U), Cracked (CR), Lightly Damaged (LD), Damaged (D), Severly Damaged (SD) or Collapse (CO). Each of the 6 classifications is defined in table 1.

Category	Definition
Undamaged UD	No external sign of changed integrity of any of the columns or beams in the storey.
Cracked CR	Lightly cracking observed in several members but no permanent deformation.
Lightly Dam. LD	Severe cracking observed with minor permanent deformations.
Damaged D	Severe cracking and local large permanent deformations observed.
Severely Dam. SD	Large permanent deformations observed and spalling of concrete at some members.
Collapse CO	Very large permanent deformations observed and severe spalling of concrete at several members.

Table 1: *Definition of the 6 damage classifications used.*

3 Experimental Results

In this section the obtained measurements are presented and the processed data are shown in order to investigate the correlation between observed damage and the calculated softenings.

3.1 Instrumentation of Frames and Data Acquisition

The considered test frame was equipped with an accelerometer at each storey measuring the horizontal acceleration. Furthermore, the shaking table was equipped with an accelerometer. The data aquisition was performed using an 16 channel HBM data-recorder connected to a PC running the HBM CATMAN program. The sampling was performed at a rate of 150 Hz.

In order to eliminate high frequency noise problems the measured acceleration time series are low-pass filtered using a digital 8th order Butterworth filter implemented in the MATLAB program. The filter was designed with a cut-off frequency of 30 Hz.

3.2 Modal Identification of Virgin Structure

The virgin structure was identified from a free decay test, where a force of approximately 50 kg was applied at the top storey to pull the structure out of the equilibrium state.

The modal parameters of the structure are determined using an AutoRegressive Vector model ARV that is fitted to the 6 measured responses at the six storeys, see Kirkegaard et al. [6].

The estimated frequencies and damping ratios are shown in table 2.

mode no.	f_i [Hz]	ζ_i[%]
1	1.95	2.9
2	6.57	1.7

Table 2: *Estimated modal parameters of the virgin structure.*

It should here be noted that especially the estimates of the second mode seem to be somewhat

sensitive to which parts of the free decay are used for the identification. An example of the sampled data from a free decay test is shown in figure 4.

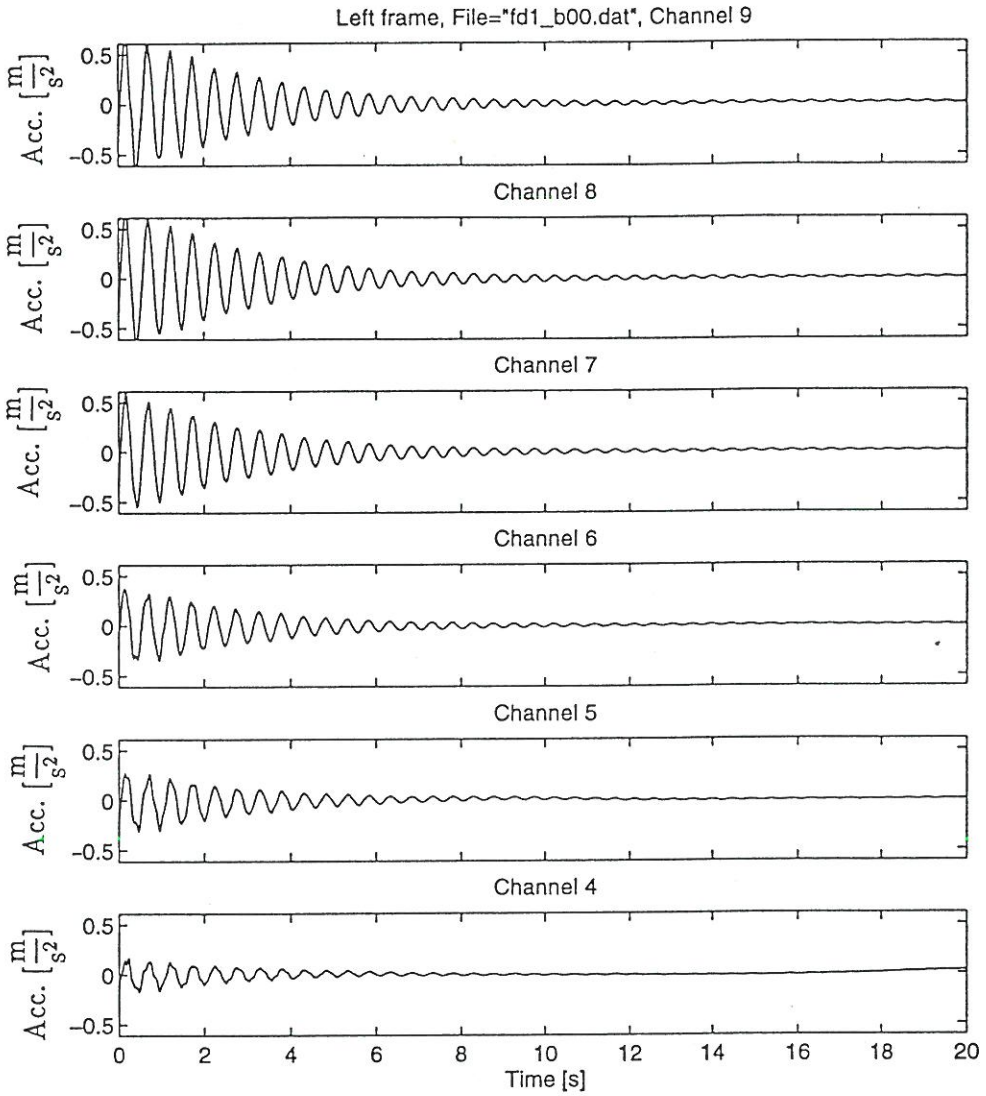

Figure 4: Measured accelerations from pull-out tests of undamaged frame AAU1.

3.3 Strong Motion Tests

During the strong motion part of the experiment the frame is exposed to three sequential earthquake like ground motions of increasing magnitude as shown in figure 5. The earthquakes are modelled using a Kanai-Tajimi filter with a center frequency of 10rad/s and a filter damping of 0.3. The peak-accelerations in the three cases are $-0.14g$, $-0.27g$ and $-0.41g$. After each of the two first earthquakes a free decay test is performed as for the virgin structure.

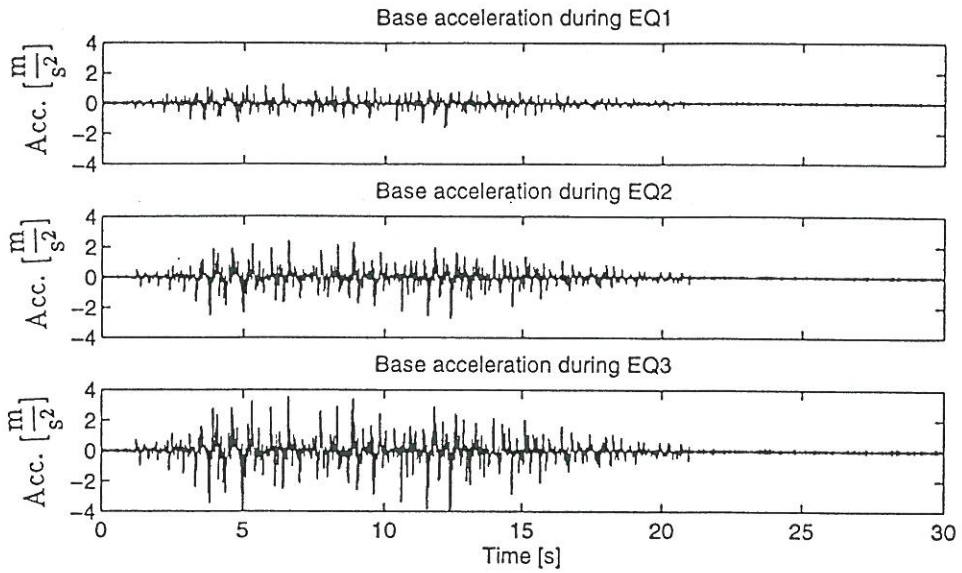

Figure 5: Applied ground motion accelerations during EQ1, EQ2 and EQ3.

During the strong motion events the storey accelerations are measured in the same manner as in the case of the free decay tests. The measured top storey response during the three earthquakes is shown in figure 6. By processing these acceleration time series in an appropriate manner the top storey displacements in figure 7 are obtained, see Skjærbæk et al. [14]. From this figure the decreasing tendency of the fundamental period of the structure is easily seen.

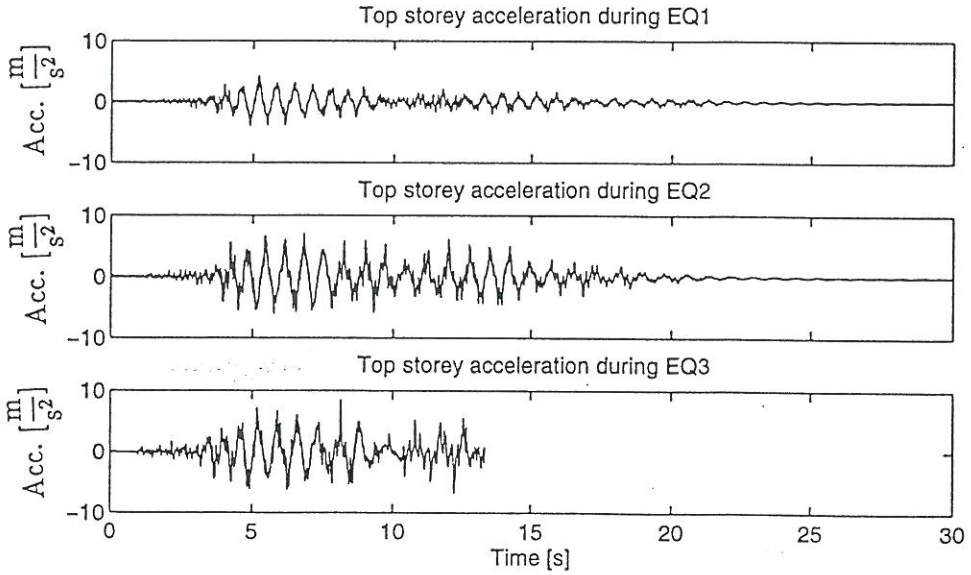

Figure 6: Top storey accelerations during EQ1, EQ2 and EQ3.

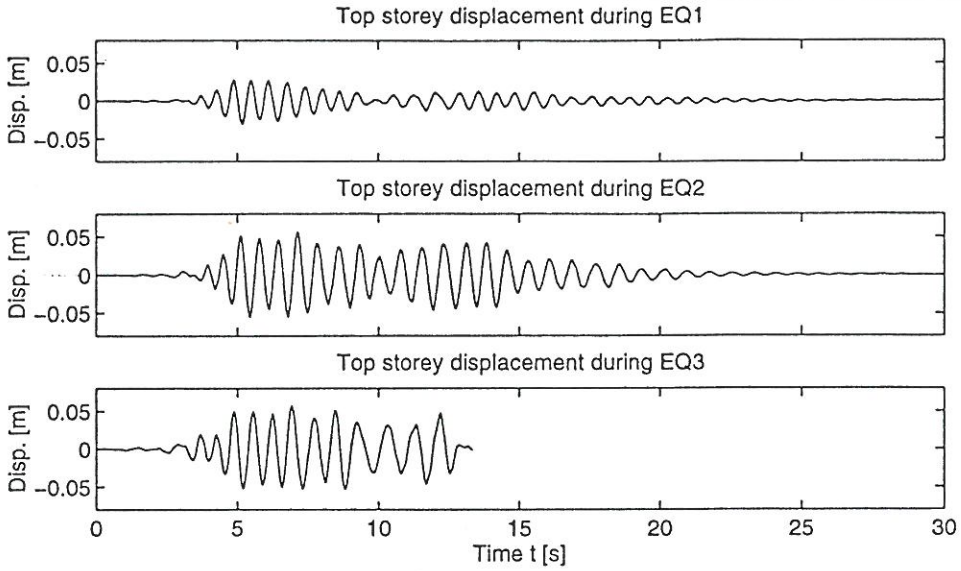

Figure 7: Top storey displacements during EQ1, EQ2 and EQ3.

To identify the modal parameters of the frame as a function of time a recursive implementation of an AutoRegressive MovingAverage Vector model is used. The applied model is a single-input-multi-output model where the estimates are updated sequentially through the time series as new information becomes available. The development in the two lowest frequencies as a function of time is shown in the figures 8-10. It should be noticed that no smoothing of the eigenfrequncies has been performed.

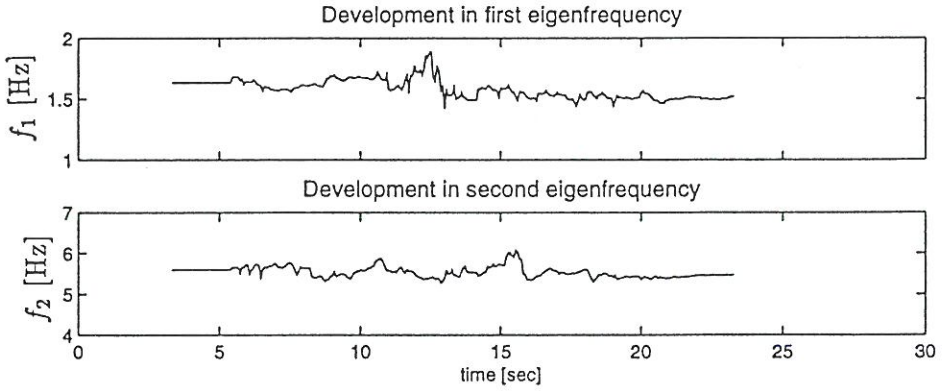

Figure 8: Development of softening in first and second mode during EQ1.

From the figures 8-10 the maximum softenings in the first and second mode can be found and the results are shown in table 3.

	$f_{\min,1}\ [Hz]$	$f_{\min,2}\ [Hz]$	$\delta_{M,1}$	$\delta_{M,2}$
EQ1	1.42	5.28	0.27	0.20
EQ2	1.19	4.71	0.38	0.28
EQ3	0.96	4.37	0.51	0.33

Table 3: *Estimated minimum frequencies and maximum softenings during the three earthquakes.*

The results from the free decay tests performed after EQ1 and EQ2 are shown in table 4.

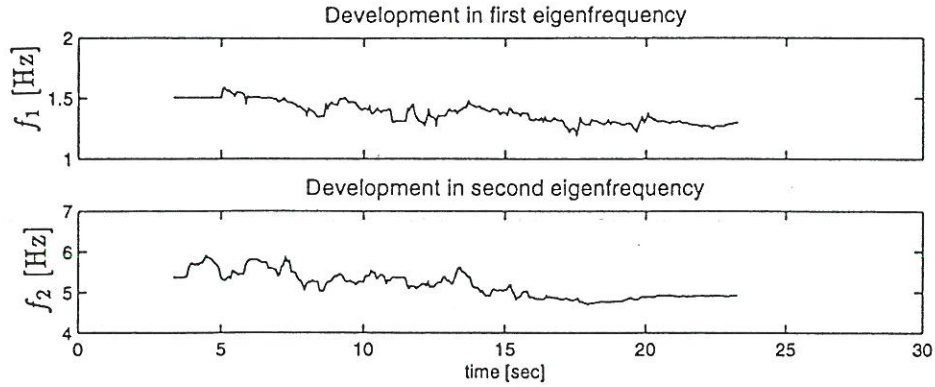

Figure 9: Development of softening in first and second mode during EQ2.

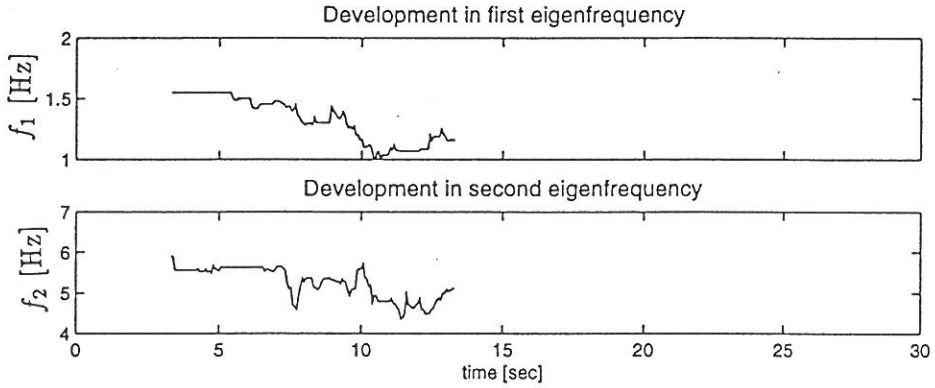

Figure 10: Development of softening in first and second mode during EQ3.

From the estimated minimum frequencies in table 3 and the frequencies estimated from free decay tests (table 4) after each of the earthquake events it is seen that during the earthquake the structural eigenfrequencies are lower than the structural frequencies found for the damaged structure after the earthquake. This indicates that yielding in some of the structural members occur during the earthquake. From table 2 it is seen that the maximum softening in the first mode right before the collapse of the structure is approximately 0.5. This value of the maximum softening is in good agreement with the damage state of a severe damaged structure, see figure 2.

earthquake No.	f_1 [Hz]	f_2 [Hz]	ζ_1[%]	ζ_2[%]
EQ1	1.58	5.62	3.8	2.2
EQ2	1.32	5.01	4.5	2.2

Table 4: *Estimated modal parameters of the damaged structure after EQ1 and EQ2.*

3.4 Visual Inspection of Test Structure

After each of the strong motion events the structure was visually inspected by means of a magnification glass where all cracks were marked by a pencil.

Generally the cracks/damage were concentrated at the beam-column connections at all load levels and the inspection was therefore concentrated at the nodes. The general impression from the visual inspection after both the first and second strong motion oscillations was that the damage was limited since only small cracks were present.

Pictures of the cracks at the middle node at the second storey and at the right node at the second storey are shown in figures 11 and 12 after EQ1 and in figures 13 and 14 after EQ2. Only at the nodes in the second and third storeys significant localized permanent deformations were found. During the third strong motion event both the second and third storey collapsed completely and the first storey suffered severe damage. A picture of the collapsed structure is shown in figure 15. A classification of the damage as described in section 2.2 is given in table 5.

Storey	EQ1	EQ2	EQ3
1	UD	CR	SD
2	CR	LD	CO
3	CR	LD	CO
4	UD	CR	LD
5	UD	CR	CR
6	UD	CR	CR

Table 5: *Damage classifications after the three earthquake events.*

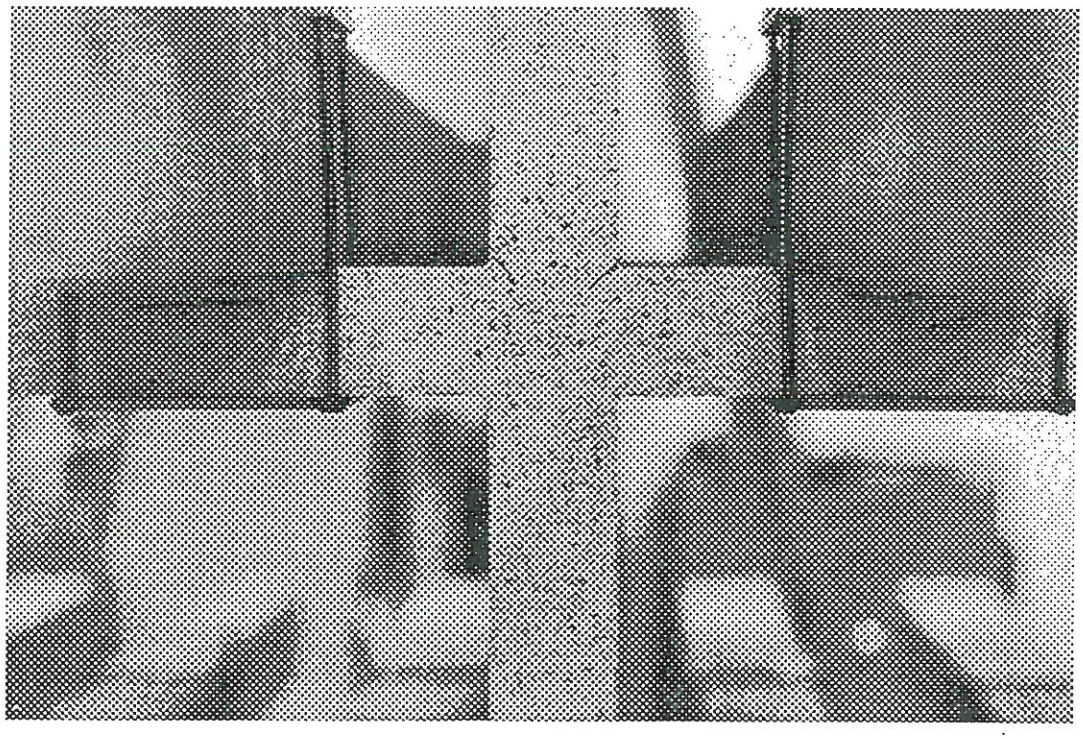

Figure 11: Cracks in node 5 after EQ1.

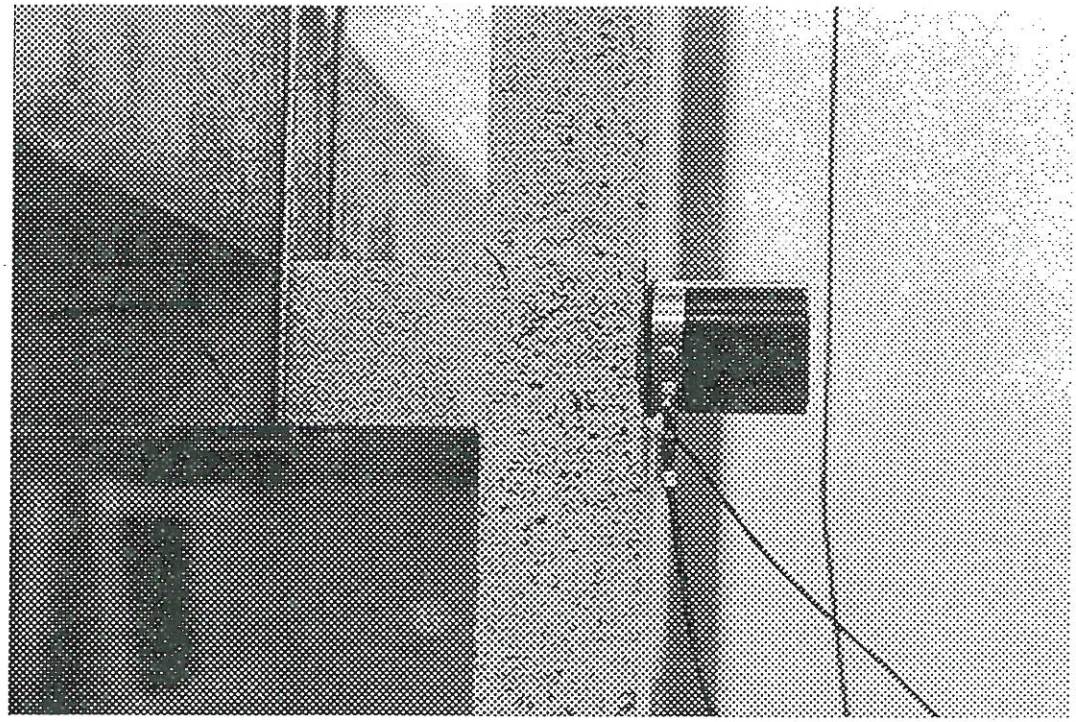

Figure 12: Cracks in node 6 after EQ1.

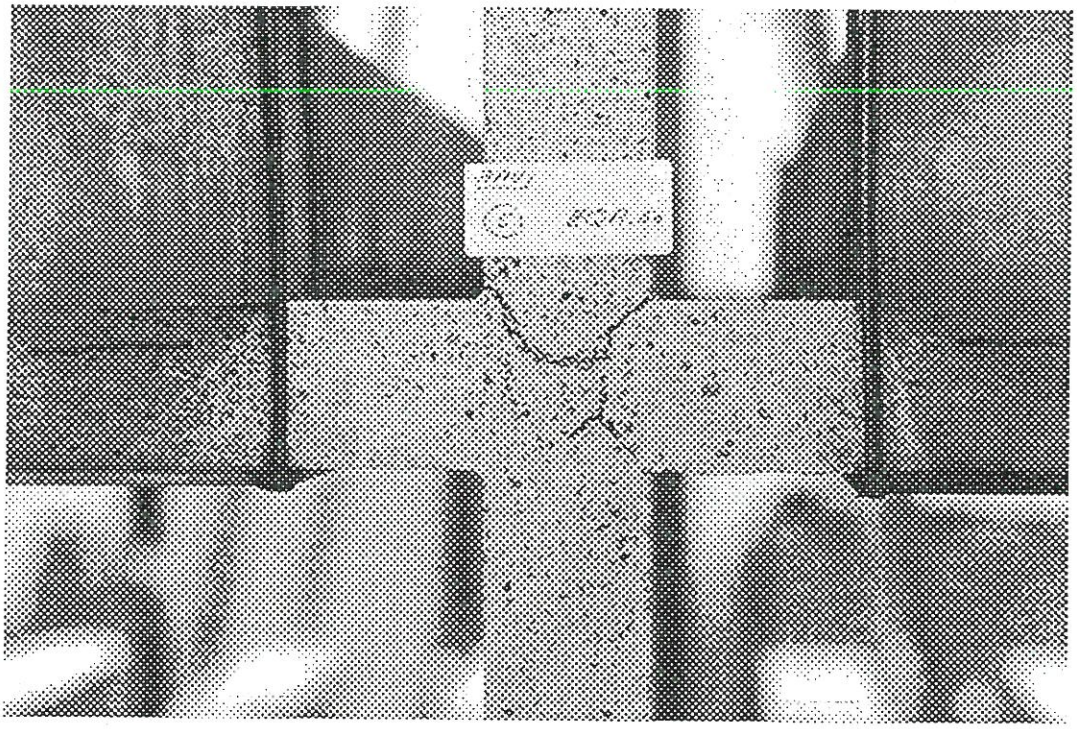

Figure 13: Cracks in node 5 after EQ2.

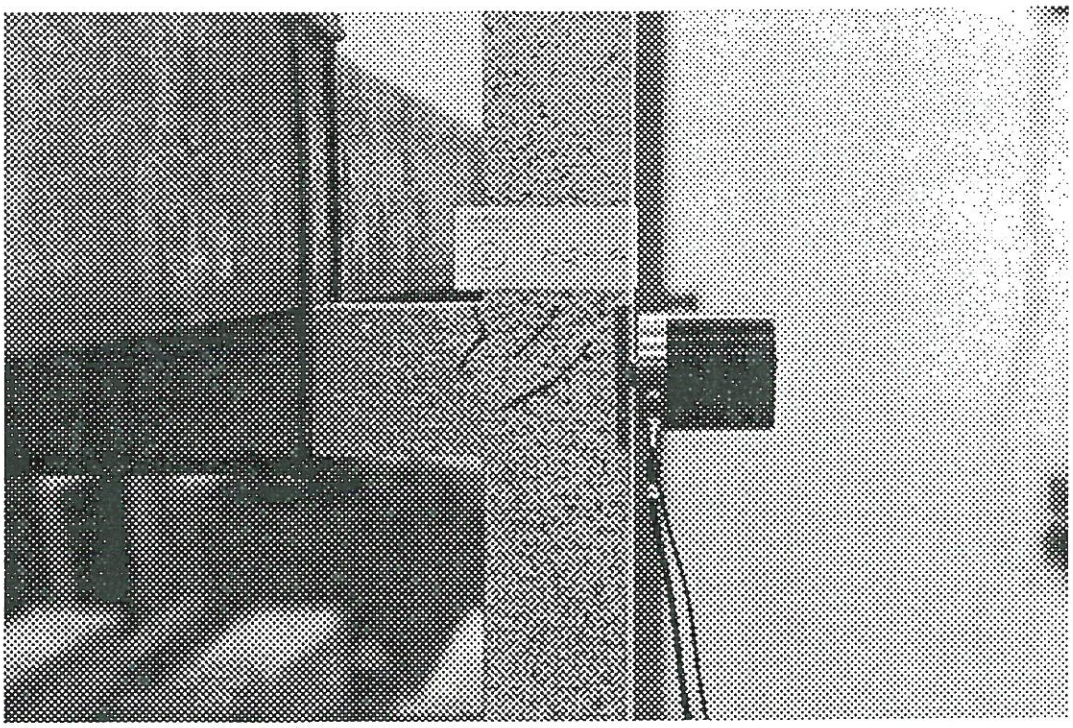

Figure 14: Cracks in node 6 after EQ2.

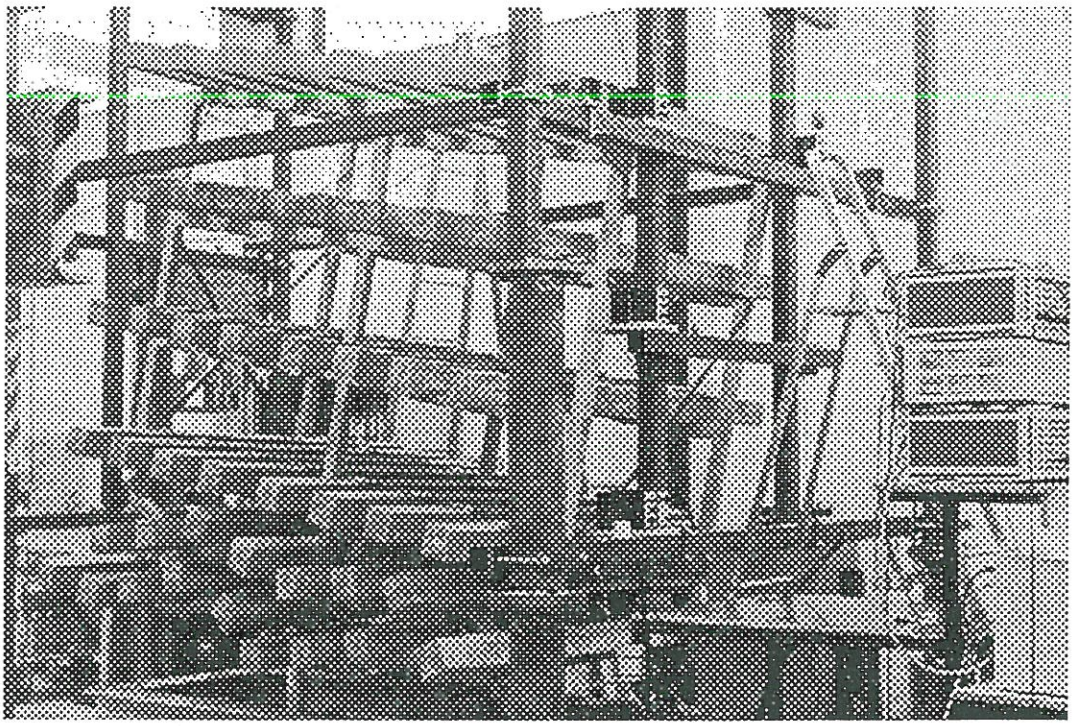

Figure 15: Collapsed structure after EQ3.

By comparing the results of the visual inspection with the evaluated maximum softenings in table 3 the magnitude of the maximum softenings clearly indicate larger structural stiffness changes than the visual inspection. After EQ1 the results of the visual inspection were that only a few small cracks had been initiated and that the structure was basically undamaged. However a maximum softening of 0.28 in the first mode indicates an average stiffness change of approximately 50 per cent. This can be explained by the fact that the damage introduced in the structure during this earthquake is mainly of internal character, such as slippage between concrete and reinforcement.

4 Conclusions

In the paper a series of shaking table tests with a scale 1:5 reinforced concrete frame is considered. Visual damage assessment of the structure was compared to damage assessment based on the two-dimensional maximum softening damage index, and it was found that the considered frame structure showed significant values of the maximum softening even though basically no external damage was observed during the visual inspection. Higher values of the maximum softening in the first mode than in the second mode was found and this indication of the highest damage level in the lower part of the structure is supported by the visual inspection where the largest cracks were found in the three lowest storeys.

5 Acknowledgement

The present research was partially supported by The Danish Technical Research Council within the project: Dynamics of Structures.

References

[1] Banon, H., Biggs, J. M. and Irvine, H. M., *Seismic Damage in Reinforced Concrete Frames*, Journal of the Structural Division, Proc., ASCE, Vol. 107, No. ST9, Sept. 1981, pp 1713-1729.

[2] Casas, J.R. *Structural Damage Identification from Dynamic-Test Data*, ASCE J. Struc. Eng. Vol. 120, No. 8, Aug. 1994, pp. 2437-2450.

[3] DiPasquale, E. and Çakmak, A. Ş. *Detection of Seismic Structural Damage using Parameter-Based Global Damage Indices*, Probabilistic Engineering Mechanics, Vol. 5, No. 2, pp. 60-65, 1990.

[4] Hassotis, S and Jeong, G.D. *Assessment of Structural Damage from Natural Frequency Measurements*, Computers and Structures, Vol. 49, No. 4, pp. 679-691, 1993.

[5] Kirkegaard, P.H. and Rytter, A. *Use of a Neural Network for Damage Detection in a Steel Member*, Presented at the Third Int. Conf. in the Application of Artificial Intelligence to Civil Engineering Structures, Civil-Comp93, Edinburgh, August 17-19, 1993.

[6] Kirkegaard, P.H. Skjærbæk, P.S. and Nielsen, S.R.K. *Identification Report: Earthquake Tests with Scale 1:5 RC-Frames*, Internal Report, Aalborg University, Denmark.

[7] Koh, C.G., See, L.M. and Balendra, T. *Damage Detection of Buildings: Numerical and Experimental studies*, ASCE J. Str.Eng., Vol. 121, No. 8, pp. 1155-1160, Aug. 1995.

[8] Nielsen, S.R.K. and Çakmak, A.Ş., *Evaluation of Maximum Softening Damage Indicator for Reinforced Concrete Under Seismic Excitation*, Proceedings of the First International Conference on Computional Stochastic Mechanics. Ed. Spanos and Brebbia, pp. 169-184, 1992.

[9] Pandey, A.K. and Biswas, M., *Damage Detection in Structures using Changes in Flexibility.* Journal of Sound and Vibration 169(1), pp. 3-17, 1994.

[10] Park, Y.J. and Ang, A. H.-S., *Mechanistic Seismic Damage Model for Reinforced Concrete*, ASCE J. Struc. Eng., 111(4) April 1985, pp.722-739.

[11] Penny, J.E.T., Wilson, D.A.L., and Friswell, M.I., *Damage Location in Structures using Vibration Data*, Aston University, Birmingham, UK, 1993.

[12] Reinhorn, A.M., Seidel, M.J., Kunnath, S.K. and Park, Y.J., *Damage Assessment of Reinforced Concrete Structures in Eastern United States.* NCEER-88-0016 technical report, June 1988.

[13] Rodriguez-Gomez, S., *Evaluation of Seismic Damage Indices for Reinforced Concrete Structures*, M.Sc. Thesis, Princeton University, Oct. 1990.

[14] Skjærbæk, P.S., Nielsen, S.R.K. and Kirkegaard, P.H., *Earthquake Tests on Scale 1:5 RC-Frame*, Laboratory report, Aalborg University, Denmark, 1997.

[15] Skjærbæk, P.S., Nielsen, S.R.K. and Çakmak, A.S., *Assessment of Damage in Seismically Excited RC-Structures from a Single Measured Response*, Proceedings of the 14th IMAC, Dearborn, Michigan, USA, February 12-15, 1996, pp. 133-139.

[16] Skjærbæk, P.S., Çakmak, A.S. and Nielsen, S.R.K., *Identification of Damage in RC-Structures from Earthquake Records - Optimal Location of Sensors*, Journal of Soil Dynamics and Earthquake Engineering, No. 6, Vol. 15, 1996, pp. 347-358.

[17] Stephens, J.E. and Yao, J.P.T., *Damage Assesment Using Response Measurements*, ASCE J. Struct Eng. 113 (4) April 1987, pp. 787-801.

[18] Stephens, J.E., *A Damage Function Using Structural Response Measurements*, Structural Safety Studies, ASCE, May 1985, pp. 22-39.

[19] Stephens, J.E., *Structural Damage Assesment Using Response Measurements*, Ph.D.-thesis, Purdue University, 1985.

[20] Stubbs, N. and Osegueda, R., *Damage Detection in Periodic Structures*, Damage Mechanics and Continuum Mechanics, ASCE, October 1985.

[21] McVerry, G. H., *Structural Identification in the Frequency Domain from Earthquake Records*, Earthquake Engineering and Structural Dynamics, Vol. 8, 1980. pp. 161-180.

[22] Vestroni F., Cerri, M.N. and Antonacci, E., *Damage Detection in Vibrating Structures*, Proceedings of Structural Dynamics - EURODYN'96, Ed. Augusti, Borri and Spinelli, Torino, Italy, 1996, pp. 41-50.

ISSN 1395-7953 R9661
Aalborg University
Dept. of Building Technology and Structural Engineering
Sohngaardsholmsvej 57
DK-9000 Aalborg, Denmark
Tel.: +45 9635 8080 Fax: +45 9814 8243

Printed at Aalborg University